TOWARD AN ELECTRONICALLY SCANNED IMAGER FOR MICROWAVE IMAGING OF THE COMPRESSED BREAST

TOWARD AN ELECTRONICALLY SCANNED IMAGER FOR MICROWAVE IMAGING OF THE COMPRESSED BREAST

By

Nooshin Valizade Shahmirzadi, B.Sc, M.A.Sc.

A Thesis

Submitted to the School of Graduate Studies

in Partial Fulfillment of the Requirements

for the Degree of

Doctor of Philosophy

Doctor of Philosophy (2024) McMaster University

(Electrical and Computer Engineering) Hamilton, Ontario, Canada

TITLE: Toward an Electronically Scanned Imager for Microwave Imaging of the Compressed Breast

AUTHOR: Nooshin Valizade Shahmirzadi

B.Sc. Shahid Beheshti University, Tehran, Iran

M.A.Sc. Iran University of Science and Technology, Tehran, Iran

SUPERVISOR: Dr. Natalia K. Nikolova

Ph.D. (University of Electro-Communications)

P. Eng. (Ontario)

CO-SUPERVISOR: Dr. Chih-Hung Chen

Ph.D. (McMaster University)

NUMBER OF PAGES: xxiii, 149

To my parents and my beloved spouse

Abstract

Microwave imaging shows promise for breast cancer screening and detection, offering non-ionizing radiation, low-cost, compact electronics, and compatibility with fast image reconstruction methods. However, clinical adoption is limited, largely due to the need for efficient data acquisition systems with high dynamic range and low signal clutter. This work introduces a novel ultra-wideband (UWB) electronically switched breast microwave imager that multiplexes hundreds of active antennas on the receiver side at a single-tone intermediate frequency (IF) to alleviate the limitations of the UWB radio frequency (RF) switching. The research is structured around three main contributions. First, a 16×16 planar UWB receiving (Rx) array of shielded slot antennas is developed on printed circuit board (PCB) technology, with each antenna equipped with a low-noise amplifier (LNA). Due to space constraints, the remaining front-end circuitry, including the mixers and the IF switching network, are incorporated on separate boards, requiring seamless board-to-board RF transitions. To this end, the second contribution focuses on a low-cost, mechanically robust, low-crosstalk interconnection solution using high-pin-density high-speed vertical connectors (HSVCs) widely adopted in computer technology to link the Rx array to its front-end circuitry. Finally, an electronically switched 16×16 UWB transmitting (Tx) array is proposed, also leveraging HSVCs to enable efficient integration with various RF feed networks, providing flexible illumination scenarios for the microwave breast imager. Together, these innovations take a step forward in making UWB microwave imaging clinically viable for the non-invasive, real-time detection of breast cancers.

Acknowledgements

First, I would like to profoundly thank my supervisor, Prof. Natalia K. Nikolova, for her tremendous support, insightful guidance, and belief in me, which have been the backbones of my studies. It has been a privilege to work with her. Besides being a great scientist and leader, she is always so encouraging and is a mentor who truly cares about her students. Her belief in my abilities has not only instilled more confidence in myself but also pushed me to strive for development as a researcher and as a professional. The knowledge I have gained through her is something that will stay with me throughout my career.

I am also thankful to my co-supervisor, Prof. James Chen, whose invaluable insights and encouragement have been instrumental in shaping my work. I would also like to take this opportunity to express my sincere appreciation to my supervisory committee members, Prof. Jamal Deen and Prof. Xun Li, for their helpful feedback and fruitful discussions that have enriched my research in many ways.

To my colleagues at the EMVi lab, your efforts have made this journey both memorable and rewarding. I would like to thank Jimmy Nguyen and Aaron Pitcher for your patience and teaching me practical skills that have been useful in my work. Your willingness to answer every question and help through countless measurements has meant a great deal to me. To Vartika Tyagi for helping me get up to speed on running projects soon after your graduation, and for an invaluable year we spent navigating challenges together, especially in designing the Rx array first prototype. Dr. Romina Kazemivala, your support in my early days in Canada, especially in the middle of challenges of the Covid lockdown, was like a lifeline. I will never forget the long days in the lab doing imaging experiments. To Dr. Zhenyuan Zhang, Guanchen Li, Roxana Nikoukar, Golap Kanti Dey, Mihail Georgiev and Sepideh Hassani, thank you for your support that made even the hardest days feel manageable. A special mention to Philip Krivor and Zimu Liu for their efforts in developing the microcontroller boards for the Tx and Rx arrays.

I must also deeply acknowledge Tyler Ackland for the great help he provided during fabrication and assembly. Tyler, your guidance through challenges, your patience, and your willingness to lend a hand whenever I needed help were instrumental to the success of this work. Your expertise coupled with your unwavering willingness to support me is much appreciated. Thank you for being a substantial part of this journey.

To my family in Iran, you are my pillars. To my father, whose absence is a void that words could never describe, your dedication to my education and pride in my accomplishments inspire me daily. I always carry with me your love and the life lesson you have taught me. Mom: Your unconditional love and unshakeable belief in me have been my strength that keeps me grounded and focused withstanding distances and challenges. To my siblings, I will forever be grateful for your encouragement and support.

Last, but certainly not least, I extend my deepest gratitude to my husband, Ehsan, for his unwavering love, patience, and faith in my abilities. The distance from our families has posed significant challenges; however, your steadfast support has profoundly impacted my journey. You have remained by my side throughout each obstacle, and I acknowledge that I could not have accomplished this without

your presence. This achievement belongs equally to you as it does to me, and I am eternally thankful to have you alongside me.

Contents

List of Figures

List of Tables

Notation and Abbreviations

2D	Two Dimensional
ADS	Advanced Design System
AI	Artificial Intelligence
CPW	Co-planar Waveguide
D-C	Dartmouth College
EM	Electromagnetic
ESAA	Electronically Scanned Antenna Array
FG	Fibro-glandular
F-SPM	Fourier-space scattered power mapping
GCPW	Grounded Co-planar Waveguide
HSVC	High-speed Vertical Connector
H-U	Hiroshima University
IF	Intermediate Frequency
LNA	Low Noise Amplifier
LO	Local Oscillator
MG-U	McGill University
MITS	Microwave Imaging Transmission System
MRI	Magnetic Resonance Imaging
MVG	Microwave Vision Group
PCB	Printed Circuit Board
PEC	Perfect Electric Conductor
RF	Radio Frequency

Rx	Receiving
SAFE	Scan and Find Early
SAR	Specific Absorption Rate
SFCW	Step Frequency Continuous Wave
SMA	Sub-miniature Version A
SMPS	Sub-miniature Push-on Sub-micro
SNR	Signal to Noise Ratio
TEM	Transvers Electromagnetic
TL	Transmission Line
Tx	Transmitting
UWB	Ultra-wideband
VNA	Vector Network Analyzer

Chapter 1

1. Introduction

1.1 Limitations of Conventional Breast Imaging Modalities

Even with considerable advances in medical imaging, breast cancer remains the second-leading cause of cancer-related deaths among women worldwide, with an estimated 670,000 deaths in 2022 alone [1]. Early detection of breast cancer is critical in improving survival rates, since cancer treatment in the early stage of the disease (i.e., before the onset of metastasis) is much more successful. However, regular screening, essential for early diagnosis, has certain limitations with the current imaging techniques, including X-ray mammography, ultrasound, and magnetic resonance Imaging (MRI).

X-ray mammography, the primary screening modality, utilizes ionizing radiation, restricting the frequency of the patient examination and creating health hazards. Besides, mammography has poor sensitivity for women with dense breast tissue, which diminishes the diagnostic value of this modality in a large section of the population [2]. The use of ultrasound, usually as a complementary tool after suspicious mammography results, also faces problems due to a high false-positive rate, thereby limiting its usefulness as an independent screening modality. MRI offers superb contrast resolution and is invaluable for treatment response or

Table 1-1: Comparison of existing breast cancer detection modalities – advantages and limitations

Mammography	Ultrasound	MRI
☑ widely available and cost effective ☑ high spatial resolution ☑ fast acquisition time	☑ real-time imaging ☑ non-ionizing ☑ portable and cost effective	☑ high contrast for soft tissue ☑ non-ionizing ☑ excellent for dense breast tissue and high-risk patients
☒ ionizing radiation ☒ uncomfortable breast compression ☒ high false-negative rates in dense breast	☒ high false-positive rate ☒ operator dependence ☒ only complementary	☒ expensive, limited access ☒ contrast agent required ☒ long scan times

presurgical evaluation, but its high cost, limited availability, and the requirement for a contrast agent (which can accumulate over time [3]), make it infeasible for screening applications. Table 1-1 summarizes the advantages and disadvantages of the available modalities for breast cancer detection. The limitations of current methods highlight the urgent need for safer, more affordable, and widely accessible imaging alternatives.

1.2 Microwave Imaging for Breast Cancer

Microwave biomedical imaging was introduced in the mid-1980s [4] and has been explored extensively as a possible alternative modality for breast-cancer detection and screening. It utilizes the contrast in the electrical properties at microwave frequencies between normal and malignant tissues, which are mainly due to the higher water content in malignant tumors than in normal tissue [2]. This, in turn, means that healthy and cancerous tissues show different responses to microwave signals, which enables non-invasive abnormality detection without ionizing radiation hazards or the use of contrast agents. Furthermore, microwave imaging supports various fast image reconstruction methods and uses compact, cost-effective electronics, making it a promising candidate for accessible breast-cancer screening. Microwave imaging techniques can be categorized into two main types based on the image reconstruction approach: quantitative and qualitative [5], [6]. In quantitative imaging, dielectric maps of the real and imaginary permittivity values are generated, providing information about the tissue composition within the examined breast. In contrast, qualitative imaging provides an energy or intensity map of the scattering sources, which highlights the areas of intense scattering within the object and offering a visual localization of potential anomalies.

While microwave imaging offers a safer and more accessible option for breast-cancer screening, several technical limitations must be addressed. One challenge is its limited penetration in radiologically dense breast tissues (BI-RADS[1] categories C and D), where dense fibro-glandular tissue impedes the signal penetration and its interaction with potential abnormalities. This limitation is more pronounced than in MRI and ultrasound, although microwave imaging may perform comparably—or even slightly better—than X-ray mammography due to higher contrast between malignant and healthy tissues in the breast. Still, the permittivity contrast between malignant and fibro-glandular tissue is low at microwave frequencies, with a malignant-to-fibro-glandular mean contrast ratio ranging only from 1.4:1 to 1.5:1. For reference, this contrast is in the range of

[1] BI-RADS stands for Breast Imaging Reporting and Data System introduced by the American College of Radiologists.

1.055:1 to 1.018:1 for the X-ray attenuation coefficients. This is the main reason for the difficulty in differentiating malignant from healthy tissues in both X-ray mammography and microwave imaging [2]. Moreover, in microwave imaging, near-field effects and breast-tissue heterogeneity introduce inaccuracies in the image reconstruction. Another consideration is the spatial resolution, which is currently around 10 mm. While this resolution is deemed sufficient for screening, it does limit the precision needed for detecting smaller lesions, especially for tumors located deeper within dense tissues.

Breast-tissue microwave imaging is typically performed within the ultra-wideband (UWB)[2] frequency range, and it encompasses both frequency-domain and time-domain measurement approaches. This frequency range offers an optimal balance between spatial resolution and tissue penetration, as it utilizes both high and low frequency components of the transmitted (Tx) signal. Furthermore, within this range, healthy and malignant tissues exhibit somewhat different contrasts in the dielectric properties, which aids the image reconstruction and the diagnosis [7], [8].

1.3 Antennas and Arrays in Breast Microwave Imaging

In UWB breast microwave imaging systems, antennas play a pivotal role for the quality of both Tx and Rx signals, and their design profoundly impacts the imaging performance. Various antenna types have been proposed for UWB microwave breast imaging [7][8]-[10], most of them designed to work in direct contact with tissue. Achieving proper impedance matching (reflection coefficient

[2] The Federal Communications Commission (FCC) has allocated a 7.5 GHz bandwidth (3.1 to 10.6 GHz) for UWB applications, including measurements, communications, and radar.

below −10 dB) across the entire UWB frequency presents unique challenges. Antennas in contact with biological tissues exhibit different radiation characteristics and return loss than those in free space. The proximity to the tissue causes reflections that are often stronger than those from the malignant tissues, especially those that are deep inside the organ. To address this problem, two primary strategies are commonly employed: (1) the antennas are designed to operate in direct contact with the skin, ensuring optimal power coupling and reduced signal loss, and (2) utilizing a coupling medium or liquid to enhance the impedance match regardless of the breast tissue type which minimizes the reflection at the interface between the coupling medium and the tissue.

Designing skin-contacting antennas can largely address the problem of skin reflections. However, the frequency dependence of the conductivity and permittivity of tissue (see Figure 1-1) and the wide variations of tissue properties among patients must be carefully considered during the design and testing phases. These variations must be addressed by making the antenna impedance match less sensitive to the tissue property variation, particularly in real-world testing. Also, air gaps between the antenna and the skin can result in impedance mismatches, and this possibility must be eliminated by properly designing the imaging apparatus.

Alternatively, a coupling medium can be used, where both the antenna and the organ are immersed in a liquid with dielectric properties similar to those of breast tissue at the operating frequencies. Here, the antenna input impedance is matched to the coupling medium which makes the antenna usable with various types of breast-tissue density. Despite this advantage, this approach still fails to fully eliminate reflections from the skin over the wide UWB spectrum and it

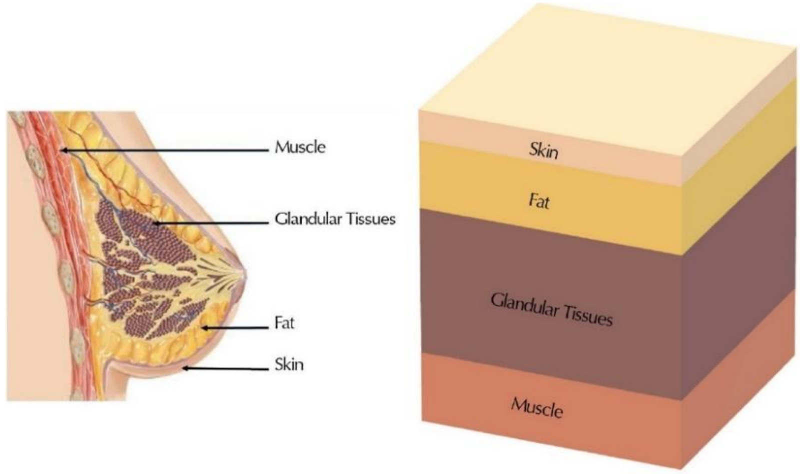

(a)

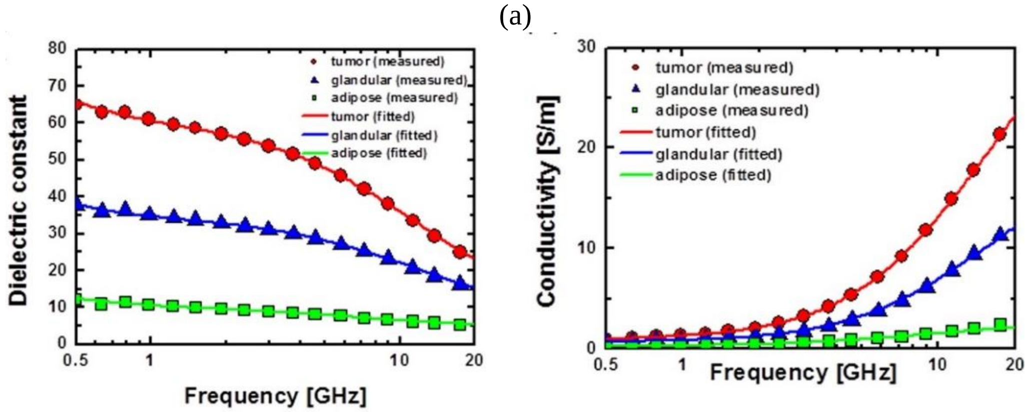

(b)

Figure 1-1: (a) Cross-sectional view of the breast along with simplified breast model adapted from [8], and (b) Data-fitted curves based on the two-pole Cole-Cole model for permittivity and conductivity of the human breast tissues adapted from [11].

introduces additional signal losses during transmission and reception. It is worth to note that some antennas for breast microwave imaging are designed to operate in air, where antennas with high gain and directivity are selected to enhance the resolution and the detection sensitivity. In this case, the reflections from the skin are strong, and special methods must be devised to de-embed them from the received back-scattered signals.

Monopole and slot microstrip antennas are particularly appealing options for breast microwave imaging due to their broadband performance and relatively small size. As long as good front-to-back ratio is achieved, they are suitable for deployment in various array configurations [13]-[21]. Vivaldi and horn antennas offer wide bandwidth, beneficial for breast microwave imaging, but their large size makes them less suitable for large array configurations, often requiring mechanical scanning to increase spatial sampling [22]-[27]. Current research in breast microwave imaging is also investigating alternative antenna types, including fractal [28], [29] and metamaterial antennas [30], [31].

Dense spatial sampling can be achieved either through a densely packed array of antenna elements multiplexed through a switching network [20], [21] or by using a sparser array in conjunction with mechanical scanning [25]-[27]. In a densely packed array, the mutual coupling between adjacent elements becomes a critical consideration, requiring a careful balance between dense sampling and minimized coupling. Conversely, mechanical scanning offers flexibility in spatial sampling intervals and patterns, array element size, and mutual coupling control; however, it suffers from increased data acquisition time and potential positioning errors.

The choice of array type and geometry further impacts imaging performance. Antenna arrays utilized in microwave imaging systems can be categorized into three primary types based on their design and operation [5].

Synthetic arrays involve the movement of either the Tx antennas, Rx antennas, or both during the scan [19], [26], [27], [32], [33]. This movement allows for data collection from different angles or positions, simulating a larger array. However, synthetic arrays face significant challenges, such as prolonged data acquisition times and the potential for positioning inaccuracies.

In hardware arrays, the individual antennas remain stationary, but the entire array can be rotated or repositioned for repeated scans [21]. This method is mainly used for artifact removal, image enhancement, or to gather more comprehensive data from multiple viewpoints. Although hardware arrays offer faster acquisition times compared to synthetic arrays, the overall acquisition time can still be extended, as multiple scans are required at different rotational angles to remove artifacts.

Stationary arrays are characterized by fixed antenna elements with no moving parts [34]-[36]. Scanning is performed without mechanical adjustments. These arrays are robust and simple to operate, as they do not rely on complex mechanical systems. Stationary arrays are potentially faster than the hardware and synthetic arrays since the scan time is limited by the switching network and hardware acquisition time. However, they may lack the flexibility or coverage of synthetic or hardware arrays, particularly when multi-angle data acquisition is necessary to enhance the imaging quality.

Antenna arrays can be arranged in various geometries. The hemispherical configuration is widely favored in breast microwave imaging due to its natural conformity to the breast curvature [19]-[21]. However, variations in the breast size necessitate a coupling medium or gel to fill any gaps, in order to prevent impedance mismatching between the antenna and the skin.

The cylindrical configuration is another common configuration in the breast microwave imaging systems. It consists of antennas arranged in a circular pattern, either surrounding a cylindrical tank containing the coupling fluid and the breast [27], [32], [33], or positioned inside the tank itself [32]. The antennas can be mechanically moved vertically or horizontally to facilitate multi-angle measurements. The use of a coupling medium (usually lossy) in cylindrical arrays is necessary to address the impedance mismatch between the antenna and the breast tissue. However, this introduces additional signal loss. Furthermore, the immersion of the breast in the coupling medium raises concerns about proper system maintenance and the prevention of infections. Since the breast is suspended in the fluid, motion during measurements may occur which is detrimental in imaging.

Contrary to hemispherical and cylindrical configurations, wearable configurations offer greater flexibility and can be integrated into a bra for more comfortable imaging, avoiding the need for patients to lie in prone or supine positions [34]. However, wearable configurations need to accommodate different breast sizes and may face constraints on the total number of accommodated antennas. Antenna elements for wearable configurations are fabricated on flexible substrates, often with low permittivity, which presents challenges in size reduction, impedance match, dense packing of the elements and electrical reliability.

Planar configurations, on the other hand, offer ease of fabrication and integration on a single PCB for a skin-contacting configuration. This allows for efficient array expansion when more elements are required (for larger breast sizes). Planar configurations also benefit from shorter signal paths, enhancing signal quality [17], [35]. However, planar arrays are not adaptable to the natural breast curvature and thus require some degree of breast compression to ensure effective imaging.

1.4 Advances and Prototypes in Breast Microwave Imaging Technology

Numerous research teams and institutions worldwide are actively engaged in the development of advanced prototypes for breast-tissue microwave imaging. Some research groups utilize breast-tissue phantoms for controlled experimental imaging, while others are conducting clinical trials to assess the real-world applicability of their prototypes. Table 1-2 provides a comprehensive overview of some of the prototypes that have undergone clinical trials, summarizing key technical specifications such as antenna type, operating frequency, coupling medium, scan time, and the nature of the imaging methodology (qualitative vs. quantitative). Note that the total time required for clinical applications includes both the scan duration and the time for image reconstruction. However, since image reconstruction time is heavily influenced by computational resources and varies significantly between systems, only the scan duration is reported in the Table 1-2.

The first breast microwave imaging system tested on humans was developed by an American team at Dartmouth College (D-C) [32]. This pioneering system performs frequency-domain measurements within the range from 0.7 GHz to 1.7 GHz. It incorporates 18 monopole antennas as a synthetic array arranged in a circular configuration submerged in a lossy medium to achieve efficient impedance matching and signal penetration. The antennas are moved vertically to perform cross-plane multi-slice measurements. Although each breast scan takes approximately 2 minutes, the system's image resolution is limited due to the relatively low operating frequency. Also, the vertical movement of the antennas introduces potential for mechanical inaccuracy or problems with alignment. The vertical sampling rate is constrained by the measurement time, and it determines the vertical resolution of the image.

A compact, handheld prototype developed in Hiroshima University (H-U in Table 1-2), Japan [19], performs UWB time-domain measurements without the need for a coupling medium. This prototype features a synthetic array of 4×4 slot antennas arranged in a cross-shaped configuration inside a hemispherical dome. The antennas are capable of rotating 360° in 9° increments using a step motor, ensuring coverage around the breast. Each scan requires approximately 15 minutes, with additional image processing time extending to several hours.

Another prototype, developed by an Italian research team under the name *Mammowave*, performs frequency-domain measurements across a frequency range from 1 GHz to 9 GHz in the air [26]. This system utilizes a horn antenna as the transmitter and a Vivaldi antenna as the receiver. Both Tx and Rx antennas rotate azimuthally to gather data in a multi-bistatic mode. A notable feature of the *Mammowave* system is its integration with artificial intelligence (AI), which aids in the detection of lesions, thereby enhancing diagnostic accuracy. The system achieves a data acquisition time of 7 minutes per breast, but image processing and precise positioning of the breast within the device require additional time, further complicating its application in clinical environments.

A research group at McGill University (MG-U in Table 1-2) proposed a compact wearable imaging system consisting of a 16-element monopole antenna stationary array integrated into a bra [34]. This system utilizes multistatic measurements with time-domain signals operating across a frequency range from 2

GHz to 4 GHz. The antennas are designed to function in direct contact with tissue, eliminating the need for a coupling medium. The system faces certain challenges. The resolution is limited by the relatively narrow frequency range, and it has been tested on a single volunteer. This necessitates further trials to validate its performance and reliability.

The Microwave Vision Group (MVG) in France has developed a breast microwave imaging system known as *Wavelia*, which employs 18 wideband Vivaldi probes as a synthetic array arranged in a circular fashion in a horizontal plane outside a cylinder filled with coupling fluid [27]. The array moves vertically to examine the breast tissue at 5 mm intervals, operating within the frequency range from 0.5 GHz to 4 GHz. Although each breast scan takes approximately 7 minutes the total process—including quality checks, patient positioning, and system, calibration—can extend up to 50 minutes per patient. Additionally, this system is not suitable for small-breasted individuals (e.g., A-cup) due to the need for the breast to fit properly within the cylindrical scanning area.

A research team in the University of Calgary, Canada, has developed a microwave imaging transmission system (MITS) similar to X-ray mammography but with slight compression of the breast [35]. This system incorporates two arrays of five custom-designed Vivaldi radiating elements encapsulated within a cylindrical waveguide [24], which makes direct contact with the skin. The antennas on the bottom plate are sequentially excited, with the signals transmitted through the tissue being detected by the upper array sensors. The system performs frequency-domain measurements over the range from 0.1 GHz to 10 GHz.

Table 1-2: Comparison of some key features in breast microwave imaging prototypes undergoing clinical trials

	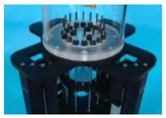				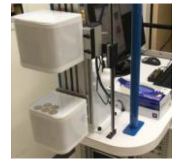			
	D-C [32]	H-U [19]	*Mammowave* [26]	*Wavelia* [27]	MITS [35]	*SAFE* [33]	*MARIA* [21], [37], [38]	MG-U [34]
Antenna type and number of elements	monopole 18	slot 4×4	1 horn (Tx) & 1 Vivaldi (Rx)	Vivaldi probes 18	encapsulated Vivaldi 5 Tx & 5 Rx	N/A 2	cavity-backed slot 60	Monopole 16
Frequency	0.7 GHz-1.7 GHz	3.1 GHz-10.6 GHz	1 GHz- 9 GHz	0.5 GHz- 4 GHz	0.1 GHz-10 GHz	1.4 GHz to 8 GHz	3 GHz-8 GHz	2 GHz-4 GHz
Array type and geometry	synthetic cylindrical	synthetic hemispherical	synthetic cylindrical	synthetic cylindrical	stationary planar	synthetic cylindrical	hardware hemispherical	stationary wearable
Measurement type	frequency domain	time domain	frequency domain	frequency domain	frequency domain	frequency domain	frequency domain	time domain
Mechanical scanning	Yes	Yes	Yes	Yes	No	Yes	Yes	No
Coupling medium	Yes	No	No	Yes	No	Yes	No	No
Scan duration	5 min per breast	15 min per scan	7 min per breast	7 min per breast	N/A	20 min total scan	10 min	6 min per breast
Imaging method	quantitative	qualitative	qualitative	qualitative	quantitative	qualitative	qualitative	qualitative
Cohort	400	10 (all malignant)	353	24 (all with palpable cancer lumps)	15	115	225	1
Sensitivity	N/A	All cancers were detected.	82.3%	87.5%	N/A	63%	76%	N/A
Specificity	N/A		50%	N/A	N/A	N/A	N/A	N/A

Although the prototype allows for fast multi-view acquisition (25 sets of measurement in 15 seconds), it suffers from limitations in image resolution and a small field of view, which hinders its diagnostic capabilities.

The *Scan and Find Early* (*SAFE*) system, developed by a research group in Turkey [33], employs a mechanically scanned bistatic system in which both Tx and Rx antennas touch and circle around a coupling cylinder. In contrast to the *Wavelia* system, this prototype features a size-adjustable cup to accommodate various breast sizes. The cup is a part of the coupling cylinder. The total scanning time is approximately 20 minutes. Although it shows promise for practical use, the system's speed and image quality need further optimization for clinical settings.

Among the prototypes discussed in Table 1-2, the *MARIA* system features the largest number of antennas. It consists of a hardware array comprising 60 cavity-backed slot antennas arranged in a hemispherical configuration, operating across the 3 GHz to 8 GHz range. A dielectric fluid is placed between the breast and the scanning cup to eliminate air gaps, improving signal transmission. A custom-built electromechanical switch network multiplexes the 60 antennas over the 3 GHz to 8 GHz range, allowing for faster data acquisition. The antenna array and switch assembly rotate as a single unit around the breast cup to minimize image artifacts happens during imaging. The scanning time for MARIA is approximately 10 minutes per breast.

In the breast microwave imaging prototypes that employ more than two antennas (see Table 1-2), electromechanical or solid-state radio frequency (RF) switches are typically employed to multiplex the Tx and Rx antennas across the operational frequency range. Increasing the number of antennas often requires complex, cascaded RF-switched networks, which can introduce significant losses frequently exceeding 9 dB in the high-GHz UWB band. These losses affect the system's dynamic range and sensitivity, ultimately limiting the number of antennas in an RF-switched imaging systems. Consequently, most of these prototypes are based on synthetic or hardware arrays. Note that in clinical applications, faster data acquisition is highly desirable as it minimizes the time patients need to remain still, thereby reducing the adverse effects of patient movement and breathing during the scan. This can enhance image quality and overall diagnostic accuracy by mitigating motion artifacts [5].

Despite considerable improvements, the microwave breast imaging prototypes still remain within the research and development phase and are yet to transition into clinical use. This lag is attributed mainly to the prevailing problems in imaging speed, resolution, receiver sensitivity, and diagnostic sensitivity and specificity. Unfortunately, so far, they show diagnostic sensitivity and specificity falling short of what is required for effective breast-cancer screening, i.e., they are lower than those of mammography (cohort: USA only: 2,872,791, sensitivity: 82.3%, specificity: 83.2%). These problems are due to limitations in both the image reconstruction algorithms and the data acquisition hardware. Although there have been some recent improvements, the existing prototypes still cannot achieve the accuracy and efficiency that is necessary for reliable detection of breast cancer in a reasonable amount of time. Improvements are needed both in the algorithmic and the hardware domains to succeed in breaking the barriers to realizing microwave breast imaging technologies for routine use in clinical practice.

1.5 Research Objective

The ultimate goal of this research is to develop an innovative architecture for breast-cancer screening and detection. The proposed architecture is an electronically scanned compressed breast imager capable of multiplexing hundreds of antenna elements, which provide the fast data acquisition and the signal-to-noise ratio (SNR) necessary for real-time breast microwave imaging. The imager consists of two densely packed antenna arrays, each with 256 elements: one functioning as the Tx array and the other as the Rx array. Unlike previously reported systems (see Table 1-2), which are constrained to multiplexing tens of antenna elements due to excessive losses and interconnect challenges at UWB frequency range, this research introduces a novel multiplexing approach. Specifically, the multiplexing of the Rx array is performed at a single-tone intermediate frequency (IF) (e.g., 30 MHz), which offers several key benefits:

- simplified distribution networks design and implementation,
- reduced insertion loss (approximately 2 dB at 30 MHz versus ≥ 9 dB at 8 GHz in the UWB range),
- improved impedance match (return loss ≥ 25 dB compared to ~10 dB in UWB),
- enhanced channel isolation (≥ 65 dB compared to ~25 dB in the UWB systems).
- accurate phase and magnitude alignment across all 256 channels,
- leverage of the VNA dynamic range of ≥ 110 dB.

The proposed strategy mitigates some of the limitations of the traditional RF-switched systems, but it also introduces complexities, as each antenna element must be equipped with its own RF front-end, requiring careful integration and design optimization. To realize this vision, the proposed architecture integrates three primary modules:

- 2-port VNA with vector frequency-conversion (mixer) measurement capability,
- 16×16 UWB Tx array equipped with a 1:256 RF power-splitting feed network or an RF-switched feed network for versatile illumination patterns,
- 16×16 UWB active Rx array featuring an IF-switch network for channel multiplexing and a local oscillator (LO) power distribution network.

Chapter 3 provides a detailed description of the proposed breast microwave imaging architecture.

The main objectives of this research are the design, fabrication and evaluation of the different parts of the electronically scanned compressed breast imager, taking one step further toward the full realization of a real-time breast imager.

1.6 Contributions

The author has contributed to the development of the electronically scanned compressed breast imager in the following ways.

1. Design, fabrication, and evaluation of a multi-layer, large-scale planar UWB Rx array realized on printed circuit board (PCB) technology. Each antenna element within the array is equipped with an individual RF front-

end for signal amplification and down-conversion. However, due to spatial constraints, only the low-noise amplifiers (LNAs) are integrated directly onto the antenna array board, resulting in an active array configuration. The remaining RF front-end circuitry, including the mixers, the LO power distribution network and the IF switching network are housed on complementary vertical PCBs. This arrangement necessitates seamless and efficient board-to-board RF transitions to ensure optimal system performance and to maintain signal integrity.

2. An efficient interconnect has been developed to link the active Rx array to the remaining RF front-end circuitry (mixers, LO power distribution network and IF switching network), accommodated on separate vertical PCBs. The large active Rx array is compatible only with sub-miniature push-on sub-micro (SMPS) connectors, which are compact but costly, fragile, and limited in mating cycles. The dense packing of hundreds of these connectors on a PCB makes connections challenging and prone to unreliable electrical performance. To overcome these issues, high-speed vertical connectors (HSVCs), commonly used in computer technology, are adopted. An impedance matching technique is developed to ensure seamless RF transitions between the active Rx array PCB and the complementary vertical PCBs housing the remaining RF front-end circuitry through the HSVCs. This solution enhances mechanical robustness, reduces costs, and improves reliability. Additionally, the proposed board-to-board transition technique is applicable to other UWB systems requiring reliable microwave signal transfer across hundreds of channels.

3. A large planar UWB Tx array realized on PCB technology has been developed to work in tandem with the Rx array in the proposed breast microwave imager. This Tx array leverages HSVCs, enabling seamless integration with various RF feed networks. The Tx array enables the implementation of different illumination schemes for breast microwave imaging by allowing the insertion of various RF feed networks in the connectors. Two types of RF feed network PCBs are evaluated in this research: (i) a power-splitting feed network for simultaneous excitation of all antenna elements, and (ii) an RF-switched feed network for sequential excitation of individual elements.
4. The complementary vertical PCBs for the active Rx array, which include the mixers, the LO power distribution network, and the IF switching network, have been carefully designed and are now undergoing final revisions before being submitted for fabrication. Once fabrication and verification of these PCBs are complete, they will be integrated with the Rx active array alongside the Tx array and its RF feed network to realize an initial prototype of the breast microwave imaging system. This initial prototype will undergo experimental validation using a breast tissue phantom to assess its performance and refine the system for future clinical applications.

1.7 Outline of the Thesis

This thesis presents the hardware advancements achieved in developing a novel electronically scanned imager for the microwave imaging of the compressed breast.

Chapter 2 focuses on the design of a planar UWB active sensing array implemented on PCB technology for compressed breast microwave imaging. The spacing between antenna elements is 12×12 mm^2 in the lateral direction, making it the smallest element spacing proposed for breast microwave imaging. Each antenna element integrates an LNA, while a ground plane within the multi-layer structure separates the antenna array from the electronics and ensures back shielding and enhanced power coupling into the tissue. The design addresses a critical challenge in large, shielded antenna arrays for tissue imaging—establishing efficient interconnects between array elements and electronics through multiple dielectric layers and a grounded plane. The Rx array's performance is validated through simulations and measurements. This chapter is adapted from a manuscript published in the *IEEE Transactions on Antennas and Propagation* [17] with formatting modifications to improve legibility.

Chapter 3 introduces an efficient method to interconnect hundreds of grounded coplanar waveguide (GCPW) input/output signal paths on two separate PCBs (one horizontal and the other vertical) based on widely available low-cost HSVCs. This development enables the realization of large-scale high-density electronically scanned or switched antenna arrays, which are critical in wireless communications as well as in microwave radar, imaging and sensing. This chapter is duplicated from a manuscript published in the MDPI *Sensors* journal [36].

Chapter 4 details the design of a large planar UWB Tx array realized on PCB technology for the electronically scanned compressed breast microwave imager. The array shares geometric similarities with the Rx array and features a modular architecture with HSVCs to accommodate different RF feed network PCBs, offering various illumination schemes. Two RF feed network PCBs are developed: for simultaneous and sequential element excitation. The performance of the Tx array and the RF feed network PCBs is verified through simulations and measurements. This chapter is duplicated from a manuscript submitted to the *IEEE Transactions on Antennas and Propagation* [39].

Chapter 5 summarizes the ongoing tasks and key achievements in the development of the electronically scanned compressed breast microwave imager. It also offers recommendations for future research aimed at advancing further the hardware of this breast microwave imaging system.

1.8 References

[1] *Breast Cancer*. World Health Organization. Accessed: Nov. 24, 2024. [Online]. Available: https://www.who.int/news-room/fact-sheets/detail/breast-cancer

[2] N.K., Nikolova. "Microwave imaging for breast cancer," *IEEE Microw. Mag.*, vol. 12, no. 7, pp.78-94, Dec. 2011.

[3] E. Tedeschi, F. Caranci; F. Giordano; V. Angelini; S. Cocozza; and A. Brunetti, "Gadolinium retention in the body: What we know and what we can do," *La Radiol. Med.*, vol. 122, pp. 589–600, Aug. 2017.

[4] L.E. Larsen, and J.H. Jacobi, "Medical Applications of Microwave Imaging," vol. 32. New York, NY, USA: *IEEE Press*, 1986.

[5] D. O'Loughlin, M. O'Halloran, B.M. Moloney, M. Glavin, E. Jones, and M.A. Elahi, "Microwave breast imaging: Clinical advances and remaining challenges," *IEEE Trans. Biomed. Eng.*, vol. 65, no. 11, pp. 2580-2590, Feb. 2018.

[6] D. Bhargava, P. Rattanadecho, and K. Jiamjiroch, "Microwave imaging for breast Cancer detection-A Comprehensive review," *Eng. Sci.*, vol. 30, pp. 1116, Mar. 2024.

[7] J. C. Lin, "Frequency optimization for microwave imaging of biological tissues," *Proc. IEEE,* vol. 73, no. 2, pp. 374–375, Feb. 1985.

[8] H.M. El Misilmani, T. Naous, S.K. Al Khatib, and K.Y. Kabalan, "A survey on antenna designs for breast cancer detection using microwave imaging," *IEEE Access*, vol.8, pp.102570-102594, Jun. 2020.

[9] B. Borja, J.A. Tirado-Mendez, and H. Jardon-Aguilar, "An overview of UWB antennas for microwave imaging systems for cancer detection purposes," *Prog. Electromagn. Res. B*, vol. 80, pp. 173-198, May 2018.

[10] M.Z. Mahmud, M.T. Islam, N. Misran, A.F. Almutairi, and M. Cho, "Ultra-wideband (UWB) antenna sensor-based microwave breast imaging: A review," *Sensors*, vol.18, no. 9, pp. 2951, Sep. 2018.

[11] T. Sugitani, S.I. Kubota, S.I. Kuroki, K. Sogo, K. Arihiro, M. Okada, T. Kadoya, M. Hide, M. Oda, and T. Kikkawa, "Complex permittivities of breast tumor tissues obtained from cancer surgeries," *Appl. Phys. Lett.*, vol.104, no. 25, Jun. 2014.

[12] W. Shao, and T. McCollough, "Advances in microwave near-field imaging: Prototypes, systems, and applications," *IEEE Microw. Mag.*, vol. 21, no. 5, pp. 94-119, Mar. 2020.

[13] H. Bahramiabarghouei, E. Porter, A. Santorelli, B. Gosselin, M. Popović, and L.A. Rusch, "Flexible 16 antenna array for microwave breast cancer detection," *IEEE Trans. Biomed. Eng.*, vol. 62, no. 10, pp. 2516-2525, May 2015.

[14] S. Latif, Saeed, D. Flores-Tapia, S. Pistorius, and L. Shafai "A planar ultrawideband elliptical monopole antenna with reflector for breast microwave imaging," *Microw. Opt. Technol. Lett*., vol. 56, no. 4, pp. 808-813, Apr. 2014.

[15] I. Amdaouch, O. Aghzout, A. Naghar, A.V. Alejos, and F. Falcone, "Enhanced accuracy of breast cancer detection based on UWB compact slotted monopole antennas," *Adv. Electromagn.*, vol. 8, no. 5, pp. 1-6, Dec. 2019.

[16] M. Ahadi, J. Nourinia, and C. Ghobadi, “Square monopole antenna application in localization of tumors in three dimensions by confocal microwave imaging for breast cancer detection: Experimental measurement,” *Wirel. Pers. Commun.*, vol. 116, pp. 2391-2409, Feb. 2021.

[17] N. V. Shahmirzadi, V. Tyagi, J. Nguyen, R. Kazemivala, N. K. Nikolova, and C.H. Chen, “Planar array of UWB active slot antennas for microwave imaging of the breast,” *IEEE Trans. Antennas Propag.*, vol. 71, no. 4, pp. 2946-2957, Jan. 2023.

[18] T. Sugitani, K. Shinichi, T. Akihiro, X. Xiao, and T. Kikkawa, “A Compact 4 4 Planar UWB Antenna Array for 3-D Breast Cancer Detection,” *IEEE Antennas Wirel. Propag. Lett.*, vol. 12, pp.733-736, Jun. 2013.

[19] M. Adachi, T. Nakagawa, T. Fujioka, M. Mori, K. Kubota, G. Oda and T. Kikkawa, “Feasibility of portable microwave imaging device for breast cancer detection,” *Diagnostics*, vol. 12, no. 1, pp. 27, Dec. 2021.

[20] M. Klemm, J.A. Leendertz, D. Gibbins, I J. Craddock, A. Preece, and R. Benjamin, “Microwave radar-based differential breast cancer imaging: Imaging in homogeneous breast phantoms and low contrast scenarios,” *IEEE Trans. Antennas Propag.*, vol. 58, no. 7, pp. 2337-2344, Apr. 2010.

[21] A.W. Preece, I. Craddock, M. Shere, L. Jones, and H.L. Winton, “MARIA M4: clinical evaluation of a prototype ultrawideband radar scanner for breast cancer detection,” *J. Med. Imaging*, vol. 3, no. 3, pp. 033502-033502, Jul. 2016.

[22] R.K. Amineh, M. Ravan, A. Trehan, and N.K. Nikolova, “Near-field microwave imaging based on aperture raster scanning with TEM horn

antennas," *IEEE Trans. Antennas Propag.*, vol. 59, no. 3, pp. 928-940, Dec. 2010.

[23] S. Diana, D. Brizi, C. Ciampalini, G. Nenna, and A. Monorchio, "A compact double-ridged horn antenna for ultra-wide band microwave imaging," *IEEE Open J. Antennas Propag.*, vol. 2, pp. 738-745, Jun. 2021.

[24] Bourqui, and E.C. Fear, "Shielded UWB sensor for biomedical applications," *IEEE Antennas Wirel. Propag. Lett.*, vol. 11, pp. 1614-1617, Dec. 2012.

[25] M.T. Islam, M.Z. Mahmud, M.T. Islam, S. Kibria, and M. Samsuzzaman, "A low cost and portable microwave imaging system for breast tumor detection using UWB directional antenna array," *Sci. Rep.*, vol. 9, no. 1, pp. 1-13, Oct. 2019.

[26] D.A. Sánchez-Bayuela, N. Ghavami, C.R. Castellano, A. Bigotti, M. Badia, L. Papini, G. Raspa, G. Palomba, M. Ghavami, R. Loretoni, and M. Calabrese, "A multicentric, single-arm, prospective, stratified clinical investigation to evaluate MammoWave's ability in breast lesions detection," *PLoS One*, vol. 18, no. 7, pp. e0288312, Jul. 2023.

[27] B. M. Moloney, P.F. McAnena, S.M. Abd Elwahab, A. Fasoula, L. Duchesne, J.D.G. Cano, C. Glynn, A. O'Connell, R. Ennis, A.J. Lowery, and M.J. Kerin, "Microwave imaging in breast cancer–results from the first-in-human clinical investigation of the wavelia system," *Acad. Radiol.*, vol. 29, pp. S211-S222, Jan. 2022.

[28] H.T Sediq, J. Nourinia, C. Ghobadi, and B. Mohammadi, "A novel shaped ultrawideband fractal antenna for medical purposes," *Biomed. Signal Process. Control*, vol. 80, pp. 104363, Feb. 2023.

[29] M.A. Khan, U. Rafique, H.Ş. Savci, A.N. Nordin, S.H. Kiani, and S.M. Abbas, "Ultra-wideband pentagonal fractal antenna with stable radiation characteristics for microwave imaging applications," *Electronics*, vol. 11, no. 13, pp. 2061, Jun. 2022.

[30] M. Alibakhshikenari, B.S. Virdee, P. Shukla, N.O. Ojaroudi, L. Azpilicueta, C.H. See, R. A. Abd-Alhameed, F. Falcone, I. Huynen, T.A. Denidni and E. Limiti, "Metamaterial-inspired antenna array for application in microwave breast imaging systems for tumor detection," *IEEE Access*, vol. 8, pp. 174667-174678, Sep. 2020.,

[31] M.T. Islam, M.T. Islam, M. Samsuzzaman, H. Arshad, and H. Rmili. "Metamaterial loaded nine high gain vivaldi antennas array for microwave breast imaging application," *IEEE Access*, vol. 8, pp. 227678-227689, Dec. 2020.

[32] T.M. Grzegorczyk, P.M. Meaney, P.A. Kaufman, and K.D. Paulsen, "Fast 3-D tomographic microwave imaging for breast cancer detection," *IEEE Trans. Med. Imaging*., vol. 31, no. 8, pp. 1584-1592, May 2012.

[33] A. Janjic, M. Cayoren, I. Akduman, T. Yilma, E. Onemli, O. Bugdayc, M.E. Aribal, "SAFE: A novel microwave imaging system design for breast cancer screening and early detection—Clinical evaluation," *Diagnostics*, vol. 1, no. 3, pp. 533, Mar. 2021.

[34] E. Porter, H. Bahrami, A. Santorelli, B. Gosselin, L.A. Rusch, and M. Popović, "A wearable microwave antenna array for time-domain breast tumor screening," *IEEE Trans. Med. Imaging*, vol. 35, no. 6, pp. 1501-1509, Jan. 2016.

[35] K. Smith, J. Bourqui, D. Garrett, S. Zarnke, M. Owjimehr, D. Deutscher, T. Fung, and E. Fear, "Microwave imaging of the breast: Consistency of measurements over time," *IEEE J. Electromagn. RF Microwaves Med. Biol.*, vo. 6, no. 1, pp. 61-67, Jul. 2021.

[36] N. V. Shahmirzadi, N. K. Nikolova, and C. H. Chen, "Interconnect for dense electronically scanned antenna array using high-speed vertical connector," *Sensors*, vol. 23, no. 20, article 8596, Oct. 2023.

[37] M. Shere, I. Lyburn, R. Sidebottom, H. Massey, C. Gillett, and L. Jones, "MARIA® M5: A multicentre clinical study to evaluate the ability of the Micrima radio-wave radar breast imaging system (MARIA®) to detect lesions in the symptomatic breast," *Eur. J. Radiol.*, vol. 116, pp. 61-67.

[38] R. Sidebottom, D. Webb, B. Bishop, M. Kabir, S. Allen, "Results for the London investigation into dielectric scanning of lesions study of the MARIA M6 breast imaging system," *Br. J. Radiol*., vol. 97, pp. 549–552, Mar. 2024.

[39] N.V. Shahmirzadi, A. D Pitcher, N. K. Nikolova, and C.H. Chen, "Transmitting Array for an Electronically Switched Microwave Breast Imager," *IEEE Trans. Antennas Propag.*, submitted, Nov. 2024.

Chapter 2

2. Planar Array of UWB Active Slot Antennas for Microwave Imaging of the Breast

Preface

This chapter is a reproduction of the following published article:

N. V. Shahmirzadi, V. Tyagi, J. Nguyen, R. Kazemivala, N. K. Nikolova, and C.H. Chen, “Planar array of UWB active slot antennas for microwave imaging of the breast,” *IEEE Transactions on Antennas and Propagation*, vol. 71, no. 4, pp. 2946-2957, Jan. 2023.

Author Contributions: Conceptualization, N. K. Nikolova; methodology, N. V. Shahmirzadi, V. Tyagi, N. K. Nikolova, and C.-H. Chen; validation, N. V. Shahmirzadi, V. Tyagi, and N. K. Nikolova; investigation, N. V. Shahmirzadi, V. Tyagi, J. Nguyen, R. Kazemivala, N. K. Nikolova, and C.-H. Chen; resources, N.

K. Nikolova; writing—original draft preparation, N. V. Shahmirzadi, V. Tyagi; writing—review and editing, N. V. Shahmirzadi, N. K. Nikolova, J. Nguyen, R. Kazemivala, and C.-H. Chen; supervision, N. K. Nikolova, and C.-H. Chen; project administration, N. K. Nikolova; funding acquisition, N. K. Nikolova

2.1 Introduction

Early-stage diagnosis of breast cancer is vital to the reduction of mortality rates among women; thus, annual or biennial breast-cancer screening is recommended for at-risk age groups [1], [2]. The primary diagnostic tool is X-ray mammography. Since X-rays are a form of ionizing radiation, the exam frequency is limited. Difficult trade-offs are made to maximize tumor detection while minimizing the risk to the patient, leading to loss of contrast and low sensitivity in dense breasts [3], [4]. Substantial, often painful, compression is required to offset these limitations [5]. These factors, along with the need for trained personnel to safely operate the X-ray apparatus, make breast-cancer screening far less effective than the expectations of healthcare professionals [6], [7]. Breast cancer remains a leading cause of premature mortality in women [8], and new technologies are explored to improve screening in terms of diagnostic accuracy (e.g., better sensitivity in dense tissue), increased frequency of check-ups, and wider accessibility. Complementary imaging through ultrasound [8], [10] and magnetic resonance imaging (MRI) of high-risk groups [11], [12] improve the diagnostic accuracy in screening, but they, too, require specialized equipment and trained personnel available only at the few cancer clinics.

Microwave imaging has been explored in the last three decades [13]-[20] as an alternative modality for breast-cancer screening. Its advantages are in the low equipment cost and size, the nonionizing radiation, and the promise for portable, even wearable deployment [16]. The optimum frequency range for tissue microwave imaging has been the subject of numerous studies [22]-[24]. The low GHz ultra-wideband (UWB) range has been identified as a good compromise between penetration and spatial resolution. The current design targets the frequency range from 3 GHz to 8 GHz.

The advancement in clinical practice for microwave imaging of breast is yet to come. To this end, fast acquisition systems are needed that provide repeatable measurements over hundreds of spatial samples within minutes with a large dynamic range and signal-to-clutter ratio. Thus, electronically scanned antenna arrays are required. Mechanical scanning, even if partial, is slow and may introduce positioning errors. The main challenge in the design of tissue-imaging electronic scanners is the need to multiplex hundreds of antennas, both transmitting (Tx) and receiving (Rx). Such multiplexing is not provided by benchtop vector network analyzers (VNAs), which, even if equipped with RF switching networks, are limited to about 16 ports. This is why custom RF-switching networks are common [13]-[16], [21] and even then, the maximum achieved number of multiplexed ports is 60 [15]. A larger number of multiplexed ports entails increasingly complex, often cascaded, RF-switch networks, the losses of which easily exceed 6 dB in the low-GHz UWB band. The losses impact the system's dynamic range and sensitivity, which puts a limit on the RF-switch network complexity. This is the main reason why most of the prototypes augment the electronic scanning, based on RF switching, with mechanical scanning [13], [14], [17]-[21]. The complementary mechanical scan also allows for denser spatial sampling while relaxing the size requirement for the sensing antenna elements.

Many antenna types have been explored for tissue measurements [24]. What distinguishes the antenna elements suitable for large dense arrays is the strict limitation on the size along with the requirement for low inter-element coupling (e.g., below −20 dB). The size limit stems from the desired spatial sampling step, which is usually set to be equal to or less than the minimum wavelength in the tissue [19]. Thus, the array elements must be electrically small, which makes the UWB impedance match challenging, and they also must be densely packed, which makes their decoupling challenging. The shielded and cavity-backed slot-antenna designs [15], [16], [25]-[29] , have emerged as a preferred choice due to small size, unidirectional radiation, smooth near-field distribution, and compatibility with printed circuit board (PCB) technology.

The first active antenna arrays for breast imaging have been reported in [27], [28], where each element is equipped with a low-noise amplifier (LNA) to improve the system sensitivity and dynamic range. We note that antenna integration with active components (e.g., p-i-n diodes and LNAs) is common in wireless energy harvesting [30], [31], communications [32]-[35], and imaging [27], [28], [36]. However, there is a major deficiency in the prior shielded slot-antenna designs [27], [28], which prevents their implementation into large active arrays consisting of hundreds of elements. In [27], each array element is terminated with a coaxial connector soldered on the metallization layer of the antenna feed underneath the ground shield. The connector leads into a separate LNA PCB. Thus, the implementation of the shielding structure above the fork layer requires the manual drilling of large openings to access the connector pads onto which the connectors are subsequently soldered manually. The fabrication is thus impractical when large arrays are to be implemented on a single multi-layer PCB. Moreover, the openings degrade the shield integrity. The design in [28] has succeeded in integrating an LNA chip with a very small footprint at each antenna feed. But the LNA output is still terminated with a coaxial connector soldered at the antenna feed, i.e., below the shield. Thus, a large opening is still needed at each antenna to accommodate the coaxial connector and the LNA chip, both of which are soldered manually.

Here, we address this deficiency by moving the LNA array to the exposed top layer of the active-antenna PCB, allowing for automated surface mount of electronics and connectors. The new design ensures high shield integrity by eliminating the need for drilled openings. The main design challenge is the vertical signal transition of substantial length, which is commensurate with the size of the slot. This transition is not amenable to analytical modelling since it traverses through dielectric layers of various permittivities and thicknesses as well as through the ground plane. Also, it resides close to the slot feed, thereby affecting the antenna input impedance. Here, we report a successful triple-wire (ground-signal-ground) vertical transition from the coplanar-waveguide (CPW) antenna feed to the CPW feed of an LNA chip on the PCB top layer. Additionally, new design features in the antenna feed improve the impedance match and the element de-coupling in the entire frequency band from 3 GHz to 8 GHz, when compared to the arrays reported in [27], [28]. The main impact of this work is that it enables the construction of large active arrays of shielded slot antennas on a single PCB with excellent signal integrity and low fabrication cost.

The ability to surface-mount hundreds of chips and various connectors is of paramount importance to the envisioned electronically scanned imager. The proposed active antenna array is to be interfaced with a matching array of mixer chips so that each sensing element outputs a signal at an intermediate frequency (IF) of 30 MHz, at which the multiplexing is performed. Unlike a UWB RF-switch network, the IF-switch network operates at a single-tone low frequency with negligible loss, excellent impedance match and decoupling better than −60 dB. This allows for the multiplexing of hundreds of sensors, thus overcoming the main limitation of the current RF-switched arrays employed in tissue imaging.

Section II presents the design of the passive antenna array along with simulation and measurement results. Section III presents the design, simulation, and measurement of the active array, wherein each antenna is equipped with an LNA. Section IV provides results from imaging experiments employing both passive and active elements in an array prototype.

2.2 Passive Sensing Array

2.2.1 Design Goals

The design goals for the passive antenna array in the frequency band from 3 GHz to 8 GHz are as follows. First, the reflection coefficient at the terminals of each passive element in the presence of the breast tissue must be equal to or less than −10 dB for a good impedance match.

Second, the mutual coupling between neighboring elements must be less than −20 dB. The mutual coupling is a source of signal clutter. If two neighboring elements form a transmit-receive pair, a mutual coupling signal in excess of −20 dB is sufficiently strong to mask the weak back-scattering signal. Moreover, in near-field measurements such as those in tissue imaging, the measured object alters the mutual-coupling signal as compared to the one obtained with the background medium alone, which makes the background de-embedding difficult. The reduction of the mutual coupling is also desirable if the two neighboring elements are both receiving, which is the case here. A UWB antenna element cannot be perfectly impedance-matched in the whole frequency band. Even under conditions of perfect impedance match and no loss, half of the incident-wave power intercepted by the antenna is scattered back [37]. Thus, each Rx element is a secondary source of radiation, and the power it injects back into the object is a source of clutter to its neighbors if the mutual coupling is significant. Therefore, the low inter-element coupling is an important performance metric of all densely packed imaging arrays.

Third, the center-to-center distance between the elements must be equal to or less than 12 mm in both x and y directions as dictated by the shortest wavelength (at 8 GHz) in a tissue medium with relative permittivity of about 10.

Fourth, the array must be fully shielded from the back for unidirectional radiation toward the tissue and for minimal external interference.

Fifth, all electronics (e.g., LNA chips and circuits) and all connectors must be placed on the top metallization layer for easy access and surface mount. The shielding ground plane must isolate the passive antenna elements from the electronics layer, allowing only for the vertical interconnects to carry the signal from the antennas to their respective LNAs.

2.2.2 Structure of the Antenna Element and the Array

The proposed UWB sensing array is composed of slot antenna elements on a multi-layer PCB with a center-to-center distance of 12 mm, both in the *x*- and *y*-directions. The layer stack-up is shown in Figure 2-1, along with the respective thicknesses in the color-coded table. There are four metallization layers: the electronics layer (metal layer 1), the shield layer (metal layer 2), the antenna-feed layer (metal layer 3), and the slot layer (metal layer 4). The geometry of a single array element in each layer is described in Figure 2-2a (metal layer 4), Figure 2-2b (metal layer 3), Figure 2-2c (metal layer 2), and Figure 2-2d (metal layer 1). The antenna-slot layer (metal layer 4) comes in contact with the breast tissue.

The dimensions of the slot and the metallic patch within which the slot resides are shown in Figure 2-2a. The slot is electromagnetically coupled to a fork residing in metal layer 3, shown in Figure 2-2b. The fork's output transitions into a CPW. The CPW, in turn, transfers the signal to the low-reflection triple-wire vertical transition that carries the signal through the shield (metal layer 2, shown in

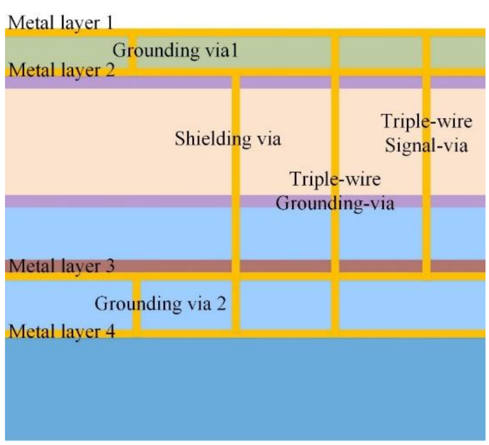

(a)

	Materials	Thickness (mm)
	Rogers 3035 (ε_r 3.5, tanδ 0.0015)	0.25
	FR4 (ε_r 4.34, tanδ 0.02)	2.5
	Rogers RT/Duroid 6010LM (ε_r 10.2, tanδ 0.0023)	0.635
	Copper	1 oz
	Fastrise (ε_r 6.15)	0.14
	Fastrise (ε_r 2.74)	0.14
	Tissue layer (ε_r 9.6, tanδ 0.4)	33

(b)

Figure 2-1: (a) Multi-layer stack-up of the PCB along with the various via-holes deployed in the structure. (b) Color-coded table showing the thickness and material property of the materials in the stack-up.

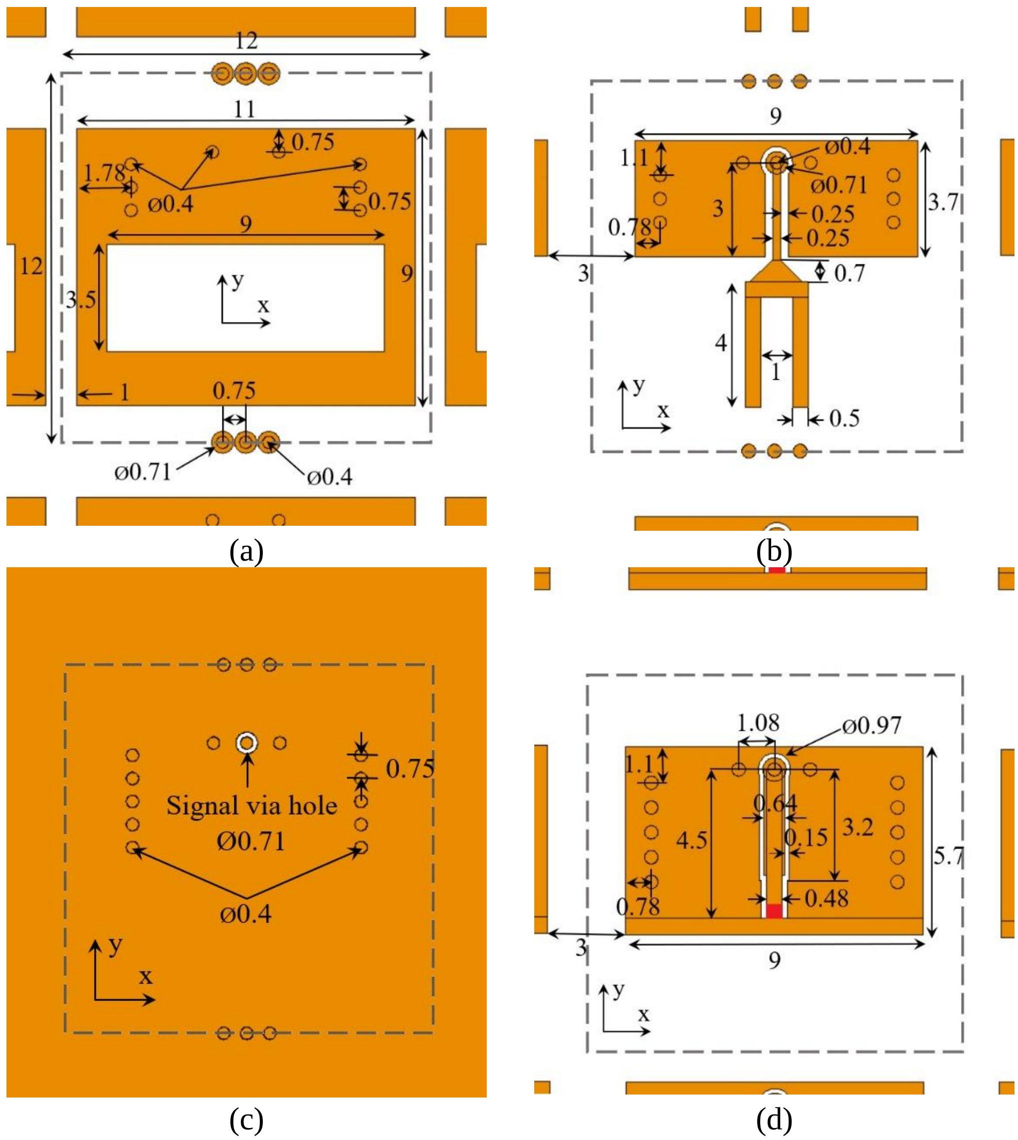

Figure 2-2: Layout and dimensions (in mm) of one element in: (a) slot layer (metal layer 4), (b) antenna-feed layer (metal layer 3), (c) shield layer (metal layer 2) and (d) electronics layer (metal layer 1). The dash-line shows the area of 12×12 mm^2 occupied by each element.

Figure 2-2c), and onto the electronics layer on top (metal layer 1, shown in Figure 2-2d).

The shield (see Figure 2-2c) is a grounded metallic plane, which extends over the entire array to isolate the antenna elements from the electronics layer. It also ensures unidirectional power delivery toward the tissue. It only allows for the center wire (a via-hole) of the triple-wire vertical interconnect to go through an opening in order to carry the signal from each antenna element to its respective LNA in the electronics layer. The shield layer impacts the antenna input impedance [27]; thus, the number of dielectric layers between the antenna-feed layer and the shield, their permittivities, and their thicknesses have been chosen to ensure a good impedance match. The shield has no observable impact on the antenna radiation efficiency, i.e., changing the material from copper to perfect electric conductor (PEC) in the simulation does not change the result. We reiterate that the shield is critical for a high front-to-back ratio. Since the proposed design eliminates the need to drill holes in the shielding, the back-radiation is eliminated.

The electronics layer (see Figure 2-2d) consists of another CPW, which connects the triple-wire output to terminals represented by lumped ports in the simulations [38].

The design employs many via-holes, which are indicated by the circles in Figure 2-2. Short grounding via-holes (Grounding via 1 in Figure 2-1a) ensure proper grounding of the CPW at the electronics layer to the shield; see Figure 2-2c and Figure 2-2d. Similarly, short via-holes (Grounding via 2 in Figure 2-1a) ground the CPW at the fork layer to the metallic patches in which the slots are cut out; see Figure 2-2a and Figure 2-2b. Additionally, two long grounding via-holes serve to form the ground wires in the triple-wire vertical transition, seen in all four layers shown in Figure 2-2. These are located symmetrically on both sides of the long signal via-hole, which connects the signal trace of the CPW at the fork layer to the signal trace of the CPW at the electronics layer. Finally, behind the triple-wire vertical transition of each element, there is a group of three long shielding via-holes, which are introduced to reduce the mutual coupling between neighboring elements along the *y*-axis. They extend from the shield layer (metal layer 2) to the antenna-slot layer (metal layer 4).

In order to achieve a good impedance match from 3 GHz to 8 GHz, significant effort has been dedicated to optimizing the size of the antenna slots, the shape of the antenna feed, particularly the transition from the fork to the CPW feed, as well the step CPW transition at the electronics layer. A fork-like stub feed is known to enhance the bandwidth of the slot antenna [29], [38] compared to a single microstrip feed. This is also the case in the current design. Based on simulation results, the fractional bandwidth with a simple microstrip feed probe is about 58%, which is improved to 91% by the fork-shaped feed designed here.

The design of the triple-wire transition in this array is challenging since it not only traverses through different dielectric layers (in thickness and permittivity) but also passes through the shield layer. The radius and center-to-center distance of this triple-wire transition (see Figure 2-2d) have been optimized to achieve a reflection coefficient well below −10 dB on both ports (on the electronics layer and the fork layer) and a transmission coefficient better than −1 dB over the whole frequency range. Moreover, this triple-wire transition is long and thus introduces parasitic inductive reactance in the element's input impedance as observed from its port. This is counteracted by the stepped-line transition from the triple-wire connection points to the element's port.

Various techniques have been used to reduce the mutual coupling in densely packed arrays [40], [41]. In this design, two strategies have been employed. First, the long shielding via-holes described before (see also Figure 2-3) ensure the decoupling of the triple-wire vertical transition of one element from the strong

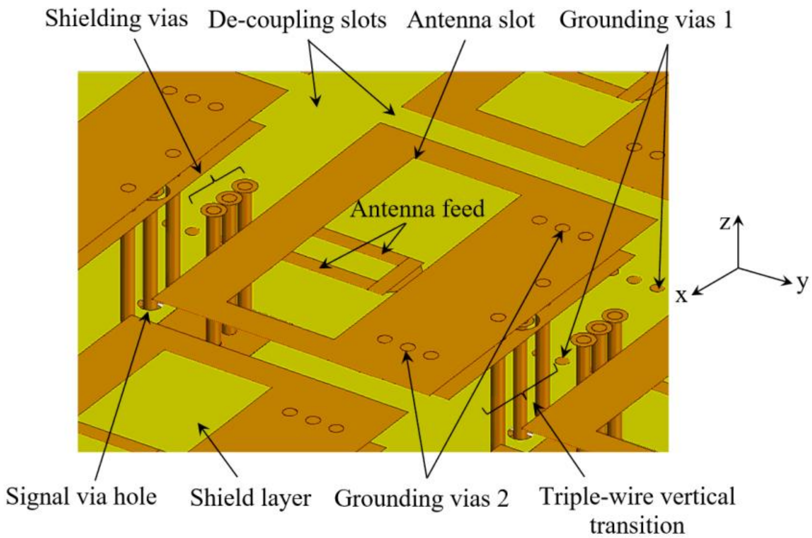

Figure 2-3: Isometric view of the metallic parts of the array. The antenna-slot layer, antenna-feed layer, and shielding layer can be observed. The electronics layer is masked by the grounding shield layer. The de-coupling slots both in the x and y directions as well as the shielding vias are also visible.

electric field of the neighboring slot. The position of these vias has been carefully chosen to block the *y*-polarized slot field, which is the strongest in the slot center (sinusoidal distribution). In the absence of these vias, the mutual coupling violates the −20 dB design goal at frequencies from 3 GHz to 4 GHz. The second strategy is to introduce decoupling slots in both the *x*- and *y*- directions in the slot layer as shown in Figure 2-3.

2.2.3 Passive Array Antenna Performance

The impedance match and the mutual coupling of a 6×6 antenna array are analyzed using the full-wave simulator HFSS [37] in a 3-port *S*-parameter configuration using lumped-port excitation with a frequency sweep from 3 GHz to 8 GHz. Figure 2-4. shows the overall size of the 6×6 array along with the port assignment in HFSS. The excitation is provided using a lumped port, whereas the actual excitation in the array prototype is provided through a sub- miniature push-on sub-micro (SMPS) coaxial connector (see Figure 2-5a). The SMPS connectors

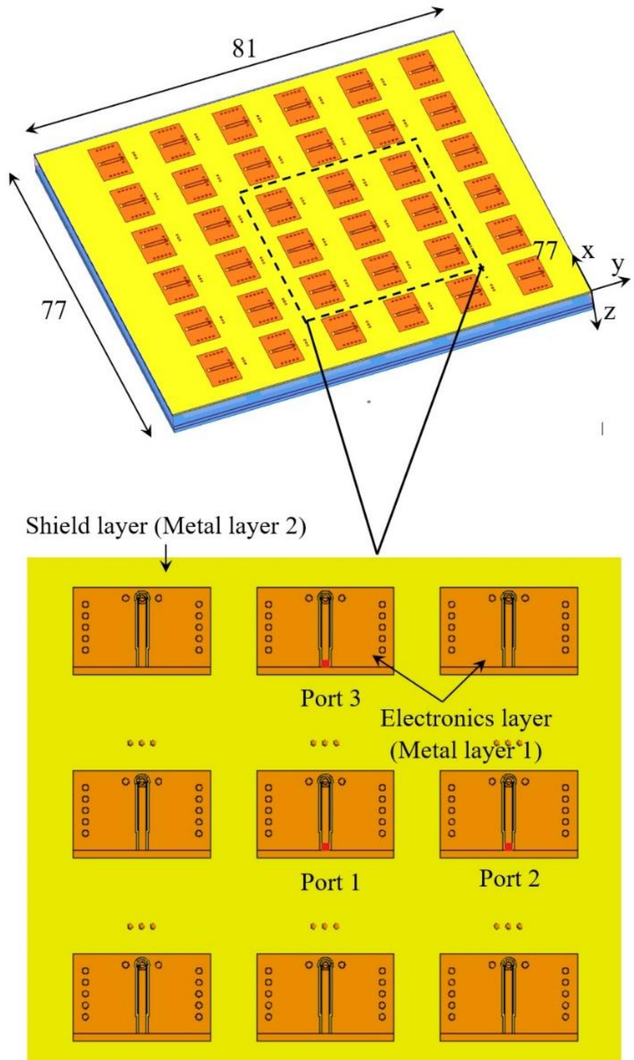

Figure 2-4: The dimensions of 6 by 6 array antenna (in mm) and the port assignment used in the simulation of the passive array. The electronics layer is shown in brown whereas the shield layer is in yellow.

are not included in the simulation because of prohibitive computational time.

In the simulation, the tissue layer is modelled by a 33 mm lossy dielectric material with a complex relative permittivity of $\varepsilon_{\mathrm{r}} \approx 9.6 - \mathrm{i}3.8$, which is selected to match approximately the average permittivity of BI-RADS Type 2 breast tissue [42], [43]. The breast tissue phantom used in the experiments presented in this section and in Section 2.4 is a stack of three 11 mm thick custom-made carbon rubber slabs with averaged complex permittivity of $\varepsilon_r \approx 9.6 - i3.8$ over the frequency band from 3 GHz to 8 GHz (see Figure 2-5c).

The simulated S-parameters of the passive array are shown in Figure 2-6. The reflection coefficients at Port 1 and Port 2 (see Figure 2-4) satisfy the goal of being below −10 dB from 3 GHz to 8 GHz. The mutual-coupling S-parameters, S_{21} and S_{31}, are shown in Figure 2-6b and Figure 2-6c in dB. The coupling values in the x-direction (S_{21}) and y-direction (S_{31}) are well below −20 dB in the whole frequency band, fulfilling the design goal.

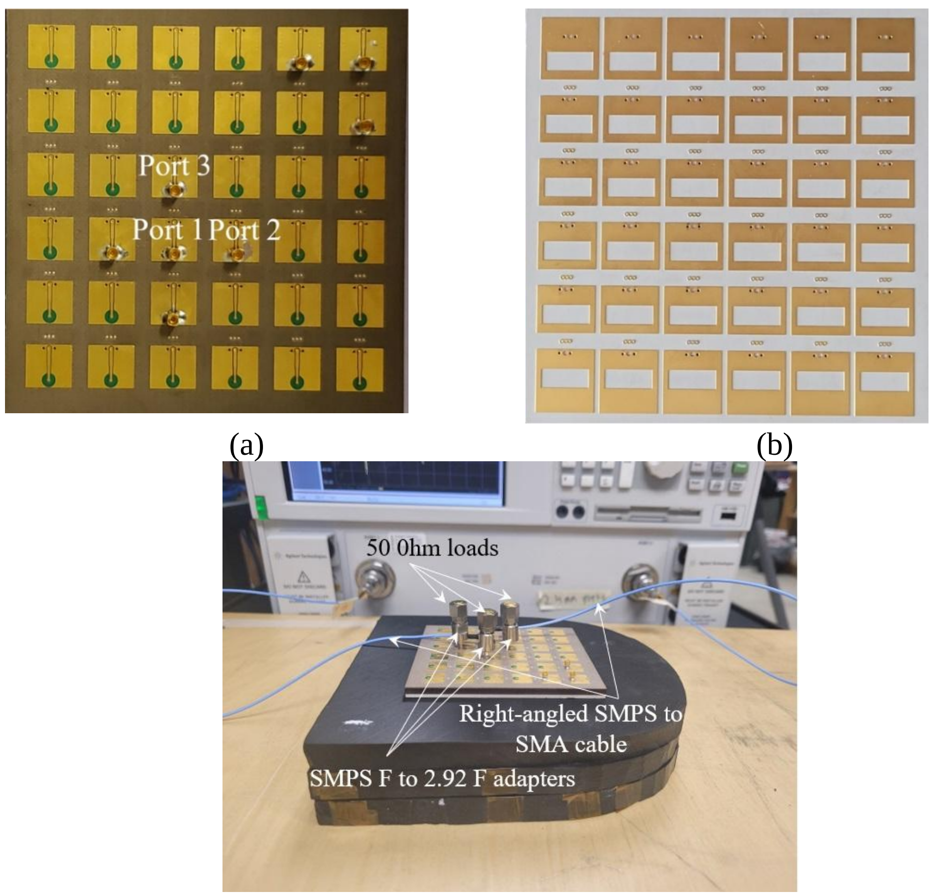

(c)

Figure 2-5: Photo of the fabricated 6×6 passive antenna array showing: (a) the electronics layer with the SMPS connectors, (b) the antenna slot layer, and (c) the measurement setup. The element at Port1 is connected to Port 1 of the VNA, while one of the neighboring elements is connected to Port 2. The remaining elements are loaded with 50 Ω SMA loads using SMPS F to 2.92 F adapters.

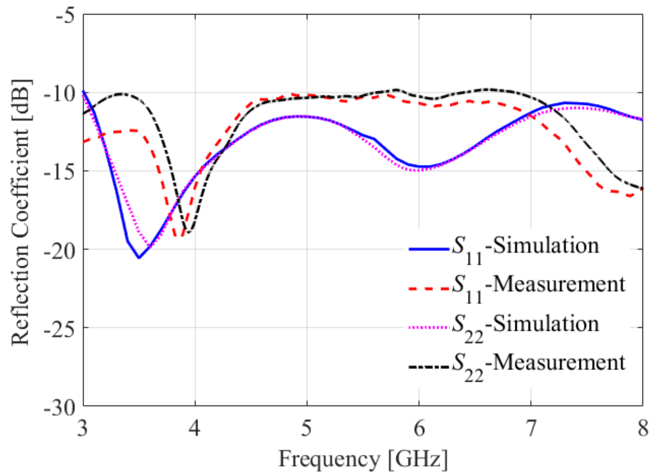

(a)

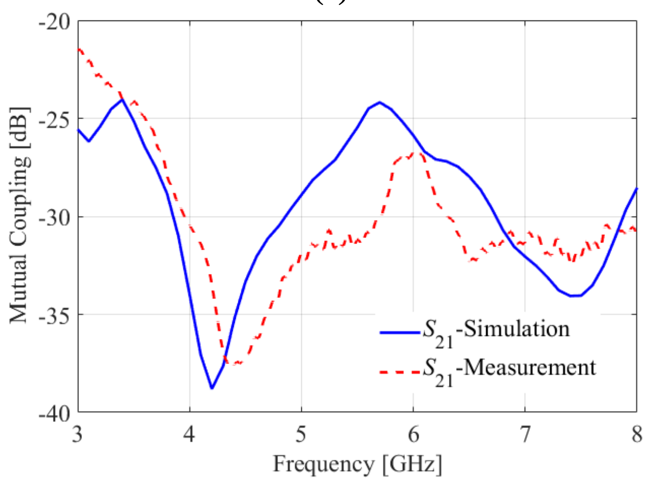

(b)

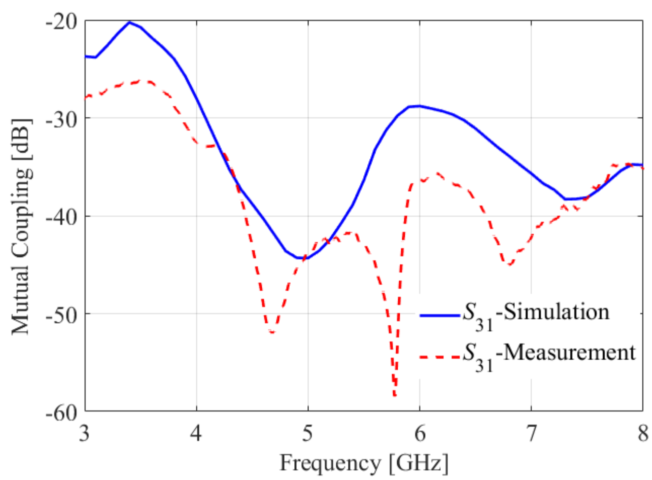

(c)

Figure 2-6: (a) Simulated and measured reflection coefficients. (b) Simulated and measured mutual coupling between the center element and the element at Port 2 (as indicated in Figure 2-4and Figure 2-5(a). (c) Simulated and measured mutual coupling between the center element and the element at Port 3.

A prototype of the passive array antenna has been fabricated consisting of 36 (6×6) elements terminated with SMPS coaxial connectors (see Figure 2-5a). The antenna board is placed on a 33 mm thick stack of three custom-made carbon-rubber slabs (each 11 mm thick) with averaged relative permittivity of $\varepsilon_{\mathrm{r}} \approx 9.6 - \mathrm{i}3.8$ (see Figure 2-5c), same as in the simulation. Port 1 of the array (see Figure 2-5a) is connected to Port 1 of the vector network analyzer (VNA) (E8363B, Keysight Technologies), whereas one of the neighboring elements is connected to Port 2 of the VNA. Both connections use right-angled SMPS female-to-sub-miniature version A (SMA) cables of 41 cm in length. The remaining elements are loaded with 50 Ω SMA terminations using SMPS female to 2.92 female adapters.

The measured *S*-parameters are shown in Figure 2-6, along with the simulated ones. The measured S_{11} and S_{22} (Figure 2-6a) confirm the satisfactory impedance match in the desired frequency band. S_{33} has also been measured. It is similar to S_{11} and S_{22}, but it is not shown in order to keep the number of curves in Figure 2-6a reasonable. The measured coupling parameters S_{21} and S_{31}, shown in Figure 2-6b and Figure 2-6c, respectively, are safely below the −20 dB threshold. From the plots in Figure 2-6, it is evident that discrepancies exist between the simulated and measured results. They are due to the fact that in simulations, lumped ports are used to excite the antenna elements, whereas the actual prototype is excited through SMPS coaxial connectors. This is a major factor since the input impedance is impacted strongly by the port model.

2.2.4 Near-field Radiation Characteristics

Another important performance parameter is the near-field distribution of

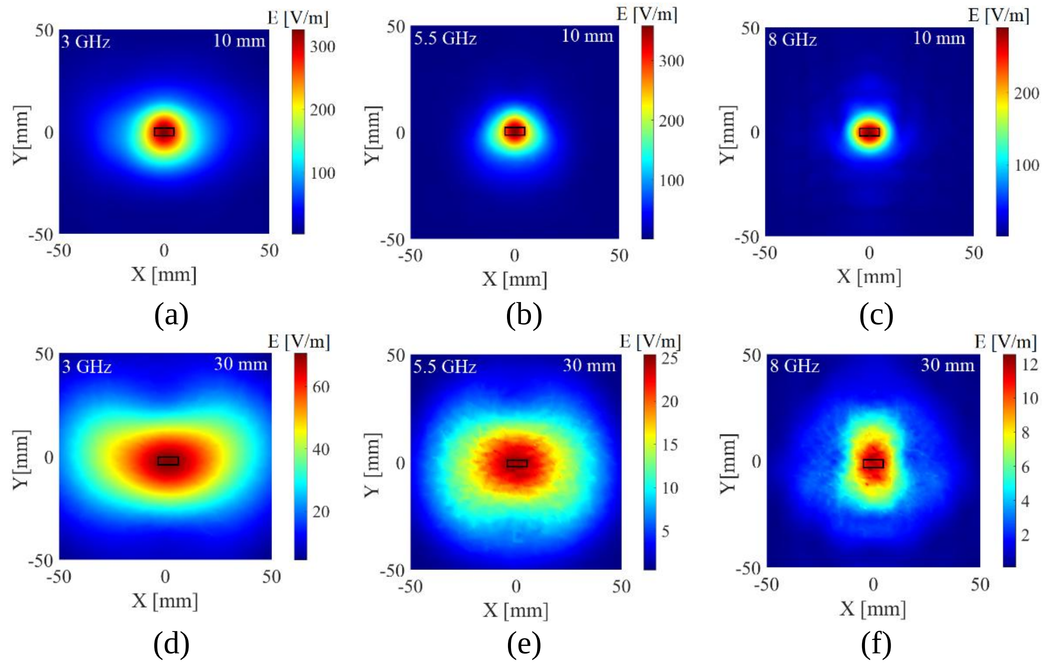

Figure 2-7: Near-field magnitude distributions obtained through simulations where the antenna element operates in a transmitting mode. The field plots show the distribution at frequencies 3 GHz (a and b), 5.5 GHz (c and d), and 8 GHz (e and f) at 10 mm and 30 mm from the antenna-tissue interface. The black rectangle indicates the position of the radiating slot.

tissue; therefore, the far-field patterns are not relevant. The envisioned thickness in compressed-breast measurements does not exceed 6 cm. Figure 2-7 presents examples of the *E*-field magnitude distribution due to one excited element (Port 1in Figure 2-4) at 3 GHz, 5.5 GHz, and 8 GHz at distances from the antenna-tissue interface of 10 mm and 30 mm. Smooth field distributions are observed, which is desirable in imaging applications. The polarization of the antenna is predominantly linear and along the *y*-direction.

2.2.5 Efficiency

The efficiency of the antenna elements is investigated via simulation. To this end, a rectangular aperture of size 21×15.5 mm^2 is defined at the slot plane (metal layer 4) of the element at Port 1 (see Figure 2-4). The size of the aperture is selected so that Poynting's vector z-component value at the edges of the rectangular aperture is less than 1/150 of the maximum value. The radiation efficiency is calculated as $e_{\text{rad}} = P_{\text{rad}} / P_{\text{in}}$, where P_{rad} is the radiated power through the defined rectangular aperture and Pin is the power fed to the antenna. The antenna input power P_{in} is computed at each frequency as $P_{\text{in}} = \left(1 - |S_{11}|^2\right) P_1$, where P_1 is the excitation power at Port 1. The radiated power P_{rad} is computed by integrating the real part of the Poynting vector's z-component (exported from the HFSS simulation) over the rectangular aperture covering the slot. The computed total radiation efficiency is shown in Figure 2-8, along with the radiation efficiency that accounts only for the conductor (copper) loss. The latter result is obtained by antenna element shows about 87% efficiency when averaged over the frequency range. It is evident that the antenna loss is due to both conductor and substrate losses of comparable impact.

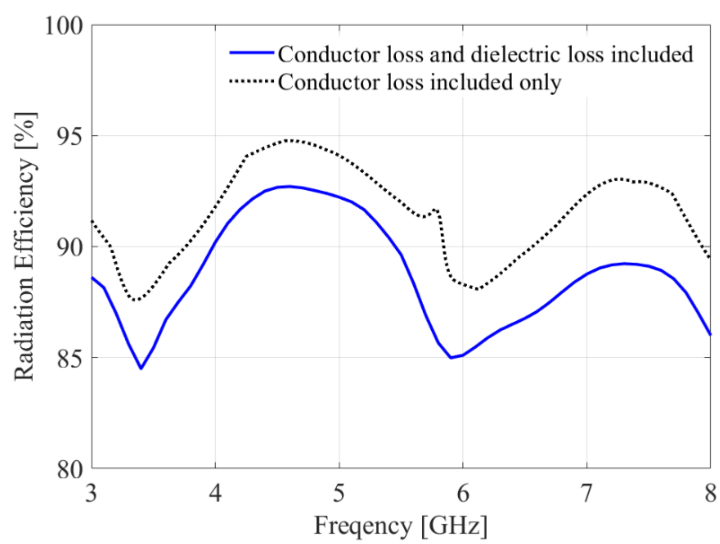

Figure 2-8: Radiation efficiency of an element in the antenna array computed using the simulated S_{11} parameter and Poynting vector distribution.

2.3 Active Sensing Array

2.3.1 Antenna Layout and Geometry

The active sensing array integrates the passive array with LNA chips. It is designed and simulated using Keysight Advanced Design System (ADS) [44]. The LNA is integrated into the electronics layer as shown in Figure 2-9. The circuit includes the LNA chip (Mini-Circuits PMA3-83LN+) and the discrete components of a bias tee, namely, the chip capacitors C1, C2, C3, and the chip inductors L1 and L2. The values of the discrete components are those suggested by the LNA chip manufacturer [44]. The DC biasing of the LNA is provided through the VDD pad and the ground pads. The signal captured by the slot antenna is fed into the LNA input by the CPW at the electronics layer, as indicated in Figure 2-10. The transition from the CPW to the LNA input has been optimized for a good impedance match. The amplified signal is fed to the SMPS connector through another finite-ground CPW with a right-angle bend. All CPW interconnects and component grounding pads are grounded using via-holes. The layout of the LNA circuitry with the SMPS

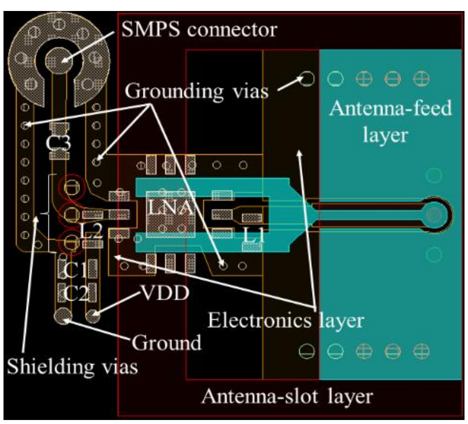

Figure 2-9: The layout of the active antenna element simulated in ADS, showing three metal layers (shield layer not shown): antenna-slot layer in red, antenna-feed layer in blue, and electronics layer in yellow. Areas shaded in beige indicate the soldering pads for the discrete components (C1, C2, C3, L1, and L2), the SMPS connector, and the LNA chip.

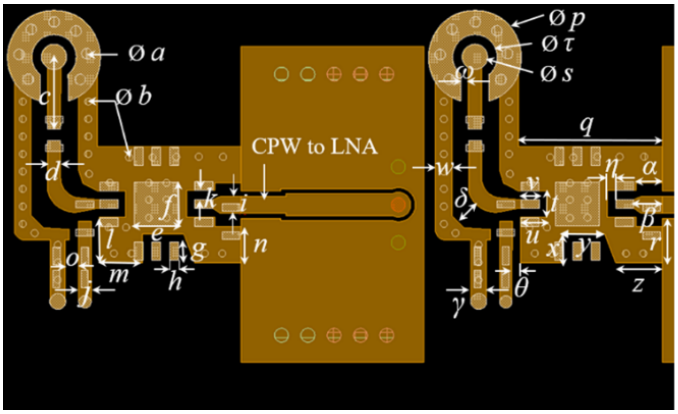

Figure 2-10: Layout and dimensioning of the simulated LNA layout with the SMPS connector. Only the electronics layer of the PCB is shown.

Table 2-1: Dimension of the LNA layout

Symbol	Size (mm)	Symbol	Size (mm)
a	0.300	*r*	1.265
b	0.200	*s*	0.721
c	2.055	*t*	0.753
d	0.380	*u*	0.753
e	1.250	*v*	0.511
f	1.250	*w*	0.470
g	0.516	*x*	0.812
h	0.250	*y*	1.173
i	0.480	*z*	1.323
j	0.361	α	0.740
k	0.245	β	0.809
l	1.289	γ	0.439
m	1.233	δ	0.713
n	1.026	ω	0.212
o	0.379	θ	0.229
p	2.680	τ	1.275
q	4.091	η	0.237

connector pad is provided in Figure 2-10, along with the dimensions in Table 2-1

2.3.2 Active Sensing Array Performance

A simulation based on HFSS with co-simulation in ADS is performed as follows. Two passive arrays (see Section 2.2) are utilized as Tx and Rx arrays in a transmit-receive configuration in HFSS, where the arrays are placed 33 mm apart along the *z*-axis; see Figure 2-11a. Between the Tx and Rx arrays, a cylindrical tissue-mimicking medium is placed with a diameter of 21 cm and relative permittivity of $\varepsilon_r \approx 9.6 - i3.8$. This medium matches the one in the measurement setup. One element of the Tx array is excited, and its corresponding (boresight-aligned) element on the Rx array collects the signal. The simulation employs a discrete frequency sweep from 3 GHz to 8 GHz with a step of 100 MHz.

The simulated transmission coefficient S_{21} of this passive configuration, along with the *S*-parameters of the LNA, provided by the manufacturer, are imported into two S2P blocks in the ADS schematic as shown in Figure 2-11b. The S2P blocks are terminated with 50-ohm ports. The co-simulation is performed from 3 GHz to 8 GHz to obtain the overall system transmission coefficient S_{21}.

To verify the performance of the active sensing array through measurement, another array prototype has been fabricated. It is composed of 6×6 elements wherein 3 elements are integrated with LNAs, the outputs of which are accessed through SMPS connectors. The remaining elements are passive, and four of them are equipped with SMPS connectors in order to measure their output signals and compare them with those of the active elements (see Figure 2-12a). Port 1 of the

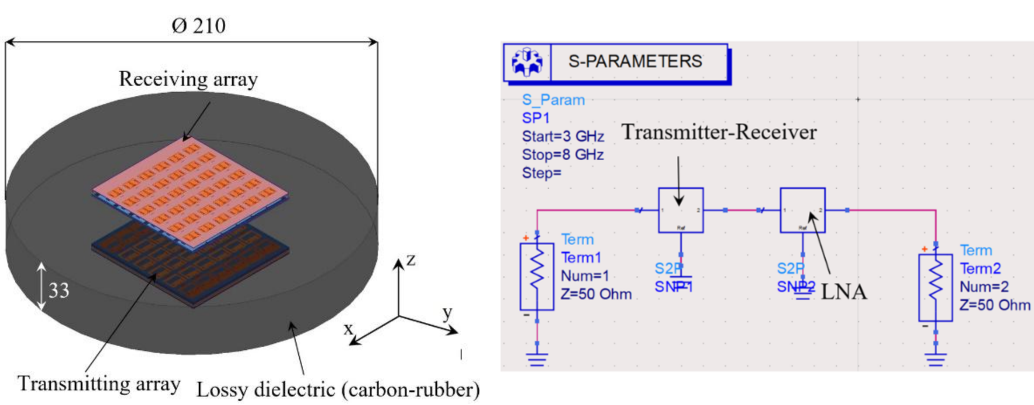

(a) (b)

Figure 2-11: (a) Isometric view of transmit-receive configuration in HFSS with dimensions in mm. (b) *Co-simulation* schematic in ADS.

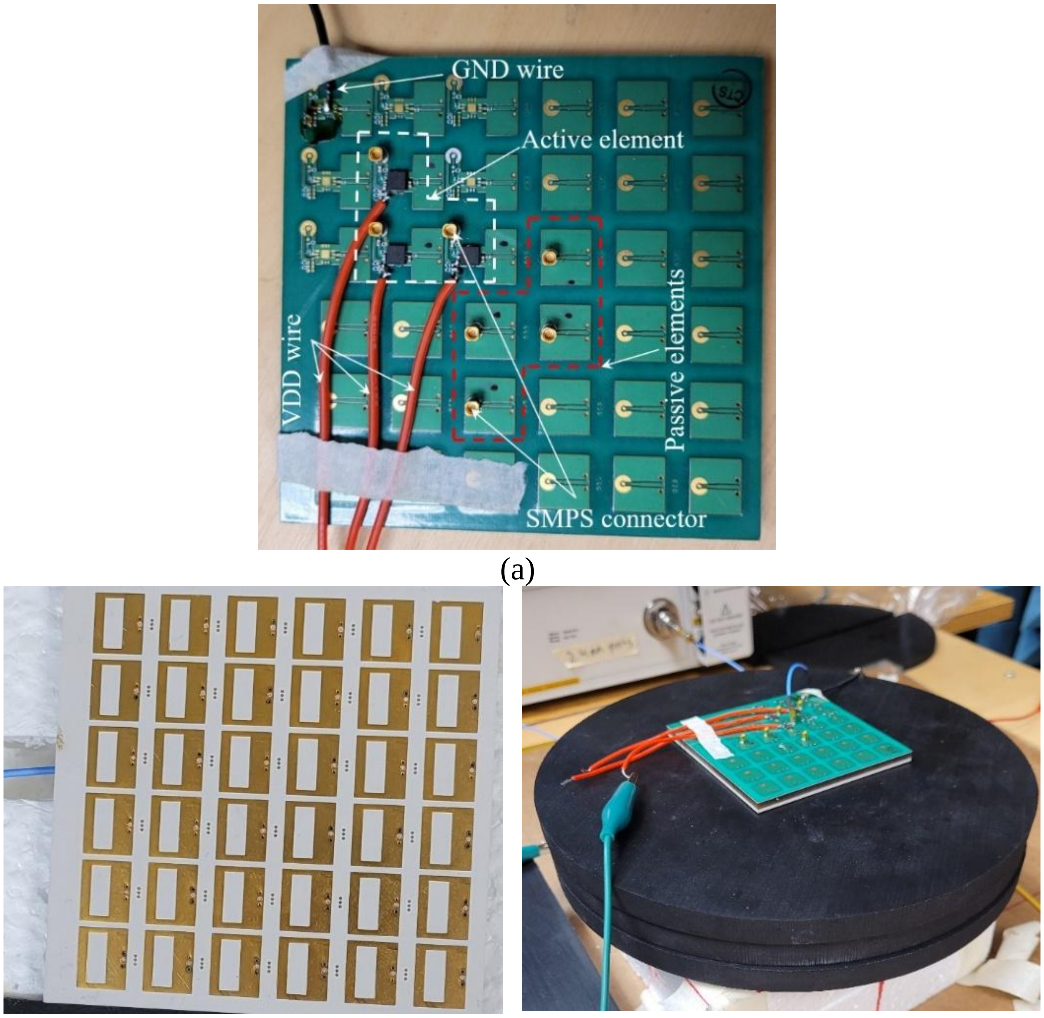

(a)

(b) (c)

Figure 2-12: (a) Electronics layer of the fabricated 6×6 Rx array with the SMPS connectors and LNA chips at the active elements. (b) The slot layer of the Tx passive array. (c) The measurement setup of the transmit-receive configuration, where the Tx and Rx arrays are separated by three 11 mm-thick circular carbon-rubber slabs emulating breast tissue.

VNA is connected to Port 1 of the Tx array (see Figure 2-5a). The phantom is a stack of three 11 mm-thick custom-made carbon-rubber slabs (Figure 2-12c) whose relative complex permittivity, averaged over the frequencies from 3 GHz to 8 GHz, is approximately $\varepsilon_r \approx 9.6 - i3.8$ (as in the simulation setup). Port 2 of the VNA is first connected to one of the passive elements on the active sensing array, and then it is connected to one of the active elements. In each case, the Tx and Rx arrays are

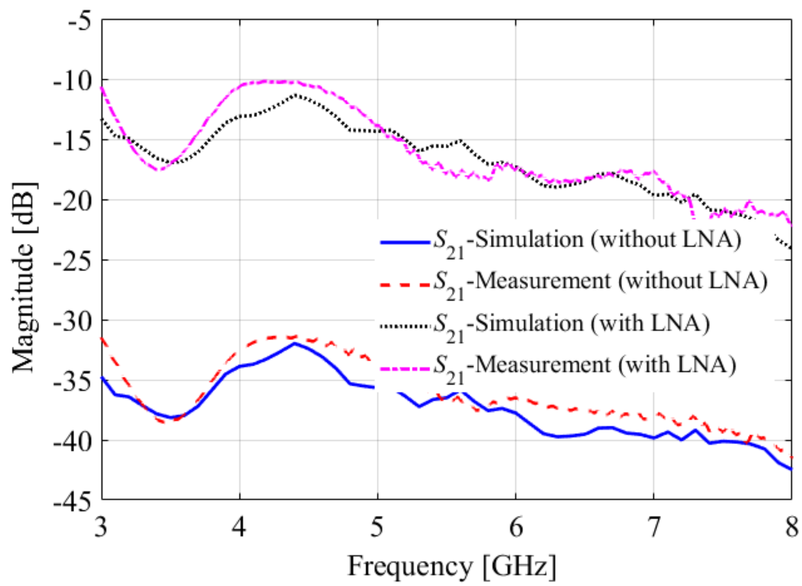

Figure 2-13: Simulated and measured S_{21} in dB of the passive sensing element and active sensing element. An expected gain of approximately 20 dB is observed in both simulation and measurement.

aligned so that the Rx element is along the boresight of the Tx element. The DC biasing of the LNA is provided through the red and black wires observed in Figure 2-12a.

The measured S_{21} responses (in dB) with the active and passive Rx elements are shown in Figure 2-13, along with the simulated responses. There is a good agreement between simulation and measurement. A gain of 20 dB in the frequency band from 3 GHz to 8 GHz is also observed, which corresponds to the gain of the LNA.

2.4 Validation in Imaging Experiment

A near-field imaging experiment with a compressed-breast tissue phantom is carried out to evaluate the functionality of the proposed UWB active sensing array. A step-frequency continuous wave (SFCW) signal is provided through port 1 of an Advantest R3770 4-port VNA to a dielectric-filled transverse electromagnetic (TEM) horn Tx antenna [46]. The horn is designed to operate in direct contact with breast tissue. Two active elements and one passive element of the sensing array are paired with the remaining ports of the VNA. The data acquisition is performed in a scanning chamber (see Figure 2-14). The Tx antenna and the sensing array are fixed at each other's boresight while a translation stage moves the Plexiglas tray, on which the compressed breast phantom is placed, along the x and y directions. The bottom of the Plexiglas tray is 4.5 mm thick. The Tx horn aperture and the Rx array are positioned as close as possible (about 1 mm) from the respective phantom surfaces. The TEM horn scans above the top phantom face, whereas the Rx array scans at the bottom of the Plexiglas tray that holds the tissue phantom. An area of 180 mm ×180 mm area is scanned with a spatial sampling step of 3 mm, employing a frequency sweep between 3 GHz and 8 GHz with 100 MHz increments. The area is chosen to match the area scanned by the envisioned final electronically scanned Rx array, consisting of 18×18 active elements. The 3 mm sampling step corresponds to about a quarter of a wavelength

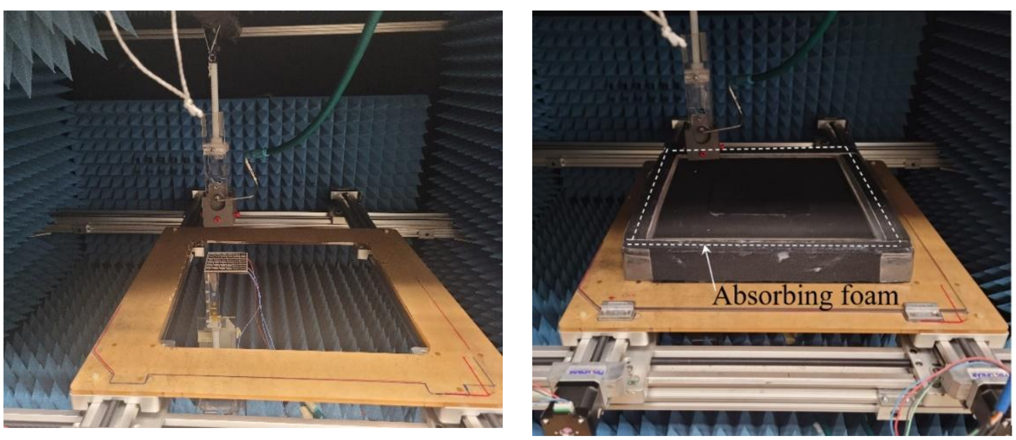

(a) (b)

Figure 2-14: (a) Photo of the Plexiglas tray inside the scanning chamber with the TEM horn as a Tx antenna on top and the proposed Rx array at the bottom. (b) Photo of the breast-tissue phantom surrounded by a black-foam microwave absorber inside the Plexiglas tray.

in the tissue phantom at the highest frequency of 8 GHz. Half-wavelength sampling is more than sufficient in transmission measurements [47]. However, the used image-reconstruction algorithm provides an image pixel size equal to the sampling step. Thus, the chosen sampling step ensures a pixel size of 3×3 mm, which is fine enough to allow for examining the image spatial resolution as dependent on the chosen frequency band rather than the sampling step.

It is worth noting that the presence of the 1 mm air gap and the 4.5 mm Plexiglas bottom layer between the Rx slot array and the tissue phantom degrades the antenna insertion loss, which averages at about −5 dB over the frequency band. Nonetheless, the received signal is sufficiently strong to allow for successful image reconstruction. We emphasize that the large electronically scanned Rx array is to operate in direct contact with the tissue without the need to scan mechanically.

A compressed breast phantom is prepared using three stacked 11 mm thick carbon-rubber slabs, mimicking scattered fibro-glandular breast tissue (BI-RADS Type 2), and two 2 mm thick carbon-silicone sheets, mimicking skin tissue [48] (see Figure 2-15a). The 2 mm sheets are placed on the top and the bottom of the phantom. The 11-mm slabs and the 2-mm sheets are cut to resemble the shape of a compressed breast. The lateral dimensions of the phantom are indicated in Figure 2-15b. In the second (middle) carbon-rubber slab, a circular section with a diameter of 94 mm is cut out to insert various tissue simulants, while the other two slabs are left intact. An irregularly shaped material mimicking healthy fibro-glandular tissue is placed inside the circular section; see the beige area outlined by a red dash line in Figure 2-15c. It is surrounded by a matching medium whose permittivity is closer to that of the carbon-rubber slabs. One tumor simulant of diameter 15 mm is

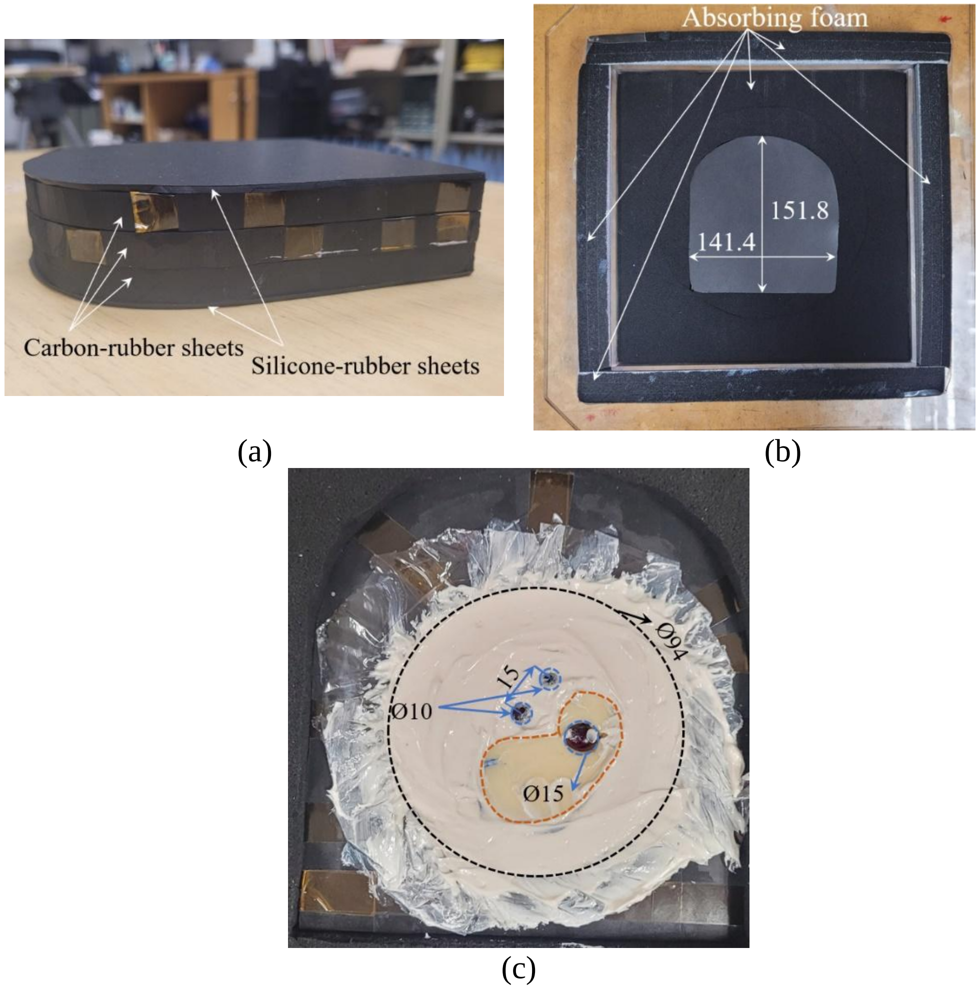

Figure 2-15: (a) Photo of the assembled compressed breast phantom. (b) The breast phantom inside the tray surrounded by a black foam microwave absorber (dimensions in mm). (c) Middle slab of the phantom with a circular cut (black dash-line circle) filled with matching medium (white color), fibro-glandular tissue simulant (brown dash line contour), and three tumor simulants (blue dash-line contours).

inserted within the fibro-glandular object, and two more tumor simulants (of diameter 10 mm) are embedded in the matching medium. The complex relative permittivity values of the matching medium, the tumor simulants and the fibro-glandular simulant are measured from 3 GHz to 8 GHz using a slim form probe [49]. These measured permittivity values are averaged over the frequency and listed in Table 2-2. The prepared middle slab is wrapped in plastic wrap to secure all inclusions. The assembled phantom is placed inside the Plexiglas tray and is surrounded by black foam microwave absorbers [50] as shown in Figure 2-15b. The foam microwave absorbers feature attenuation of 11 dBm/cm and 24 dBm/cm at 3 GHz and 10 GHz, respectively. They are critical in reducing the reflections at the side walls of the phantom and thus decreasing the image artifacts. Absorbing foam is also used to line the side walls of the Plexiglas tray to further suppress reflections; see Figure 2-14b. The S_{21} data sets collected by the active and passive Rx array elements are processed using the real-time quantitative image-reconstruction algorithm referred to as Fourier-space scattered power mapping (F-SPM) [51]. Since only forward-scattering (transmission) data are available in the planar scan, range resolution (along z) is not available [47]. Thus, the reconstructed images are only two-dimensional (2D), depicting the lateral distribution (along x and y) of the real and imaginary relative permittivity of the object. The permittivity values are effectively averaged over z and over frequency. The 2D quantitative images of the heterogeneous breast phantom are shown in Figure 2-16. The tumor simulants are detected well, along with the healthy fibro-glandular tissue inclusion. Their averaged permittivity values correlate well with those listed in Table 2-2. The resolution is better than 15 mm (the center-to-center distance between the two small tumor simulants).

Table 2-2: Averaged dielectric properties of phantom materials over the frequencies from 3 GHz to 8 GHz

Material	ε_r'	ε_r''
Carbon-rubber Slab	9.60	3.82
Carbon-silicone Sheet [47]	19.36	14.00
Matching Medium	11.30	2.59
Tumor Simulant	64.11	22.32
Fibro-glandular Tissue Simulant	17.61	7.89
Scattering Probe	43.70	≈ 0

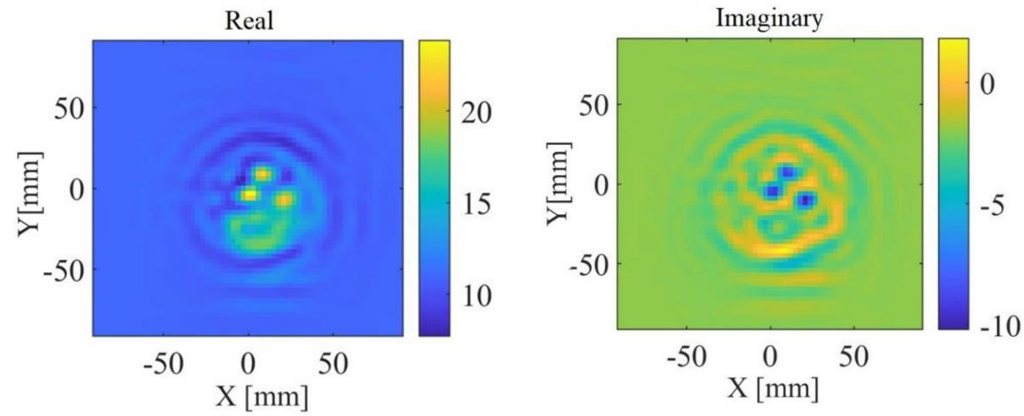

(a) (b)

Figure 2-16: 2D reconstructions of the real and imaginary parts of the relative permittivity of the compressed breast phantom using the F-SPM algorithm.

We note that the image reconstruction is not affected significantly when using only the two active element responses as compared to using both the active and passive elements. The passive-element responses, however, exhibit increasingly poor signal-to-noise ratio at higher frequencies.

2.5 Conclusion

An ultra-wideband (3 GHz to 8 GHz) planar active sensing array for microwave imaging of the breast has been proposed. It consists of slot antennas, fully shielded from the back, where each element is equipped with an LNA. The array features element reflection loss better than 10 dB and inter-element mutual coupling better than −20 dB. The critical design component, allowing for practical implementation in large arrays on a multi-layer PCB, is the triple-wire vertical transition that carries the signal from the antenna-feed layer, through the grounded shield, to the top electronics layer, where the LNAs reside. The performance of the array elements is investigated in terms of near-field distribution and efficiency. They provide unidirectional radiation (no back radiation) and smooth field distribution inside the tissue. The average radiation efficiency is 87% over the frequency band. Both passive and active sensing array prototypes comprising 6×6 elements have been fabricated for validation through measurements. The expected gain of 20 dB in the received signal strength due to the employed LNAs is confirmed. The active sensing array has also been successfully tested in a near-field imaging experiment with a heterogeneous compressed-breast phantom.

Future work will focus on the fabrication of the final 18×18 active antenna array, which connects to a matching array of 18×18 mixer chips whose outputs are multiplexed through an IF-switching network. The envisioned measurement architecture [52] employs a 2-port VNA in a frequency-conversion measurement mode, i.e., the VNA measures the magnitude and phase of the down-converted single-tone IF signal. Since the VNA offers only one port for the IF signal, an IF switching network is needed to multiplex the 324 (18×18) IF channels. The envisioned receiving array will allow for fast electronic scanning over an area of about 20 cm × 20 cm. Moreover, in comparison with the RF-switched receiving arrays, the IF-switched architecture will offer a significantly improved signal-to-noise ratio due to reduced loss and better channel decoupling.

2.6 References

[1] K.C. Oeffinger, E.T. Fontham, R. Etzioni, A. Herzig, J. S. Michaelson, Y. C. Shih, L.C. Walter, T. R. Church, C. R. Flowers, S. J. LaMonte, and A. M. Wolf, "Breast cancer screening for women at average risk: 2015 guideline update from the American Cancer Society," *J. Amer. Med. Assoc.*, vol. 314, no. 15, pp 1599–1614, Oct. 2015.

[2] N. Dimitrova, P. Z. Saz, A. Bramesfeld, T. A. Uluturk, G. Bocchi, L. Pylkkanen, A. J. Lopez, L. Neamtiu, M. Ambrosio, S. Deandrea, and D. Lerda, "European guidelines for breast cancer screening and diagnosis – the European breast guidelines," *Joint Res. Centre (JRC) Technical Reports*, 2016.

[3] M. T. Mandelson, N. Oestreicher, P. L. Porter, D. White, C. A. Finder, S. H. Taplin, and E. White, "Breast density as a predictor of mammographic detection: Comparison of interval- and screen-detected cancers," *J. Nat. Cancer Inst.*, vol. 92, no. 13, pp. 1081–1087, Jul. 2000.

[4] M. von Euler-Chelpin., M. Lillholm, I. Vejborg, M. Nielsen and E. Lynge, "Sensitivity of screening mammography by density and texture: a cohort study from a population-based screening program in Denmark," *Breast Cancer Research*, vol. 21, p. 111, Dec. 2019.

[5] M. A. Helvie, H.-P. Chan, D. D. Adler, and P. G. Boyd, "Breast thickness in routine mammograms: effect on image quality and radiation dose," *Amer. J. Roentgenol*, vol. 163, no. 6, pp. 1371–1374, Dec. 1994.

[6] H. G. Welch, P. C. Prorok, A. J. O'Malley, and B. S. Kramer, "Breast-cancer tumor size, overdiagnosis, and mammography screening effectiveness," *The New England J. Med.*, vol. 375, no. 15, pp. 1438–1447, Oct. 2016.

[7] C. Nickson and A. M. Kavanagh, "Tumour size at detection according to different measures of mammographic breast density," *J. Med. Screening*, vol. 16, no. 3, pp. 140–146, Jul. 2009.

[8] *Breast Cancer*. Public Health Agency of Canada. Accessed: May 10, 2022. [Online]. Available: https://www.canada.ca/en/public-health.html

[9] N. Houssami, L. Irwig, J. M. Simpson, M. McKessar, S. Blome, and J. S. Noakes, "Sydney breast imaging accuracy study: Comparative sensitivity and specificity of mammography and sonography in young women with symptoms," *Amer. J. Roentgenol.*, vol. 180, no. 4, pp. 935–940, Apr. 2003.

[10] D. Thigpen, A. Kappler, and R. Brem, "The role of ultrasound in screening dense breasts—a review of the literature and practical solutions for implementation," *Diagnostics*, vol. 8, no. 1, p. 20, Apr. 2018.

[11] A. Raikhlin, B. Curpen, E. Warner, C. Betel, B. Wright, and R. Jong, "Breast MRI as an adjunct to mammography for breast cancer screening in high-risk patients: retrospective review," *Amer. J. Roentgenol*, vol. 204, no. 4, pp. 889–897, Apr. 2015.

[12] A. Fatemi-Ardekani, C. Boylan and M. D. Noseworthy, "Identification of breast calcification using magnetic resonance imaging," *Med. Physics,* vol. 36, no. 12, pp. 5492–5436, Dec. 2009.

[13] S. P. Poplack, T.D. Tosteson, W.A. Wells, B.W. Pogue, P.M. Meaney, A. Hartov, C.A. Kogel, S. K. Soho, J. J. Gibson, and K. D. Paulsen,

"Electromagnetic breast imaging: results of a pilot study in women with abnormal mammograms," *Radiology*, vol. 243, no. 2, pp. 350–359, May 2007.

[14] T. M. Grzegorczyk, P. M. Meaney, P. A. Kaufman, R. M. diFlorio-Alexander and K. D. Paulsen, "Fast 3-D tomographic microwave imaging for breast cancer detection," *IEEE Trans. Med. Imaging*, vol. 31, no. 8, pp. 1584–1592, Aug. 2012.

[15] A. W. Preece, I. Craddock, M. Shere, L. Jones, and H. L. Winton, "MARIA M4: clinical evaluation of a prototype ultrwideband radar scanner for breast cancer detection," *J. Med. Imag.*, vol. 3, no. 3, article 033502, Jul. 2016.

[16] E. Porter, H. Bahrami, A. Santorelli, B. Gosselin, L.A. Rusch, and M. Popović, "A wearable microwave antenna array for time-domain breast tumor screening," *IEEE Trans. Med. Imaging*, vol. 35, no. 6, pp. 1501-1509, Jan. 2016.

[17] H. Song, S. Sasada, T. Kadoya, M. Okada, K. Arihiro, X. Xiao, and T. Kikkawa, "Detectability of breast tumor by a hand-held impulse-radar detector: performance evaluation and pilot clinical study," *Sci. Rep.*, vol. 7, p. 16353, Nov. 2017.

[18] D. Tajik, F. Foroutan, D.S. Shumakov, A.D. Pitcher, and N.K. Nikolova, "Real-time microwave imaging of a compressed breast phantom with planar scanning," *IEEE J. Electromagn., RF Microw. Med. Biol.*, vol. 2, no. 3, pp. 154–162, Sep. 2018.

[19] N.K. Nikolova, "Microwave imaging for breast cancer," *IEEE Microw. Mag.*, vol. 12, no. 7, pp. 78–94, Dec. 2011.

[20] D. O'Loughlin, M. O'Halloran, B.M. Moloney, M. Glavin, E. Jones, and M.A. Elahi, "Microwave breast imaging: Clinical advances and remaining challenges," *IEEE Trans. Biomed. Eng.*, vol. 65, no. 11, pp. 2580-2590, Feb. 2018.

[21] M. T. Islam, M. Z. Mahmud, M. Tarikul Islam, S. Kibria, and M. Samsuzzaman, "A low cost and portable microwave imaging system for breast tumor detection using UWB directional antenna array," *Sci. Rep.*, vol. 9, no. 1, pp. 1–13, Oct. 2019.

[22] J. C. Lin, "Frequency optimization for microwave imaging of biological tissues," *Proc. IEEE*, vol. 73, no. 2, pp. 374–375, Feb. 1985.

[23] S.Y. Semenov, A. E. Bulyshev, A. Abubakar, V. G. Posukh, Y. E. Sizov, A. E. Souvorov, P. M. Van Den Berg, and T.C. Williams, "Microwave-tomographic imaging of the high dielectric-contrast objects using different image-reconstruction approaches," *IEEE Trans. Microw. Theory Techn.*, 53, no. 7, pp. 2284–2294, Jul. 2005.

[24] H.M. El Misilmani, T. Naous, S. K. Al Khatib, and K. Y. Kabalan, "A survey on antenna designs for breast cancer detection using microwave imaging," *IEEE Access*, vol. 8, pp. 102570–102594, Jun. 2020.

[25] M. Klemm, D. Gibbins, J. Leendertz, T. Horseman, A. W. Preece, R. Benjamin, and I. J. Craddock, "Development and testing of a 60-element UWB conformal array for breast cancer imaging," *in Proc. 5th Eur. Conf. Antennas Propag. (EUCAP)*, pp. 3077–3079, Apr. 2011.

[26] T. Sugitani, S. Kubota, A. Toya, and T Kikkawa, “A compact 4 x 4 planar UWB antenna array for 3-D breast cancer detection,” *IEEE Antennas Propag. Soc. Int. Symp.*, vol. 12, pp. 733–736, Jun. 2013.

[27] F. Foroutan and N. K. Nikolova, “Active sensor for microwave tissue imaging with bias-switched arrays,” *Sensors*, vol. 18, E1447, May 2018.

[28] F. Foroutan and N. K. Nikolova, “UWB active antenna for microwave tissue imaging,” *IEEE Antennas Wireless Propag. Lett.*, vol. 18, no. 10, pp. 1951–1955, Oct. 2019.

[29] D. Gibbins, M. Klemm, I. J. Craddock, J. A. Leendertz, A. Preece, and R. Benjamin, “A comparison of a wide-slot and a stacked patch antenna for the purpose of breast cancer detection,” *IEEE Trans. Antennas Propag.*, vol. 58, no. 3, pp. 665–674, Dec. 2009.

[30] C. Song, Y. Huang, J. Zhou, J. Zhang, S. Yuan, and P. Carter, “A high-efficiency broadband rectenna for ambient wireless energy harvesting,” *IEEE Trans. Antennas Propagt.*, vol. 63, no. 8, pp. 3486–3495, May 2015.

[31] P. Lu, Ch. Song, and K. M. Huang, “Ultra-wideband rectenna using complementary resonant structure for microwave power transmission and energy harvesting,” *IEEE Trans. Microw Theory Tech*., vol. 69, no.7, pp. 3452–3462, Mar. 2021.

[32] N. Valizade Shahmirzadi, and H. Oraizi, “Design of reconfigurable coplanar waveguide-fed planar antenna for multiband multi-input–multi-output applications,” *IET Microw. Antennas Propag.*, vol. 10, no. 14, pp. 1591–1597, Nov. 2016.

[33] N. Hasegawa, and N. Shinohara, “C-band active-antenna design for effective integration with a GaN amplifier,” *IEEE Trans. Microw Theory Tech.*, vol. 65, no. 12 pp. 4976–4983, Jul. 2017.

[34] T. H. Jang, K. K. Hwang, G. H. Park, H. Y. Kim, H. H. Bae, C. W. Byeon, and C. S. Park, “A 60 GHz wideband, low-power active receiving antenna with adjustable polarization for SNR improvement,” *IEEE Trans. Antennas Propagt.*, vol. 67, no. 12, pp. 7296–7303, Aug. 2019

[35] H. Al-Saedi, W. M. Abdel-Wahab, S. M. Raeis-Zadeh, E. H. M. Alian, A. Palizban, A. Ehsandar, N. Ghafarian, G. Chen, S. R. Boroujeni, M. R. Nezhad-Ahmadi, and S. Safavi-Naeini, “An integrated circularly polarized transmitter active phased-array antenna for emerging ka-band satellite mobile terminals,” *IEEE Trans. Antennas Propagt.*, vol. 67, no. 8, pp. 5344–5352, Aug. 2019.

[36] A. F. Mirza, C. H. See, I. M. Danjuma, R. Asif, R. A. Abd-Alhameed, J. M. Noras, R. W. Clarke, and P.S. Excell, “An active microwave sensor for near field imaging,” *IEEE Sens. J.* vol. 17, no. 9, pp. 2749–2757, Feb. 2017.

[37] C. A. Balanis, *Antenna Theory: Analysis and Design*. Hoboken, NJ, USA: Wiley, 2015.

[38] Ansys Corporation. *HFSS 2020 R2*. Accessed: May 10, 2022. [Online]. Available: https://www.ansys.com/

[39] Jia-Yi Sze and Kin-Lu Wong, “Bandwidth enhancement of a microstrip-line-fed printed wide-slot antenna,” *IEEE Trans. Antennas Propag.*, vol. 49, no. 7, pp. 1020–1024, July 2001.

[40] L. Sun, Y. Li and Z. Zhang, "Wideband decoupling of integrated slot antenna pairs for 5G smartphones," *IEEE Trans. Antennas Propag.*, vol. 69, no. 4, pp. 2386–2391, Sep. 2020.

[41] Y. Q. Hei, J.G He, and W. T. Li, "Wideband decoupled 8-element MIMO antenna for 5G mobile terminal applications," *IEEE Antennas Wireless Propag. Lett.*, vol. 20, no. 8, pp. 1448–1452, Jun. 2021.

[42] J. Melnikow, J. J. Fenon, and E. P. Whitlock, "Supplemental screening for breast cancer in women with dense breasts: A systematic review for the U.S. Preventive services task force," *Ann. Internal Med.*, vol. 164, no. 4, pp. 268–278, Feb. 2016.

[43] *ACR BI-RADS ATLAS-MAMMOGRAPHY*. Accessed: Nov. 13, 2021. [Online]. Available: https://www.acr.org/-/media/ACR/Files/RADS/BI-RADS/Mammography-Reporting.pdf

[44] Keysight-Technologies. *Pathwave Advanced Design System (ADS).* Accessed: May 10, 2022. [Online]. Available: https://www.keysight.com/ca/en/products/software/pathwavedesignsoftware/pathwave-advanced-design-system.html

[45] Mini-Circuits. *TB-830A+ Evaluation Board*. Accessed: May 10, 2022. [Online]. Available: https://www.minicircuits.com/WebStore/dashboard.html?model=PMA3-83LN%2B

[46] R. Khalaj Amineh, A. Trehan, and N. K. Nikolova, "TEM horn antenna for ultra-wide band microwave breast imaging," *Prog. Electromagn. Res.B*, vol. 13, pp. 59–74, 2009.

[47] N. K. Nikolova, *Introduction to Microwave Imaging*. Cambridge, U.K.: Cambridge Univ. Press, Jul. 2017.

[48] Laird. *Flexible Absorber Silicone Rubber Sheet*. [Online]. Available: https://www.laird.com/sites/default/files/2021-01/RFP-DSJCS%2018062020.pdf.

[49] *Dielectric Probe Kit 200 MHz to 50 GHz, (85070E)*, Keysight Technologies, Santa Rosa, CA, USA, 2014.

[50] Cuming Microwave. *C-RAM MT LOSSY, Carbon Filled, Flexible Foam Sheet Stock*. Accessed: May 10, 2022. [Online]. Available: https://www.ppgaerospace.com/getmedia/c9fa6c24-90d2-459c-9609 b34f7602a6d7/320-2-C-RAMMT

[51] R. Kazemivala, D. Tajik, and N. K. Nikolova, "Simultaneous Use of the Born and Rytov Approximations in Real-Time Imaging with Fourier-Space Scattered Power Mapping," *IEEE Trans. Microw. Theory Techn.*, vol. 70, no. 5, pp. 2904-2920, May 2022.

[52] V. Tyagi, F. Foroutan, N. K. Nikolova, C. H. Chen, and C. Baard, "UWB planar bias-switched imaging array for breast-cancer screening," *in Proc. 15th Eur. Conf. Antennas Propag. (EuCAP),* Düsseldorf, Germany, Mar. 2021, pp. 1–5.

Chapter 3

3. Interconnects for Dense Electronically Scanned Antenna Array Using High-Speed Vertical Connector

Preface

This chapter is a reproduction of the following published article:

N. V. Shahmirzadi, N. K. Nikolova, and C. H. Chen, "Interconnect for dense electronically scanned antenna array using high-speed vertical connector," *Sensors*, vol. 23, no. 20, pp. 8596, Oct. 2023.

Author Contributions: Conceptualization, N. K. Nikolova; methodology, N. V. Shahmirzadi, N. K. Nikolova, and C.-H. Chen; validation, N. V. Shahmirzadi and N. K. Nikolova; investigation, N. V. Shahmirzadi, N. K. Nikolova, and C.-H. Chen; resources, N. K. Nikolova; writing—original draft preparation, N. V. Shahmirzadi; writing—review and editing, N. V. Shahmirzadi, N. K. Nikolova, and C.-H. Chen;

supervision, N. K. Nikolova, and C.-H. Chen; project administration, N. K. Nikolova; funding acquisition, N. K. Nikolova.

3.1 Introduction

Over the past decade, the development of electronically scanned antenna arrays (ESAAs) has been the focus of intense research since they outperform the mechanically scanned systems with exceptional speed, compactness, light weight, and immunity to positioning errors. These advantages make the ESAAs the preferred choice in applications such as wireless communications [1]-[4], radar systems [5], [6], non-destructive testing [7], [8], and microwave imaging [9]-[12], among others. In communications, these arrays enable dynamic beamforming, where the antenna pattern is shaped to maximize the signal power toward the desired receiver(s) and/or to minimize interference from other directions. Radar systems utilize ESAAs for precise beam steering to acquire data from different angles and positions, resulting in improved sensitivity, image quality, and resolution. In non-destructive testing and imaging, ESAAs primarily offer a multiplexing capability among transmit/receive channels, where the inputs/outputs of multiple antenna elements are combined to connect to a single receiver or transmitter.

To realize ESAAs in the microwave frequency range, a widely adopted approach integrates solid-state phase shifters [4], [13], [14], radiofrequency (RF) switches [9], [15], [16], p-i-n and Schottky diodes [17]-[20], varactors [21]-[23], etc., within each antenna element. Such integration adds functionality to the sensing element (e.g., frequency conversion, tunable phase delay), but it does not resolve the problems arising when multiplexing hundreds of such sensors to the transmitting/receiving circuitry as well as the digital control circuitry. In [21], a complementary circuit composed of power dividers and varactors is developed at the rear of the array's printed circuit board (PCB) to provide beam-steering capability at 3 GHz. The topology is narrowband and limited to controlling only 16 elements. Substantial modifications would be necessary to scale up the number of elements to several hundred and to overcome the bandwidth limitations of the power dividers. In a recent study [4], eight solid-state phase shifters are connected to 32 ports of a phased array antenna by utilizing a combination of one 1-to-8 power splitter and eight 1-to-4 power dividers, all interconnected through RF cables. This configuration ensures highly uniform amplitudes and accurate phase shifts. However, the design is bulky. In ESAAs currently employed in microwave tissue imaging [9]-[12], the transmitting/receiving circuitry includes a network of RF switches which are connected through high-quality RF cables and coaxial connectors to the antenna elements. Due to losses in the RF switches and the large size of the co-axial connectors, there are limitations on the number of multiplexed elements and the inter-element spacing. Thus, complementary mechanical scanning is usually required to increase the spatial sampling density [10], [12].

Efficient RF signal routing to/from the mm-sized antenna elements within densely packed arrays is a significant challenge, particularly in the context of imaging, where high-density ESAAs must provide sufficient spatial sampling without the need for mechanical scanning. Conventional RF switching networks are not practical when multiplexing hundreds of array elements. This is due to their substantial insertion loss, limited isolation, and calibration difficulties. To overcome these limitations, a solution based on multiplexing at a single-tone intermediate frequency (IF) has been proposed in [24], [25]. In a recent study on microwave imaging of breast tissue [25], a planar ultra-wideband (UWB) active receiving array has been introduced in the frequency range of 3 GHz to 8 GHz. This array design allows for scalability to a larger configuration of 16×16 elements where an IF switching network enables the multiplexing of hundreds of sensors within the array.

Figure 3-1 shows the architecture of a UWB electronically scanned microwave compressed breast imager employing a scaled-up prototype of the active receiving array first proposed in [25]. The architecture is composed of a 2-port vector network analyzer (VNA), an RF transmitting (Tx) array fed by the VNA through a power distribution network, a local oscillator (LO) power distribution network, a UWB active receiving (Rx) array that captures the scattered signal through an object under test, and an IF-switching network. The employed VNA [27] features an additional internal signal generator, which provides an RF-synchronized LO signal for down-conversion. This allows for vector (magnitude and phase) frequency-conversion measurements. The passive antenna elements in the Tx and Rx arrays are the same. The UWB active Rx array in this development is composed of 16×16 sensors where each antenna element is equipped with its own RF front-end down converting the UWB RF signals to a single tone IF signal. The spacing between the elements is 12 mm in both lateral directions. Due to space constraints and the lack of a single chip UWB platform capable of amplifying and down converting RF signals, each array element is integrated only with a low-noise amplifier (LNA) chip [25]. The mixer arrays, the LO distribution network and the

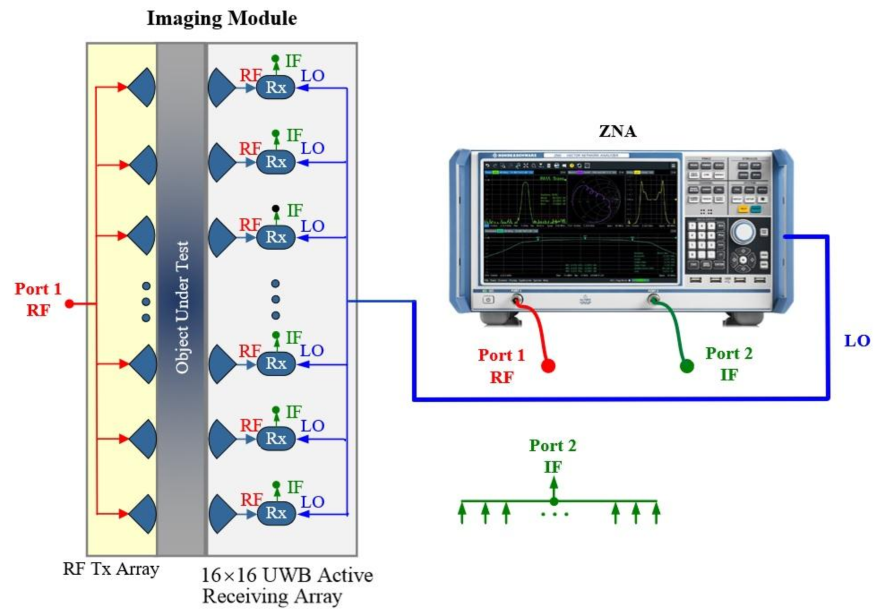

Figure 3-1: The architecture of an electronically scanned system based on the proposed UWB active receiving array prototype in [25] for breast-tissue microwave imaging.

IF-switching network, reside on a separate board, necessitating a low-reflection, low-loss, and low-crosstalk board-to-board transition.

This work presents a solution that achieves seamless transitions from the UWB 16×16 active Rx array PCB to separate PCBs of the corresponding array of mixers and the IF switching network which multiplexes the 256 sensors at the single tone 30 MHz IF output. To this end, we explore the use of high-speed vertical connectors, widely employed in computer technology. These connectors offer several advantages over conventional coaxial connectors, including high pin density, low cost, and mechanical robustness, making them a much preferred choice for board-to-board transitions. The primary focus of this study is to design a high-quality RF transition between the grounded coplanar waveguide (GCPW) lines at the outputs of the LNAs on the Rx antenna board (described in [25]), and a high-speed vertical connector. We assess the performance of this interconnect through electromagnetic (EM) simulations and measurements of fabricated test boards. Subsequently, the high-speed vertical connectors are incorporated into the 16×16 UWB active receiving array, and their performance is investigated and compared with sub-miniature push-on sub-micro (SMPS) coaxial connectors in a 6×6 UWB active Rx array prototype [25]. The SMPS connectors, along with their respective cables and adapters, are expensive. A single SMPS connector costs over US$20, which leads to substantial expenses when arrays consisting of several hundred elements are to be interfaced with electronics. They are mechanically fragile with a limited number of mating cycles, usually ranging from 100 to 500, depending on whether they employ a full detent or smooth bore interface. Importantly, connecting and disconnecting hundreds of such connectors, densely packed on a PCB, is difficult, leading to unreliable electrical performance. Hence, the SMPS connectors are deemed unsuitable for connectorizing large arrays.

To the best of our knowledge, no existing antenna array has yet harnessed the potential benefits of a high-speed connector in the UWB frequency range for board-to-board connections. Therefore, our proposed vertical board-to-board transition holds significant promise not only for our specific application but also for other scenarios that require a transfer of microwave signals between high-density PCBs with hundreds of input/output GCPW interconnects.

In Section 3.2, the design of the GCPW interconnects for high-speed vertical connectors is discussed, followed by validation through measurements. Section 3.3 focuses on the implementation of the designed GCPW interconnects on the 16×16 UWB Rx array board together with the vertical board-to-board connector. The RF performance of the assembly is validated through measurements and compared with that of the SMPS connectors terminating the elements of a prior 6×6 UWB array prototype [25]. Discussion and conclusions are presented in Sections 3.4 and 3.5, respectively.

3.2 Vertical Board-Borad Interconnect Design

In [25], a planar receiving array of UWB active slot antennas has been proposed for microwave imaging of the compressed breast with operating bandwidth from 3 GHz to 8 GHz. Each array element integrates an LNA chip to boost the received signal. This is necessary in tissue imaging because microwave signals suffer significant attenuation, which grows rapidly with frequency [27], [28]. Using the published permittivity and conductivity values for the various healthy breast-tissue properties [27], along with a simple plane wave propagation model, it is possible to estimate the attenuation for a signal path of about 60 mm (the average thickness of a compressed breast during the microwave measurement). Depending on the breast tissue composition in terms of fibro-glandular and adipose content, the estimated attenuation is between −60 dB and −90 dB at the highest frequency of 8 GHz. This translates into attenuation rates from −10 dB/cm to −15 dB/cm. These estimates are confirmed in [25], where a transmission measurement shows an attenuation of about −42 dB at 8 GHz through a 33 mm-thick breast-tissue phantom, which mimics a BI-RADS (Breast Imaging Reporting and Data System) Category B healthy breast tissue (scattered areas of fibro-glandular tissue with 25% to 50% of the overall breast-tissue mass [29]). Thus, signal amplification on receive is imperative, and the active array in [25] employs LNA chips with a flat 20-dB gain throughout the 3 GHz to 8 GHz bandwidth.

The initial 6×6 array prototype reported in [25] demonstrates a seamless integration of the LNA chips with the slot antennas on the Rx array PCB. The design is scalable, which allows for its expansion into larger arrays, such as the 16×16 Rx array shown in Figure 3-2. However, the initial 6×6 array prototype uses SMPS coaxial connectors, which are impractical for large arrays, as discussed earlier. We reiterate that the system architecture in Figure 3-1 requires each Rx array element to connect to a dedicated mixer, requiring 256 identical high-quality RF interconnect paths.

To address this problem, we propose to employ off-the-shelf high-speed board-to-board vertical connectors that offer high pin density, mechanical robustness, and low cost (below US$10 per connector). Figure 3-2 shows the horizontal PCB of the large UWB active Rx array along with the mounted connectors (Samtec MEC2-50-01-L-DV [29]). The connector features 50 pins with a 2-mm pitch on each side. Since the center-to-center spacing between the elements of the Rx array is 12 mm, the connector accommodates 8 elements on each side (16 array elements in total). As shown in Figure 3-2, two connectors, mounted edge-to-edge, can accommodate two 16-element rows (32 array elements in total). Overall, 16 vertical connectors are required for the assembly. The connectors link the Rx array PCB to eight identical vertical PCBs, each accommodating 32 mixer chips, along with an LO distribution network and an IF switching network. Note that the PCB of the Rx antenna array in Figure 3-2 contains unconnected elements at its periphery. These are dummy elements, which ensure identical performance of the connected array elements, all of which are at least one array element away from the PCB edges. In [25], the outputs of the LNAs on the active sensing array employ

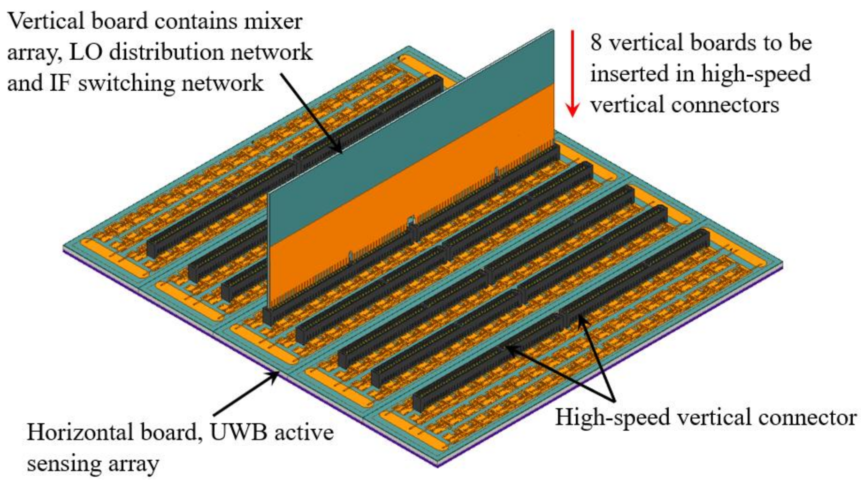

Figure 3-2: Isometric view of a 16×16 UWB active sensing array with 8 rows of vertical connectors, where each row consists of two edge-to-edge MEC2-50-01-L-DV connectors. One of the eight vertical boards (carrying additional electronic circuits) before insertion into the connector is also shown.

short GCPW transmission lines (TLs) terminated with SMPS connectors. As discussed later, these GCPWs need to be thoroughly redesigned in order to achieve acceptable reflection and transmission coefficient when interfacing them with the pins of the vertical board-to-board connector. Specifically, the design goal is to achieve reflection coefficients below −10 dB and "through" transmission coefficients above −1 dB in the frequency band from 3 GHz to 8 GHz.

3.2.1 EM Design of the GCPW Interconnect for the High-speed Vertical Connector

The documentation on MEC2-50-01-L-DV [31] suggests a 50-Ω microstrip layout for the connector's pin footprint. However, in the UWB frequency range, GCPWs are preferred over microstrip lines due to lower dispersion, lower loss, and lower channel crosstalk. Therefore, a new design is necessary for GCPW leads between the circuitry and the connector. To this end, the HFSS [32] encrypted model of MEC2-50-01-L-DV has been acquired from the manufacturer to perform

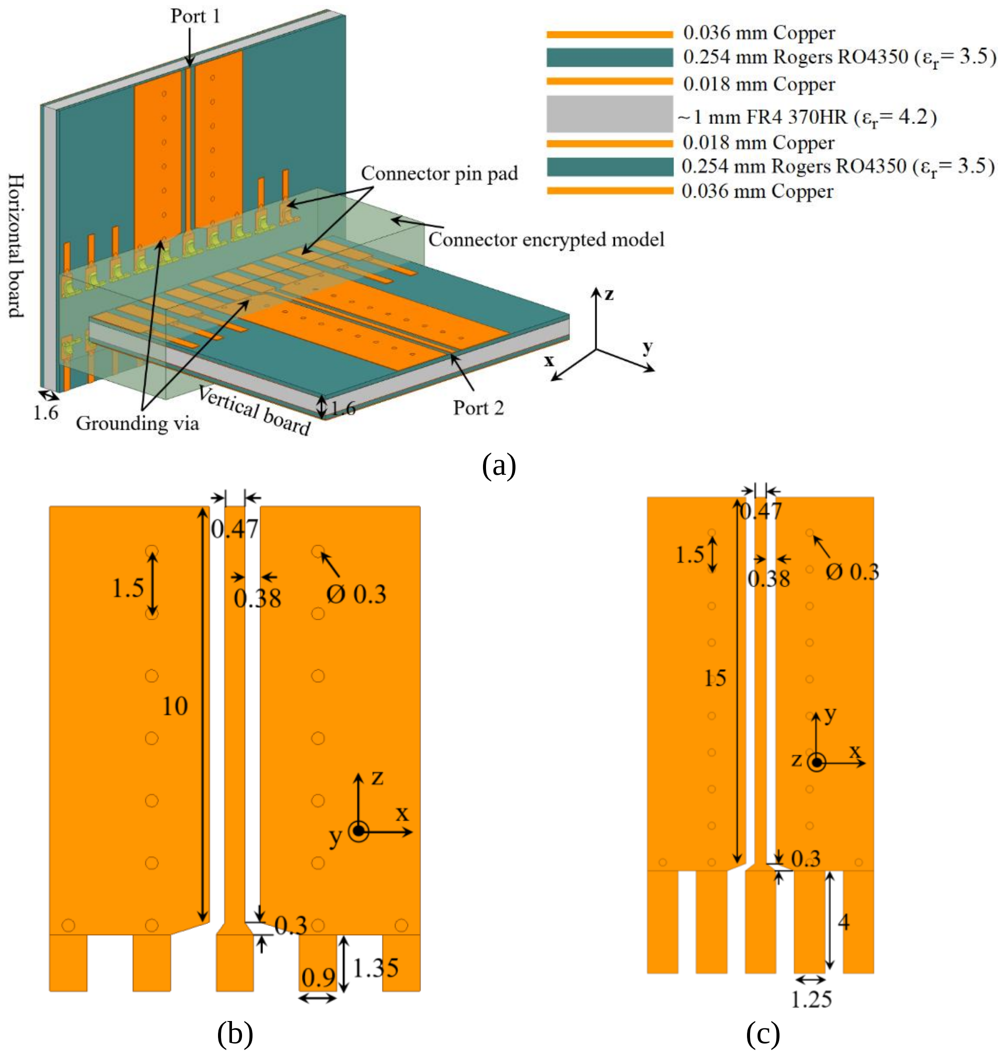

Figure 3-3: (a) Isometric view of the assembly consisting of the GCPW TLs test boards and the encrypted model of the high-speed vertical connector, alongside the stack-up of the test boards. Circles in grey indicate grounding via-holes. For a better view of the pin footprint of the vertical connector, the assembly is tilted at an angle such that the horizontal (Rx antenna array) board appears vertical in the CAD drawing, whereas the vertical (mixer array) board appears horizontal. Layouts of the GCPWs leading to the vertical connector on: (b) the horizontal board (c) the vertical board. All dimensions are in mm.

the design using full-wave EM simulations.

The initial design is based on the assumption that the connector might function effectively with direct connection to 50-Ω GCPW transmission lines. Two test PCBs (horizontal and vertical) are designed to evaluate its performance with such GCPWs over the frequency range from 3 GHz to 8 GHz. Figure 3-3 shows the designed GCPW test boards, along with their respective layout and stack-up. Note that the connector mates to vertical boards of 1.6 mm thickness, which necessitates the FR4 layer as a filler in the middle of the stack-up shown in Figure 3-3a. The signal trace width and the gap width of the GCPW are the same on both the horizontal and vertical boards. The trace width is 0.47 mm, and the gap width is 0.38 mm. Grounding via holes with 1.5 mm center-to-center spacing are employed in the ground planes of GCPWs.

Wave port analysis of the GCPW traces in HFSS yields an approximate 50-Ω characteristic impedance averaged over the 3 GHz to 8 GHz bandwidth. The pin pads' dimensions for both the horizontal and the vertical boards are dictated by the HFSS encrypted model of the connector. The HFSS encrypted model of the connector contains only 20 pins, 5 of which are specifically designated for testing the GCPW interconnect. To prevent ground loops, all the remaining pins on both the vertical and horizontal boards are grounded. The reflection coefficient and transmission coefficient of this configuration are assessed using a 2-port S-parameter analysis, employing wave-port excitation in HFSS with a frequency sweep from 3 GHz to 8 GHz.

The simulation of this initial design indicates that the reflection coefficients at both ports (S_{11} and S_{22}) surpass the –10 dB threshold beyond 4 GHz; see the solid-line results in Figure 3-4a and Figure 3-4b. Accordingly, the transmission coefficients ($S_{21} = S_{12}$) are not satisfactory either, with values as low as –7 dB at high frequencies; see Figure 3-4c. We note that S_{11} and S_{22} are not identical since the vertical connector does not have a mid-point symmetry.

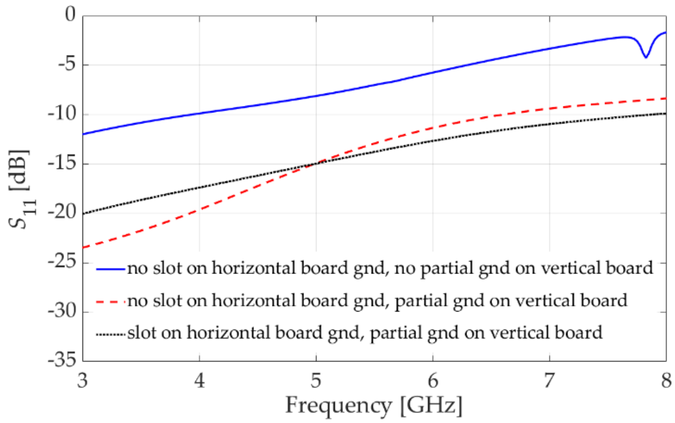

(a)

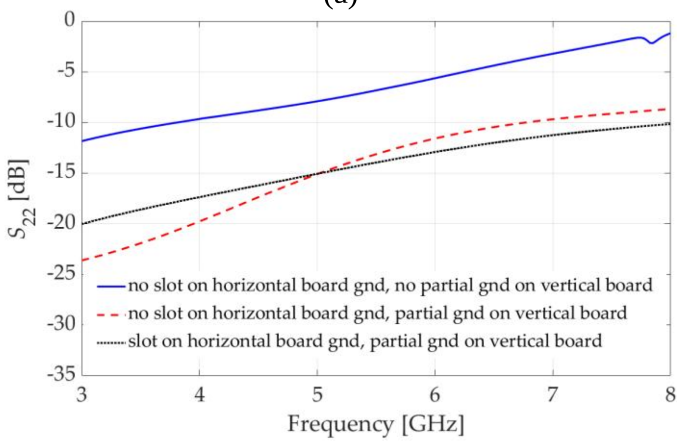

(b)

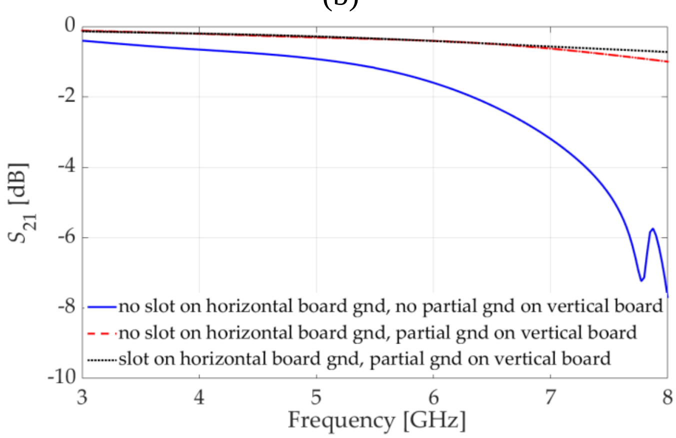

(c)

Figure 3-4: Simulation results for the initial and improved designs of the GCPW layouts on the horizontal and vertical boards in the vertical connector assembly. The improvement is due to two major design changes: (i) introducing partial ground planes on the vertical board and (ii) introducing a slot in the horizontal board ground layer. The initial design results are shown with solid blue lines. The major improvement due to design change (i) is shown by the dash-dot red line. The additional improvement due to design change (ii) is shown by the dotted black line. (a) Reflection coefficient at Port 1 (S_{11}). (b) Reflection coefficient at Port 2 (S_{22}). (c) Transmission coefficient (S_{21}).

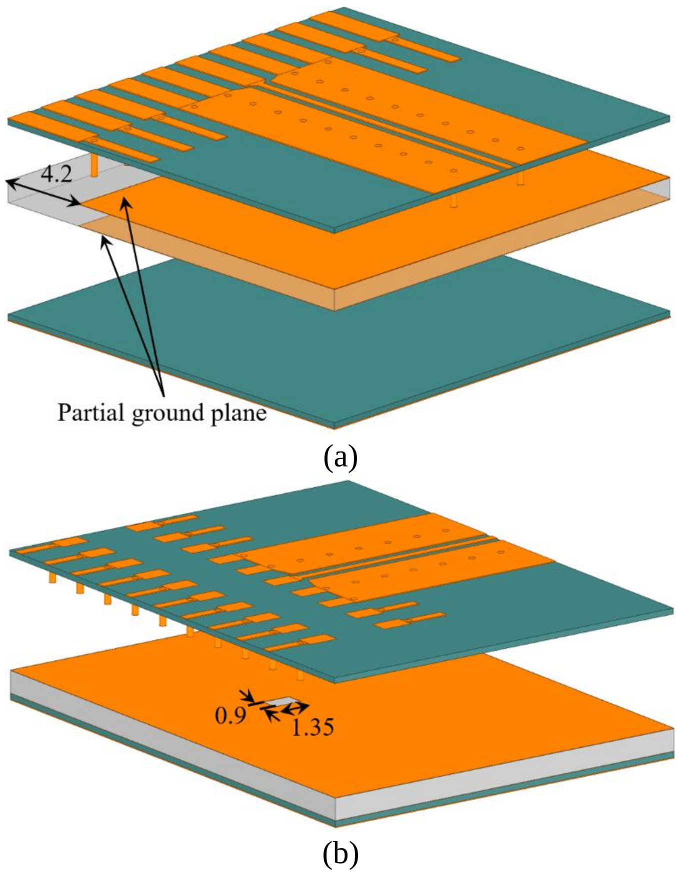

Figure 3-5: Design improvements at the contact points between the GCPWs and the vertical connector: (a) partial ground planes on the vertical board, where metallization is partially removed from the sections to be inserted into the connector; (b) the slot in the ground plane of the horizontal board. Circles in grey and cylinders indicate grounding via-holes.

Since the HFSS model of the connector is encrypted, its internal composition is inaccessible, preventing the analysis of the causes for the unsatisfactory impedance match performance. However, the input resistance and reactance can be inspected at each port of the configuration in Figure 3-3a. At higher frequencies, especially above 5 GHz, the input impedances at both ports exhibit parasitic reactances. To bring the reflection coefficients below the desired –10 dB level throughout the UWB frequency spectrum, two significant design changes are made. First, partial ground planes on both sides of the vertical board are introduced (see Figure 3-5a) such that the metallization is partially removed from the sections which are inserted into the connector. Second, a slot beneath the connector's pin pad at the signal trace of the GCPW on the horizontal board is introduced, as shown in Figure 3-5b. Each one of these measures counteracts the parasitic effects at higher frequencies, as is asserted by the reflection and transmission coefficient plots in Figure 3-4. The improved design features good impedance match (reflection loss better than 10 dB) in the whole band from 3 GHz to 8 GHz, except for a minor violation at 8 GHz. The corresponding improvement in the transmission coefficient is also significant so that it does not exceed 1 dB over the entire frequency range.

3.2.2 Measurement Validation of GCPW Interconnect for High-speed Vertical Connector

To verify the performance of the GCPW interconnects for the high-speed vertical connector, the test board designs described in subsection 3.2.1 are fabricated along with Thru, Reflect, and Line calibration boards (see Figure 3-6). These boards are equipped with edge SMA connectors for 2-port measurements with a vector network analyzer (VNA) (E8363B, Keysight Technologies). In the measurements, the MEC2-40-01-L-DV connector is employed in lieu of MEC2-50-01-L-DV, featuring a 40-pin configuration instead of 50 pins. Aside from the pin number, the 40-pin and 50-pin vertical connectors are identical, and their electromagnetic performance is also identical. Thus, the HFSS encrypted model of the MEC2-DV series vertical connector is valid for any pin count. The 8-term error model [33] is implemented in MATLAB [34] and utilized to de-embed the effect of the edge SMA connectors and their transitions to the GCPW TLs. The de-

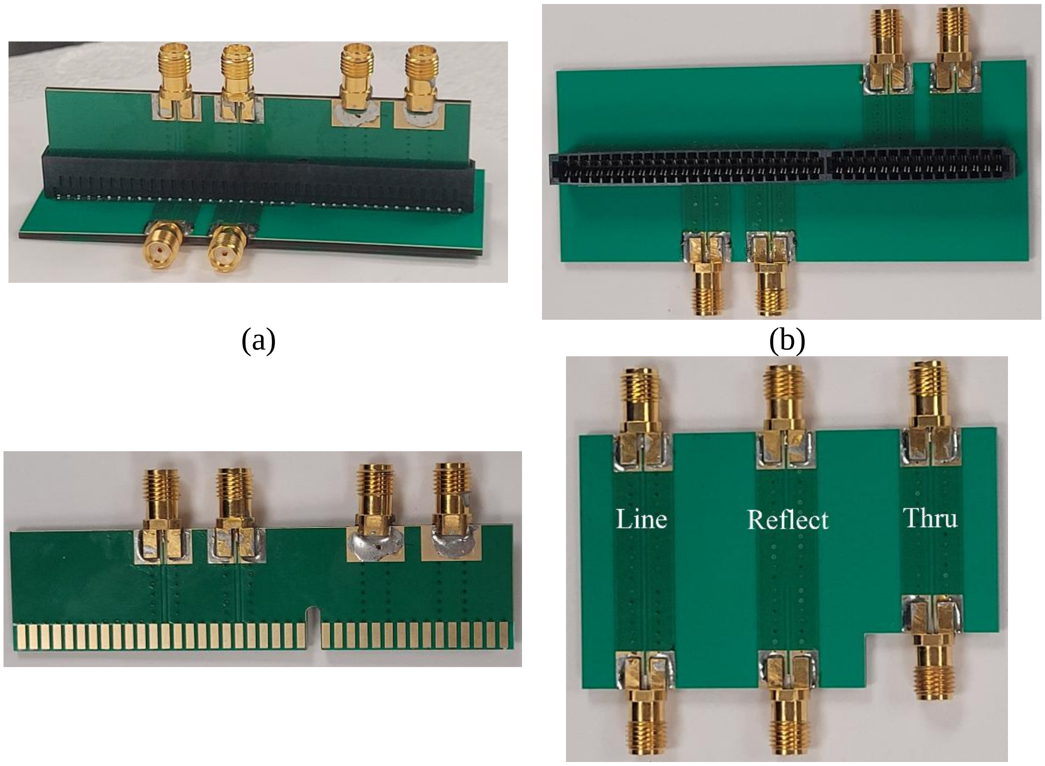

(a) (b)

(c) (d)

Figure 3-6: (a) Assembly showing the vertical test board inserted in the connector mounted on the horizontal test board. (b) GCPW horizontal test board with the mounted vertical board-to-board connector. (c) GCPW vertical test board. (d) GCPW calibration board with Thru, Reflect (Shorted GCPW), and Line GCPW TLs.

embedding requires the 2-port *S*-parameter measurements of the calibration 2-ports (Thru, Reflect, Line) shown in Figure 3-6d.

The *S*-parameters of the assembly in Figure 3-6a are also measured. The obtained four sets of *S* parameters (3 calibration measurements and one device measurement) are imported into the MATLAB code to extract the *S*-parameters of the high-speed vertical connector together with the pin transitions to GCPW TLs. The raw measured *S*-parameters of the assembly in Figure 3-6a are presented in Figure 3-7 along with the de-embedded *S*-parameters. It is observed that, despite the satisfactory simulation results in Figure 3-4, in measurements, the reflection coefficients at Port 1 and Port 2 violate the −10 dB threshold at higher frequencies.

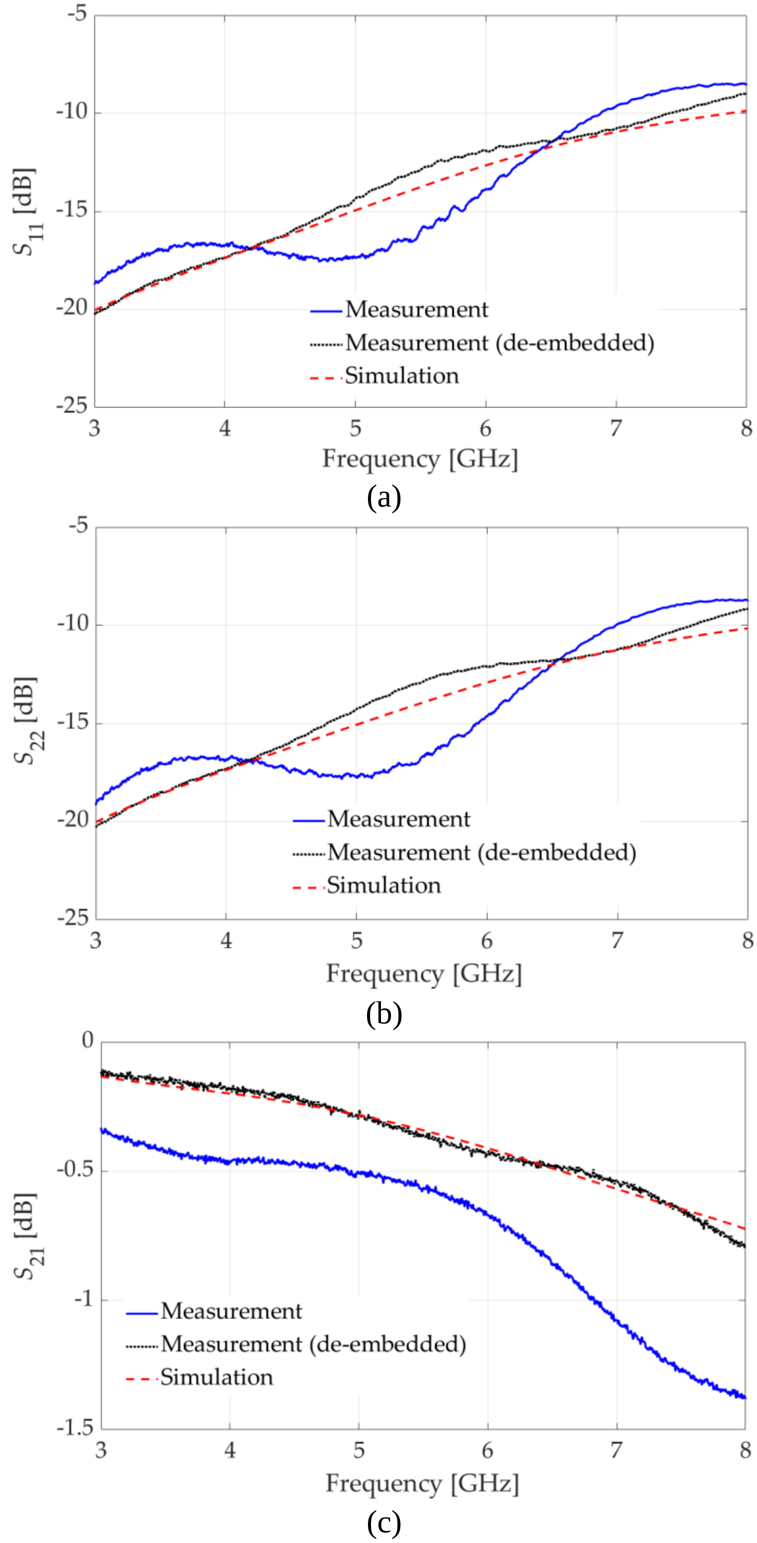

Figure 3-7: Measured, de-embedded and simulated S-parameters of the vertical connector assembly with the GCPW test boards, both of which employ GCPW signal trace width of 0.47 mm and gap width of 0.38 mm: (a) reflection coefficient at Port 1, (b) reflection coefficient at Port 2; (c) transmission coefficient.

To address this problem, a parametric sweep is conducted in HFSS, varying the width of the GCPW signal trace while keeping the gap width intact (0.38 mm). Again, a wave port excitation is employed. Representative results for the parametric sweep are shown in Figure 3-8a, which shows that a signal trace width of 0.38 mm along with a gap width of 0.38 mm provides a better impedance match with some margin below the −10 dB threshold. With this trace width, the HFSS wave port analysis shows a characteristic impedance of 56 Ω on average over the frequency

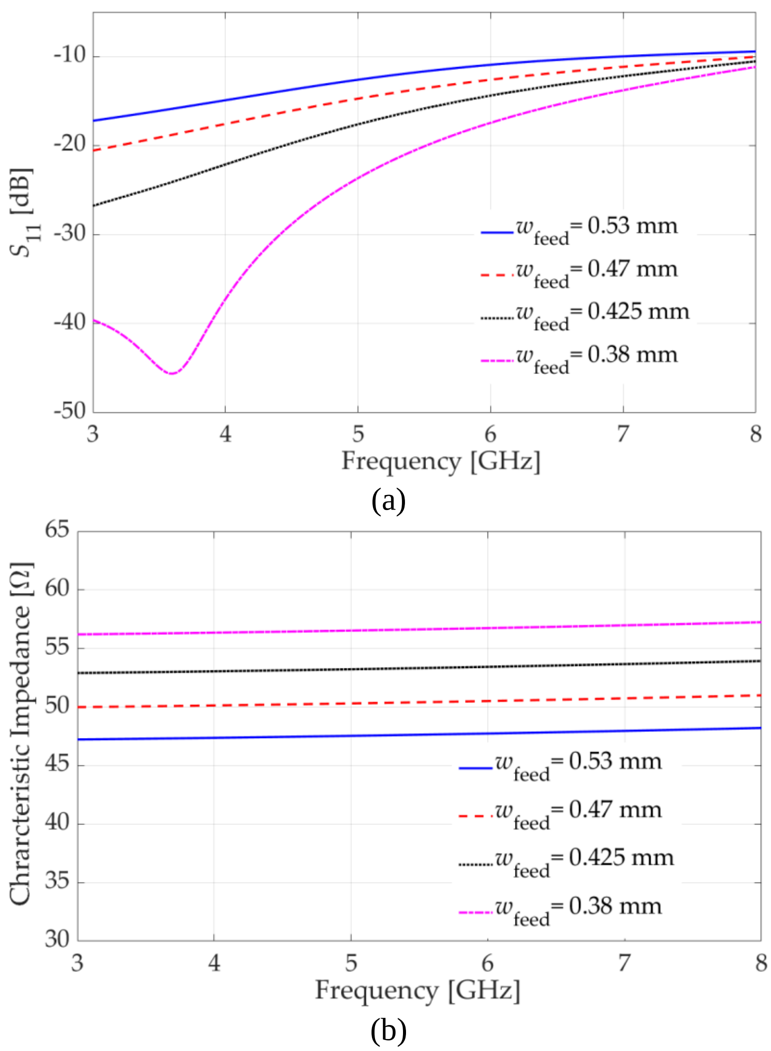

Figure 3-8: Effect of variation in the GCPW signal trace width (w_{feed}) on: (a) the reflection coefficient at Port 1 (generalized S_{11}), (b) the GCPW characteristic impedance on the horizontal board (Port 1). Gap width is fixed at 0.38 mm.

band from 3 GHz to 8 GHz, as shown in Figure 8b (w_{feed} = 0.38 mm). The reflection coefficient at Port 2 has similar behavior.

Another set of GCPW calibration boards and test boards with this trace width w_{feed} = 0.38 mm have been fabricated and measured. Since the characteristic impedance of the GCPW TLs in these boards is 56 Ω on average, and the VNA reference impedance is 50 Ω, a reference impedance conversion [35] is carried out for all sets of measured *S*-parameters (the 3 calibration-board measurements and the assembly measurement) before the de-embedding with the 8-error-term model. Figure 3-9 shows the raw measured *S*-parameters of the assembly with the new test boards compared with simulation results. Figure 3-9 also includes the de-embedded *S*-parameters. Contrary to the first prototype, the measured and de-embedded reflection coefficients of the assembly with the new test boards are well below −10 dB, indicating that the high-speed vertical connector is better matched to 56-Ω GCPW interconnects. We note that there are some discrepancies between the simulated (generalized *S*-parameter) and measured *S*-parameters. The simulations employ wave port excitations, where generalized *S*-parameters are computed (not normalized to a fixed system impedance). These *S*-parameters are expected to match better the de-embedded measured *S*-parameters, where the impact of the SMA connectors is removed and the reference system impedance is set to 56 Ω. This is indeed the case in Figure 3-9, especially at higher frequencies. At lower frequencies, the discrepancy appears larger; however, this is where the reflection coefficients are weak (below −20 dB), and the imperfections in the TRL calibration lead to larger uncertainty on the dB scale.

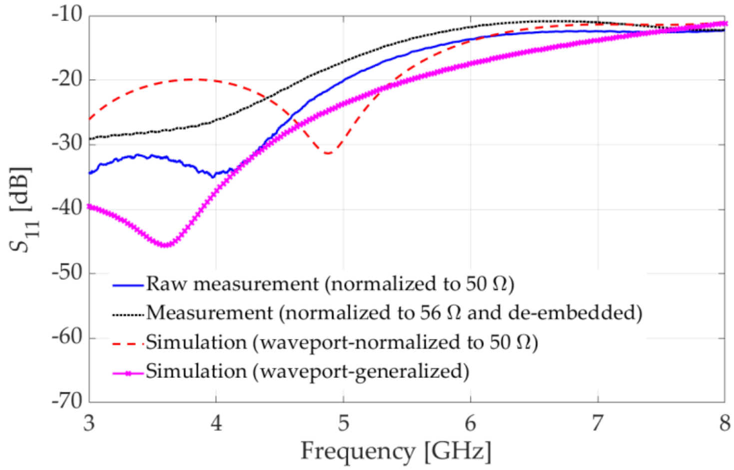

(a)

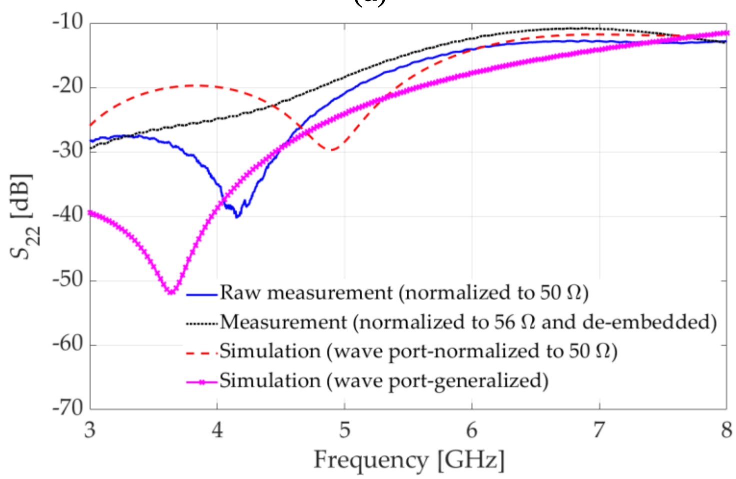

(b)

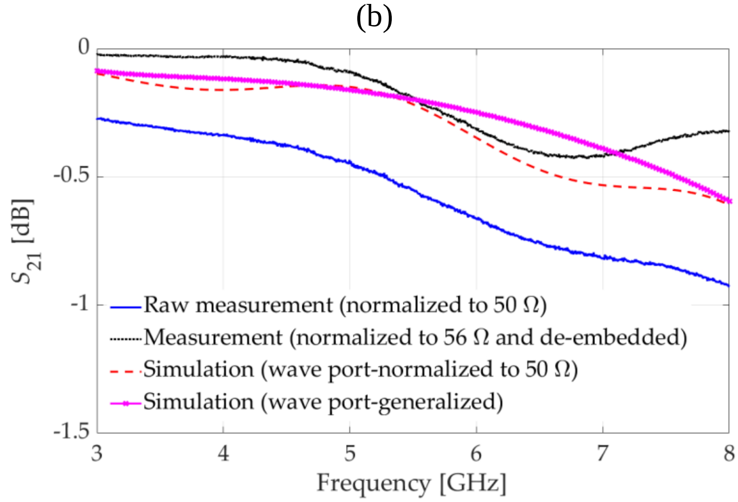

(c)

Figure 3-9: Measured (raw and de-embedded) and simulated *S*-parameters of the vertical connector assembly with test boards with GCPW signal trace width of 0.38 mm and gap width of 0.38 mm: (a) reflection coefficient at Port 1, (b) reflection coefficient at Port 2, (c) transmission coefficient.

3.3 Integration of Vertical Connector with the UWB Active Sensing Array

The high-speed vertical connector is employed in the UWB active sensing array for microwave imaging applications. In such applications, it is important to achieve not only good impedance match but also good decoupling between receiving channels. This is investigated here utilizing a setup in which the connector is integrated with the actual 16×16 UWB active sensing array.

3.3.1 EM Simulation

Initially, the layout of the GCPW interconnect introduced in the preceding section is implemented on the horizontal board at the output of the LNA chip, which is represented simply with a 50-Ω lumped port in HFSS, as indicated in Figure 3-10a (Port 1 and Port 3). The layout of this interconnect is shown in detail in Figure 3-10b. Note that the 56-Ω GCPW interconnect leading to the vertical connector is preceded by a carefully designed bend and a transition to a 50-Ω GCPW at the LNA output. These are critical for maintaining good impedance matches at Ports 1 and 3. The respective ground plane layout is the same as the one in Figure 3-5b. Note that the vertical connectors accommodate two rows of antennas (16 on each side); thus, they must reside between the two antenna rows. This necessitates the right-angle bend from the LNA outputs toward the connector.

Also, the vertical board GCPW interconnect has been implemented on both sides of the board and has been equipped with SMA connectors for RF testing; see Port 2 and Port 4 in Figure 3-10a. The actual model of these SMA connectors is used in HFSS and they are excited by 50-Ω wave port excitations. The details of the GCPW layout at the top and bottom of the vertical board are shown in Figure 3-10c. The ground plane layout for the two GCPWs on the vertical board is shown in Figure 3-10d. The purposeful creation of voids within the ground planes beneath the SMA connectors is critical for achieving good impedance matches on Ports 2 and 4. Another design feature is the transition from the GCPW to the footprint of the SMA connector, which impacts the impedance match as well. We reiterate the importance of the partial ground planes on the vertical board such that the

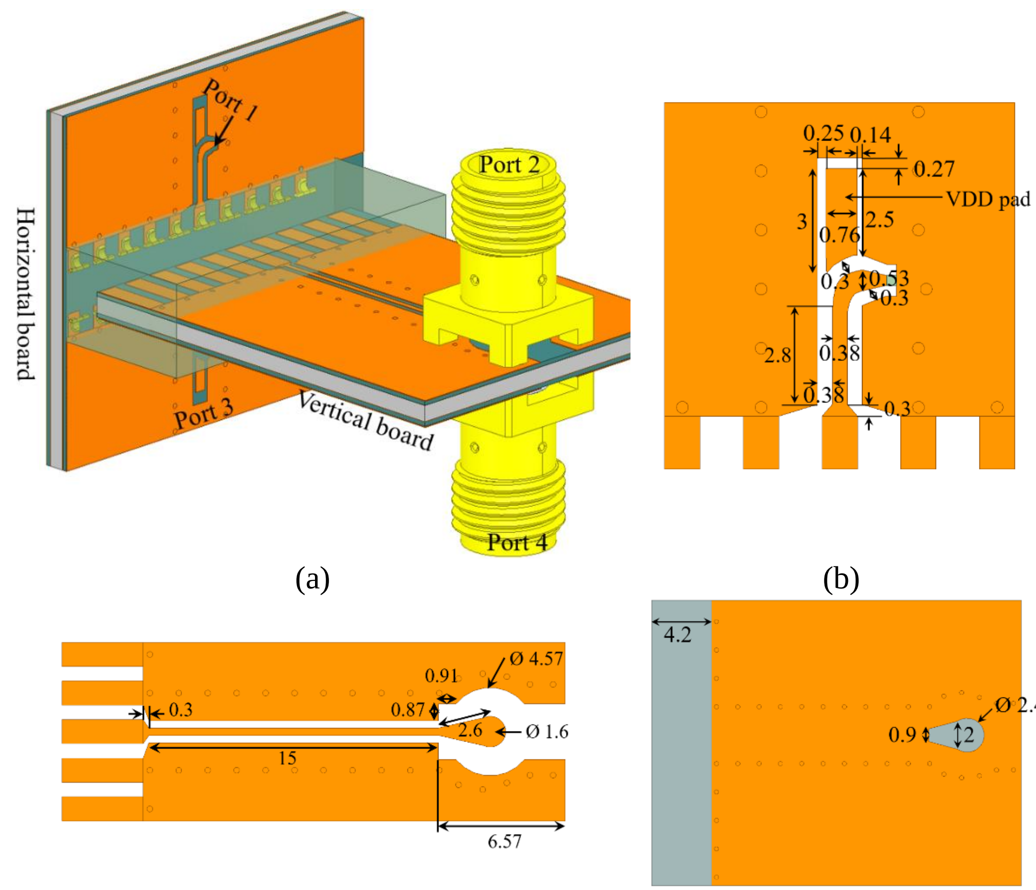

Figure 3-10: (a) Assembly showing the horizontal board with its transition path from the LNA to the vertical connector and the vertical board equipped with two SMA connectors for RF testing. (b) Top-layer layout on the horizontal board (LNA side) with dimensions in mm. The ground plane of this GCPW interconnect is the same as the one in Figure 5b. (c) Top-layer layout on the vertical board (SMA side) with dimensions in mm. (d) Partial ground plane of the vertical board with dimensions in mm. Circles in grey indicate grounding via-holes.

metallization is removed in the PCB section that is inserted in the connector. These sections are visible in Figure 3-10d to the left of the partial ground plane.

A 4-port *S*-parameter analysis with a frequency sweep from 3 GHz to 8 GHz is performed in HFSS. The port assignment is indicated in Figure 3-10a. The 4-port *S*-parameters are shown in Figure 3-11. As observed in Figure 3-11a, the reflection coefficients are well be-low −10 dB. The "through" transmission coefficients between Ports 1 and 2, as well as Ports 3 and 4, are plotted in Figure 3-11b. They are better than −1 dB, which indicates high-quality transmission.

Figure 3-11c summarizes the mutual coupling transmission coefficients, which describe undesirable crosstalk between ports. In imaging, it is important to channel the signal received by a sensor to its respective output but not to outputs associated with its neighbors. Thus, Port 1 should “talk” to Port 2, but not to Port 4 Similarly, Port 3 should “talk” to Port 4, but not to Port 2. Therefore, the crosstalk between Ports 1 and 4 as well as Ports 2 and 3 must be below −20 dB, and the respective *S*-parameters (S_{41} and S_{23}) meet this goal.

On the other hand, the crosstalk between Ports 2 and 4 (both on the vertical PCB) is less important in our application since both of these ports are outputs, i.e., there is no signal injection at these ports. These are ports leading to the RF inputs of separate mixers. Similarly, the crosstalk between Ports 1 and 3 (both on the horizontal PCB) is less important since a crosstalk due to a signal from the LNA at one of these ports is dissipated by the output resistance of the LNA at the other port. However, in other application it may be important to supress this crosstalk represented by the transmission coefficients S_{31} and S_{42}. As is evident from Figure 3-11c, these *S*-parameters exceed the threshold of −20 dB significantly (by more

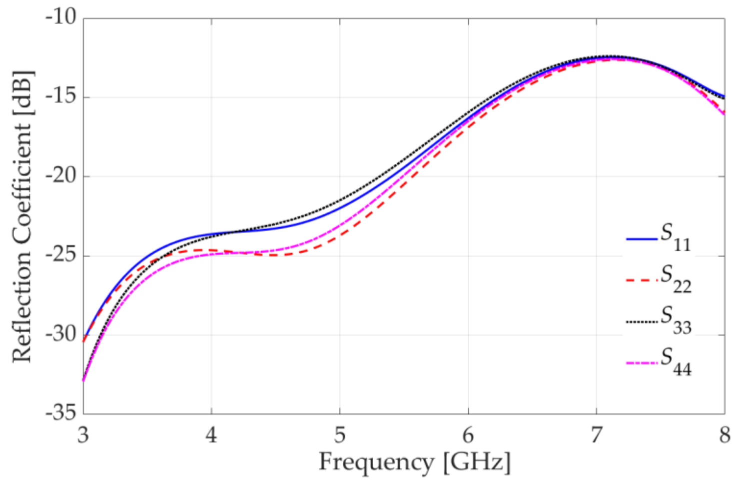

(a)

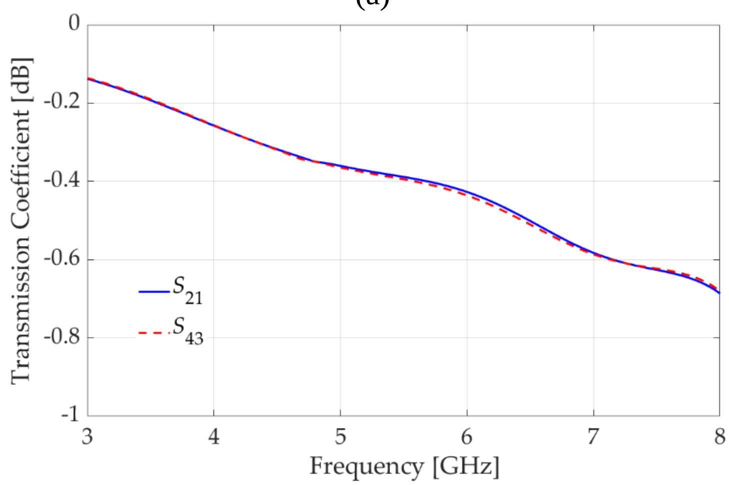

(b)

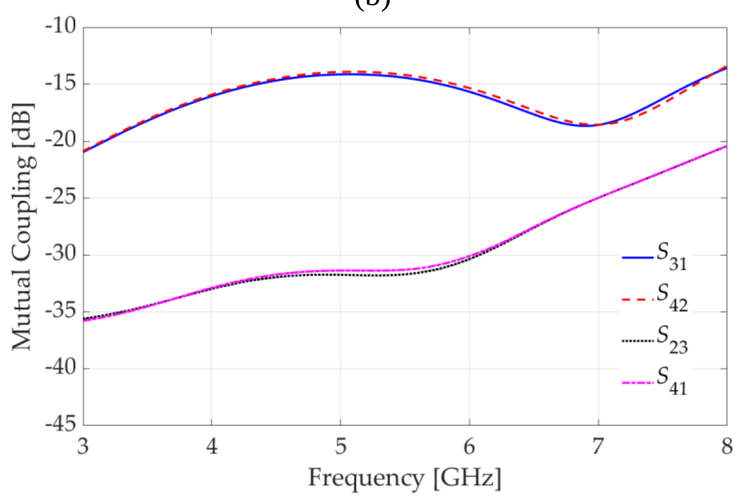

(c)

Figure 3-11: Simulated *S*-parameters of the configuration in Figure 10: (a) reflection coefficients in dB at all 4 ports, (b) "through" transmission coefficients between Ports 1 and 2 as well as Ports 3 and 4, (c) "mutual-coupling" (crosstalk) transmission coefficients.

than 5 dB). To mitigate this crosstalk, two additional partial ground planes (one ground plane per GCPW) are introduced on the vertical board as shown in Figure 3-12a. A parametric sweep is executed on the length of the de-metallized segment, leading to the optimal choice of 2.1 mm as indicated in Figure 3-12a. However, the inclusion of these additional ground planes negatively impacts all reflection coefficients. To counteract this effect, the ground plane slots beneath the SMA connectors are modified as shown in Figure 3-12b.

The *S*-parameters of the final design are plotted in Figure 3-13. The reflection coefficients (Figure 3-13a) remain below −10 dB, and the "through" transmission coefficients (Figure 3-13b) are better than −1 dB. The crosstalk (Figure 3-13c) between Ports 2 and 3, as well as Ports 1 and 4, remains well below

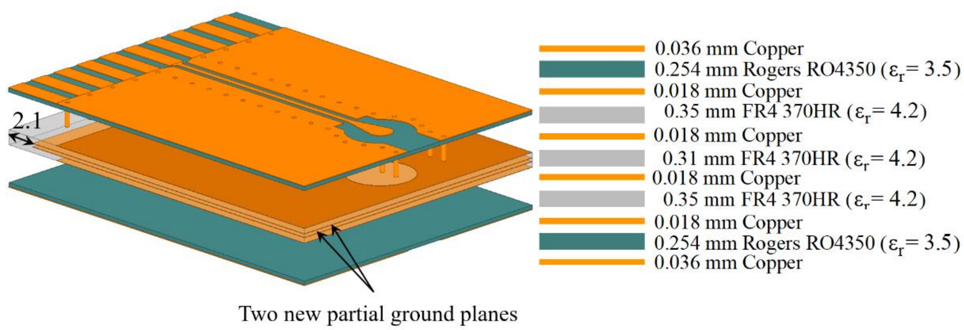

(a)

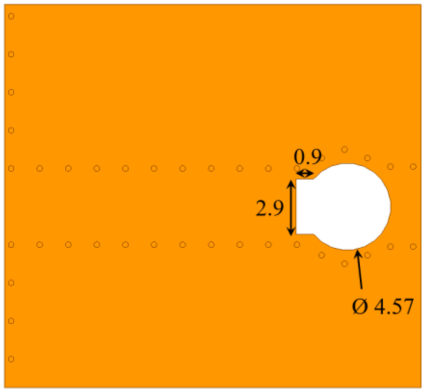

(b)

Figure 3-12: (a) Placement of two additional partial ground planes on the vertical board. (b) Adjustments made to the slots in the ground planes directly beneath the SMA connectors. Circles in grey and cylinders indicate grounding via-holes.

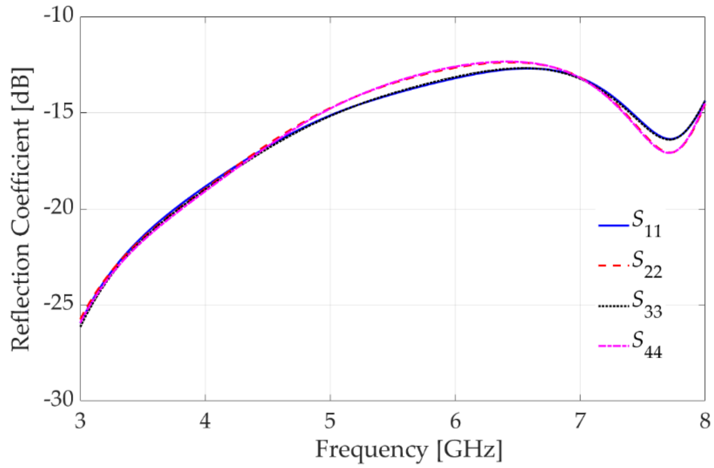

(a)

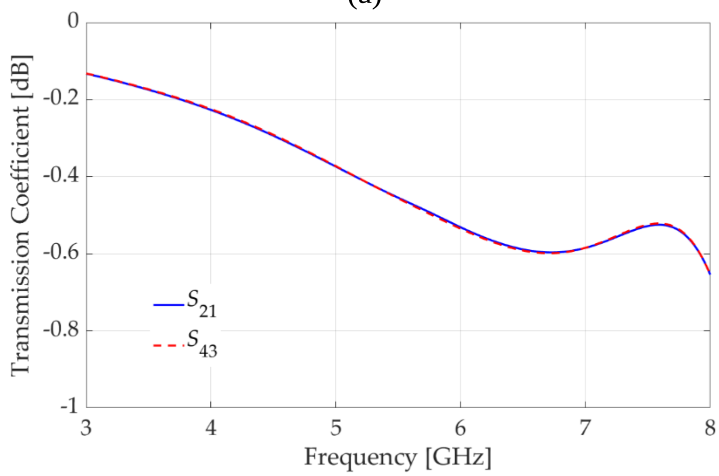

(b)

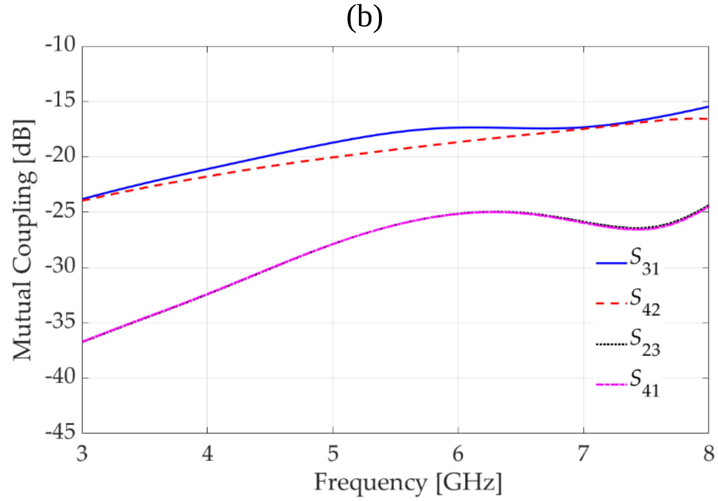

(c)

Figure 3-13: Simulated *S*-parameters of the modified configuration presented in Figure 3-12: (a) reflection coefficients in dB at 4 ports, (b) "through" transmission coefficient between Ports 1 and 2 as well as Ports 3 and 4, (c) "mutual-coupling" (crosstalk) transmission coefficient between ports.

−20 dB whereas that between Ports 2 and 4 as well as Ports 1 and 3, is now improved to be consistently below −15 dB.

4.3.2. Measurement Validation

To compare the RF connectivity offered by the high-speed vertical connectors with that of the SMPS connectors, two prototypes of the UWB active sensing array are utilized. The first prototype is the original SMPS-connectorized 6×6 array described in [25]. Its photo is shown in Figure 3-14. The second prototype is the new 16×16 array (see Figure 3-2) designed to accommodate the vertical connector. As seen in Figure 3-2, a 16×16 array can be built from identical array tiles, each housing 64 active antenna elements. A photo of one such tile is shown in Figure 3-15. This tile is used to carry out the comparison with the original SMPS-connectorized 6×6 array in Figure 3-14. A vertical test board is also fabricated in accordance with the GCPW vertical-board design presented in subsection 3.3.1. It is inserted in one of the vertical connectors of the Rx array tile as shown in the photo in Figure 3-16a.

As shown in Figure 3-16a, a transmit-receive setup is put together, where a dielectric-filled transverse electromagnetic (TEM) horn [36] is used as the Tx antenna; see Figure 3-16c. The Tx antenna and the Rx active array (either the SMPS-connectorized 6×6 array or the new array tile with the vertical connector) are placed on the opposite sides of a stack of three 11 mm-thick custom-made carbon-rubber slabs with complex permittivity of $\varepsilon_r \approx 9.6 - i3.8$ (averaged over the frequency band from 3 GHz to 8 GHz). The slab material mimics the dielectric properties of healthy breast tissue. Figure 3-16a shows the setup, where the Tx

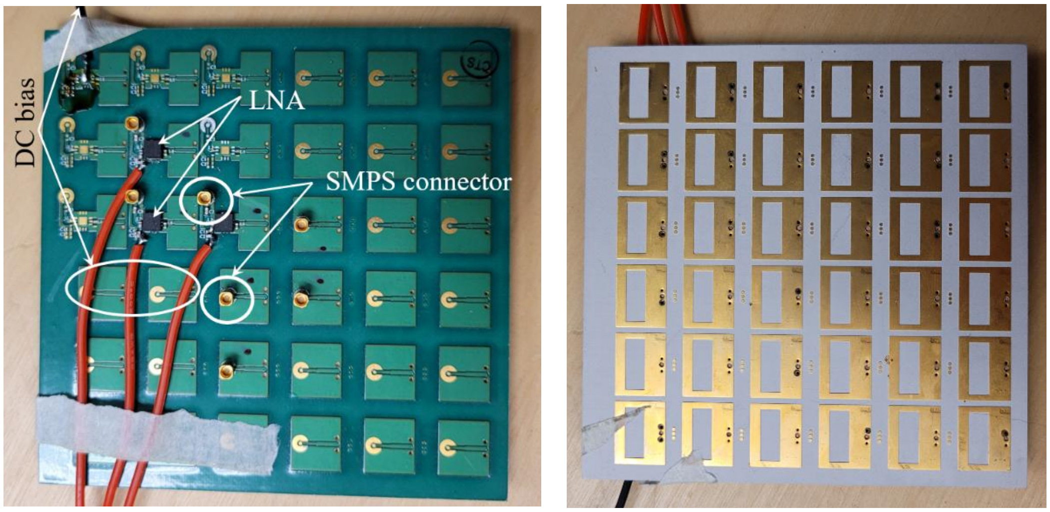

(a) (b)

Figure 3-14: Photo of the original SMPS-connectorized 6×6 array described in [25]: (a) electronic layer, where 3 array elements are active (with LNA chips), (b) slot layer that comes in direct contact with tissue.

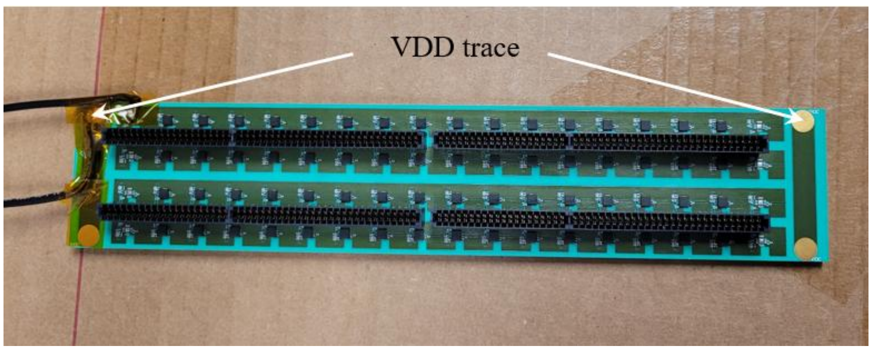

Figure 3-15: Electronics (top) layer of one of the five fabricated array tiles used to build a 16×16 UWB sensing array prototype. The slot (bottom) layer (not shown) contains 4 rows of 16 slots, which are identical to those in Figure 3-14b. The tile accommodates 64 active sensors and 8 dummy array elements at the left and right ends of the PCB. The active sensors are equipped with LNA chips whose outputs lead to the vertical connector pins.

antenna is beneath the breast-tissue phantom. The Tx antenna is connected to Port 1 of the VNA, and its aperture comes in direct contact with the tissue phantom. On the opposite (top) side, the Rx array slots also come in direct contact with the breast phantom. One of these slots is aligned along boresight with the Tx horn antenna. This slot belongs to the active sensor element whose output on the vertical test

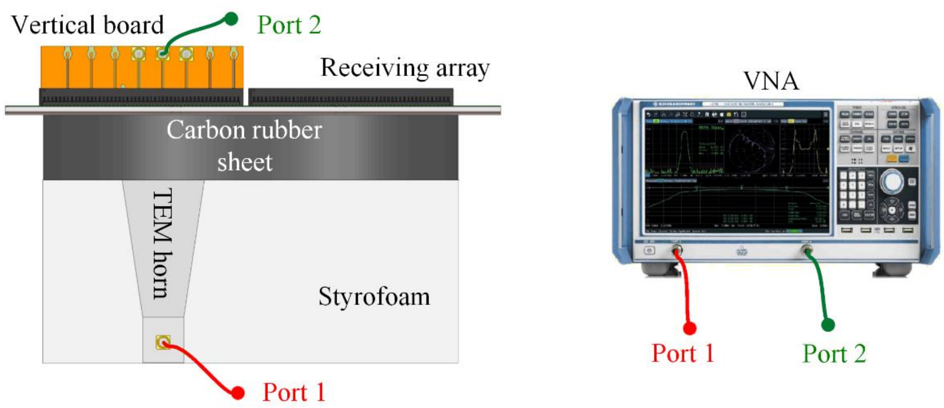

(a)

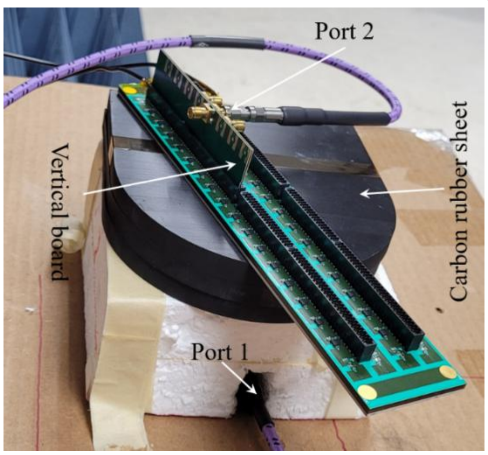

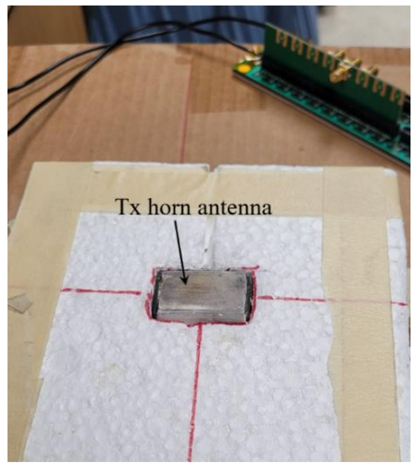

(b) (c)

Figure 3-16: (a) The schematic of measurement setup of transmit-receive configuration. (b) The measurement setup of the transmit-receive configuration, where the Tx antenna and the Rx array assembly are separated by three 11 mm-thick circular carbon-rubber sheets, mimicking the electrical properties of healthy breast tissue. (c) TEM dielectric horn [36] used as the Tx antenna.

board is equipped with an SMA connector, which in turn is connected to Port 2 of the VNA. The exact same Tx antenna, arrangement and alignment are used when measuring the received signal with one of the elements of the SMPS-connectorized 6×6 array. We emphasize that the sensing elements of the 6×6 array and the new Rx array tiles are identical, except for the different connectors at their outputs.

The S_{21} (through) transmission coefficients (in dB, through the tissue phantom) measured with the two Rx arrays are shown in Figure 3-17. It is evident that the RF connection provided by the high-speed vertical connector is of

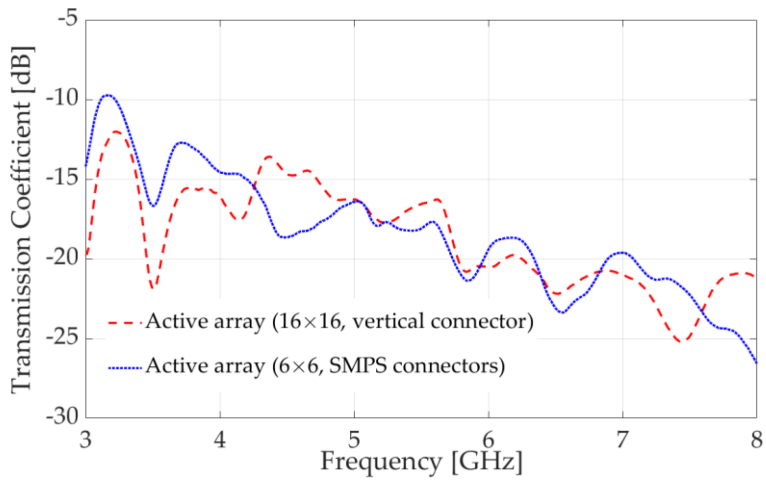

Figure 3-17: Measured "through" transmission coefficient with the two active Rx arrays: one employing a high-speed vertical connector and the other employing SMPS connectors.

comparable quality to that of the SMPS connectors. We note that the active Rx antenna elements on the PCB, including the vertical connectors and their interconnects, are expected to have identical reception performance. However, quantifying the array reception uniformity requires an equally repeatable transmission performance, which can be achieved only with precision alignment of the Tx and Rx antenna elements. The development of a printed Tx antenna array, which provides such alignment, is still ongoing.

3.4 Discussion

This study is an integral part of the development of a large-scale, densely packed electronically switched antenna array for biomedical imaging in the frequency range from 3 GHz to 8 GHz, with a focus on the receiving array. The IF-switched architecture enables the multiplexing of hundreds of array elements in contrast to the conventional RF-switched architecture, which is limited to several tens of sensors. While our IF-switched imaging system is work in progress, preliminary studies suggest that employing switching circuits at the IF frequency of 30 MHz offers the following advantages over switching at RF frequencies in the UWB range: (i) insertion loss less than 1 dB compared to 6 dB at UWB, (ii) isolation better than 60 dB compared to 20 dB at UWB, (iii) return loss better than 25 dB compared to 10 dB in UWB, and (iv) easy design of the inter-connecting transmission lines with superior amplitude and phase uniformity across all 256 channels.

However, an IF-switched sensing array requires the integration of each antenna with an RF front-end. The limited space on the antenna board (12 mm in both x and y directions), coupled with the lack of a single chip platform for low noise amplification and frequency conversion over the wide frequency band (3 GHz to 8 GHz), dictates that the antenna array board can only accommodate the LNA chips. Therefore, a separate board becomes necessary to house the mixer array, the LO distribution network, and the IF-switching network. The seamless transition between these two boards is of paramount importance.

In this manuscript, the primary focus is on the development of mechanically robust, low cost, and low crosstalk connections between the UWB active antenna array board and its corresponding mixer boards. SMPS connectors, due to size, cost, and reliability concerns, were found inadequate for the task. As an alternative, we turn to high-speed digital board-to-board vertical connectors, known for their high pin density, mechanical and electrical durability, and affordability. We explore a particular off-the-shelf connector (MEC2-50-01-L-DV) within the UWB frequency range for establishing efficient board-to-board microwave connections. The interfacing of this connector with microstrip lines is well documented by the manufacturer. However, GCPW TLs are preferred in UWB technology. This study shows that, while the connector can indeed be connected to GCPWs on both the horizontal and vertical boards, it is not sufficient to simply attach a 50-Ω GCPW to the connector's pins. Careful design and simulation-based optimization have been reported here that target not only the GCPW signal trace and gap widths but also slots in the GCPW ground plane layer as well as ground plane de-metallization (partial ground plane). The proposed design achieves very good microwave performance with reflection loss better than 10 dB, insertion loss well below 1 dB, and mutual coupling (crosstalk) below −20 dB.

The designed GCPW interconnects for the high-speed vertical connector have been employed here to integrate a 16×16 UWB active sensing array (horizontal) board with vertical boards. However, the proposed board-to-board GCPW transitions can also be employed in many other UWB applications where simultaneous seamless microwave signal transfer is needed for hundreds of channels.

It is worth noting that there is a great variety of other printed transmission lines, e.g., CPWs without a ground plane, differential, strip, and slot lines, and the ways to interface these with high-speed board-to-board connectors are yet to be investigated.

3.5 Conclusion

We have proposed an efficient method to interconnect hundreds of GCPW input/output signal paths on two separate PCBs (one horizontal and the other vertical) based on widely available low-cost high-speed digital vertical connectors.

This development enables the realization of large-scale high density electronically scanned or switched antenna arrays, which are critical in wireless communications as well as in microwave radar, imaging, and sensing. Excellent RF performance has been demonstrated in the UWB band through simulations and measurements in terms of reflection loss, insertion loss and channel crosstalk.

Appendix A

The development described above has enabled the successful assembly of a large-scale 16×16 active Rx array, as illustrated in Figure 3-18.

Figure 3-18: The complete 16×16 active Rx array with heat sinks installed over each row of antennas to effectively dissipate the heat generated by LNAs.

3.6 References

[1] S. Das, S. K. Sharma, S. W. Waldstein, J. M. Downey, B. L. Schoenholz, S. M. Dever, J. A. Nessel, R. A. Banerjee, “Flat-Panel 8× 8 Wideband K–/Ka–Band Dual Circularly Polarized Phased Array Antenna for CubeSat Communications,” *IEEE Trans. Antennas Propag.*, vol. 71, pp. 4153-4166, Mar. 2023.

[2] M. Nouri, H. Behroozi, A. Jafarieh, S. A. Aghdam, M. J. Piran, and N. K. Mallat, “A learning-based dipole Yagi-Uda antenna and phased array antenna for mmWave precoding and V2V communication in 5G systems,” *IEEE Trans. Veh. Technol.*, vol. 72, no. 3, pp. 2789–2803, Oct. 2022

[3] A. H. Naqvi and S. Lim, “Review of recent phased arrays for millimeter-wave wireless communication,” *Sensors*, vol. 18, no. 9, pp. 3194, Sep. 2018.

[4] G. Yang and S. Zhang, “Dual-polarized wide-angle scanning phased array antenna for 5G communication systems,” *IEEE Trans. Antennas Propag.*, vol. 70, no. 10, pp. 7427–7438, Jan. 2022.

[5] K. Tang, L. Lou, T. Guo, B. Chen, Y. Wang, Z. Fang, C. Yang, W. Wang, and Y. Zheng, “A 4TX/4RX pulsed chirping phased-array radar transceiver in 65-nm CMOS for X-band synthetic aperture radar application,” *IEEE J. Solid-State Circuits*, vol. 55, no. 11, pp. 2970–2983, Jul. 2020.

[6] J. O. Plouchart, X. Gu, W. Lee, A. Tzadok, D. Liu, H. Liu, M. Yeck, C. Baks, A. Valdes-Garcia, “Si-based 94-GHz phased array transmit and receive modules for real-time 3D radar imaging,” *IEEE MTT-S Int. Microw. Symp.*, pp.532-535, Jun. 2019.

[7] M. T. Ghasr, S. Kharkovsky, R. Bohnert, B. Hirst, and R. Zoughi, “30 GHz linear high-resolution and rapid millimeter wave imaging system for NDE,” *IEEE Trans. Antennas Propag.*, vol. 61, no. 9, pp. 4733–4740, Jun. 2013.

[8] Y. Gao, M. Ravan, and R. K. Amineh, “Fast, robust, and low-cost microwave imaging of multiple non-metallic pipes,” *Electronics*, vol. 10, no. 14, pp. 1762, Jul. 2021.

[9] M. Klemm, D. Gibbins, J. Leendertz, T. Horseman, A. W. Preece, R. Benjamin, and I. J. Craddock, “Development and testing of a 60-element UWB conformal array for breast cancer imaging,” *in Proc. 5th Eur. Conf. Antennas Propag. (EUCAP)*, pp. 3077–3079, Apr. 2011.

[10] M.T. Islam, M.Z. Mahmud, M.T. Islam, S. Kibria, and M. Samsuzzaman, “A low cost and portable microwave imaging system for breast tumor detection using UWB directional antenna array,” *Sci. Rep.*, vol. 9, no. 1, pp. 1-13, Oct. 2019.

[11] E. Porter, H. Bahrami, A. Santorelli, B. Gosselin, L.A. Rusch, and M. Popović, “A wearable microwave antenna array for time-domain breast tumor screening,” *IEEE Trans. Med. Imaging*, vol. 35, no. 6, pp. 1501-1509, Jan. 2016.

[12] H. Song, S. Sasada, T. Kadoya, M. Okada, K. Arihiro, X. Xiao, and T. Kikkawa, “Detectability of breast tumor by a hand-held impulse-radar detector: performance evaluation and pilot clinical study,” *Sci. Rep.*, vol. 7, p. 16353, Nov. 2017.

[13] G. Yang, Y. Zhang, and S. Zhang, "Wide-band and wide-angle scanning phased array antenna for mobile communication system," *IEEE Open J. Antennas Propag.*, vol. 2, pp. 203–212, Feb. 2021.

[14] Y. Kim, H. Y. Lee, P. Hwang, R. K. Patro, L. Lee, W. Roh, and K. Cheun, "Feasibility of mobile cellular communications at millimeter wave frequency," *IEEE J. Sel. Top. Signal Process.*, vol. 10, no. 3, pp. 589–599, Jan. 2016.

[15] M. S. Sharawi, S. Deif, and A. Shamim, "An electronically controlled 8-element switched beam planar array," *IEEE Antennas Wirel. Propag. Lett.*, vol. 14, pp. 1350–1353, Feb. 2015.

[16] P. Sanchez-Olivares, P. P. Sanchez-Dancausa, and J. L. Masa-Campos, "Circularly conformal patch array antenna with omnidirectional or electronically switched directive beam," *IET Microw. Antennas Propag.*, vol. 11, no. 14, pp. 2253–2259, Dec. 2017.

[17] Z. Ding, J. Chen, H. Zhou, and R. Jin, "Two-dimensional scanning phased array with large element spacing using pattern reconfigurable stacked patch antenna at Ka-band," *IEEE Trans. Antennas Propag.*, vol. 70, no. 8, pp. 5447–5457, Mar. Mar. 2022.

[18] M. T. Ghasr, M. J. Horst, M. R. Dvorsky, and R. Zoughi, "Wideband microwave camera for real-time 3-D imaging," *IEEE Trans. Antennas Propag.*, vol. 65, no. 6, pp. 258–268, Nov. 2016.

[19] M. T. Ghasr, M. A. Abou-Khousa, S. Kharkovsky, R. Zoughi, D. and Pommerenke, "Portable real-time microwave camera at 24 GHz," *IEEE Trans. Antennas Propag.*, vol. 60, no. 2, pp. 1114-1125, Oct. 2011.

[20] J. Zhang, S. Zhang, Z. Ying, A. S. Morris, and G. F. Pedersen, "Radiation-pattern reconfigurable phased array with pin diodes controlled for 5G mobile terminals," *IEEE Trans. Microw. Theory Tech.*, vol. 68, no. 4, pp. 1103–1117, Dec. 2019.

[21] S. Verho, V. T. Nguyen, and J. Y. Chung, "A 4×4 active antenna array with adjustable beam steering," *Sensors*, vol. 23, no. 4, p. 1324, Jan. 2023.

[22] J. G. Nicholls and S. V. Hum, "Full-space electronic beam-steering transmit array with integrated leaky-wave feed," *IEEE Trans. Antennas Propag.*, vol. 64, no. 8, pp. 3410–3422, Jun. 2016.

[23] D. Kim, M. Hwang, G. Kim, and S. Kim, "Self-Deployable Circularly Polarized Phased Yagi–Uda Antenna Array Using 3-D Printing Technology for CubeSat Applications," *IEEE Antennas Wirel. Propag. Lett.*, vol. 21, no. 11, pp. 2249-2253, Aug. 2022.

[24] F. Foroutan and N. K. Nikolova, "Active sensor for microwave tissue imaging with bias-switched arrays," *Sensors*, vol. 18, E1447, May 2018.

[25] N. V. Shahmirzadi, V. Tyagi, J. Nguyen, R. Kazemivala, N. K. Nikolova, and C.H. Chen, "Planar array of UWB active slot antennas for microwave imaging of the breast," *IEEE Trans. Antennas Propag.*, vol. 71, no. 4, pp. 2946-2957, Jan. 2023

[26] R&S® *ZNA43 Vector Network Analyzer 2 Ports*. Accessed: Aug. 2023. [Online]. Available: https://www.rohde-schwarz.com/ca/products/test-and-measurement/network-analyzers/rs-zna-vector-network-analyzers_63493-551810.html.

[27] T. Sugitani, S.I. Kubota, S.I. Kuroki, K. Sogo, K. Arihiro, M. Okada, T. Kadoya, M. Hide, M. Oda, and T. Kikkawa, “Complex permittivities of breast tumor tissues obtained from cancer surgeries,” *Appl. Phys. Lett.*, vol.104, no. 25, Jun. 2014.

[28] M. Lazebnik, L. McCartney, D. Popovic, C. B. Watkins, M. J. Lindstrom, J. Harter, S. Sewall, A. Magliocco, J. H. Booske, M. Okoniewski, and S. C. Hagness, “A large-scale study of the ultrawideband microwave dielectric properties of normal breast tissue obtained from reduction surgeries,” *Phys. Med. Biol.*, vol. 52, no. 10, pp. 2637–2656, Apr. 2007.

[29] *ACR BI-RADS ATLAS-MAMMOGRAPHY*. Accessed: Aug. 25, 2023. [Online]. Available: https://www.acr.org/-/media/ACR/Files/RADS/BI-RADS/Mammography-Reporting.pdf

[30] Samtec. *MEC2-50-01-L-DV*. Accessed: Aug. 25, 2023. [Online]. Available: https://www.samtec.com/products/mec2-50-01-l-dv.

[31] Samtec. High-speed characterization report MEC2-XX-01-L-DV. *Samtec Inc Tech. Rep*. 2013.

[32] Ansys Corporation. *HFSS 2021 R2*. Accessed: May 10, 2022. [Online]. Available: https://www.ansys.com/

[33] G. F. Engen and C. A. Hoer, “Thru-reflect-line: An improved technique for calibrating the dual six-port automatic network analyzer,” *IEEE Trans. Microw. Theory Techn.*, vol. 27, no. 12, pp. 987–993, Dec. 1979.

[34] The MathWorks Inc. *MATLAB R2021b*. Accessed: Aug. 10, 2023. [Online]. Available: https://www.mathworks.com/

[35] Steer, M. *Microwave and RF design*. Raleigh, NC, USA, 2019.

[36] R. K. Amineh, A. Trehan, and N. K. Nikolova, “TEM horn antenna for ultra-wide band microwave breast imaging,” *Prog. Electromagn. Res. B*, vol. 13, pp. 59–74, 2009.

Chapter 4

4. Transmitting Array for an Electronically Switched Microwave Breast Imager

Preface

This chapter is a reproduction of the following submitted article:

N. V. Shahmirzadi, N. K. Nikolova, and C. H. Chen, “Transmitting array for an electronically switched microwave breast imager,” *IEEE Transactions on Antennas and propagation*, submitted, Nov. 2024.

Author Contributions: Conceptualization, N. K. Nikolova; methodology, N. V. Shahmirzadi, A. D. Pitcher, N. K. Nikolova, and C.-H. Chen; validation, N. V. Shahmirzadi and N. K. Nikolova; investigation, N. V. Shahmirzadi, N. K. Nikolova, and C.-H. Chen; resources, N. K. Nikolova; writing—original draft preparation, N. V. Shahmirzadi; writing—review and editing, N. V. Shahmirzadi, A. D. Pitcher, N. K. Nikolova, and C.-H. Chen; supervision, N. K. Nikolova, and C.-H. Chen; project administration, N. K. Nikolova; funding acquisition, N. K. Nikolova

4.1 Introduction

The applications of microwave technology in biomedicine have garnered significant interest in recent years due to its potential for new non-invasive and non-ionizing diagnostic methods. These applications span sensing, monitoring (e.g., heart and breathing rates [1], blood flow and blood pressure [2]), and imaging (e.g., cancer detection [3]-[7], bone imaging [8], brain stroke detection and monitoring [9]-[11], and cardiac imaging [12]). Among these applications, early-stage breast cancer diagnostics has been the focus of extensive research due to the need for greater accessibility and better diagnostic accuracy of the breast-cancer screening programs [3]. Early detection through screening is crucial for high survival rates [13]. X-ray mammography remains the first-line imaging exam in breast-cancer screening, but its limitations in sensitivity (especially in radiologically dense tissue) [3], [14]-[16] and the exam frequency [17], [18] make it less effective than what medical professionals would like to achieve, often necessitating adjunctive ultrasound and magnetic resonance imaging (MRI) exams. These challenges motivate global research on microwave breast imaging as a stand-alone or a complementary early detection method [19]-[26].

The transmitting (Tx) and receiving (Rx) antennas are critical components of the microwave imaging systems. They must ensure good impedance match in the chosen frequency band of operation while being placed in close proximity to or in direct contact with the tissue. High efficiency is required along with near-field distribution that optimizes the performance of the image reconstruction method. Importantly, high quality imaging requires dense spatial sampling, as dictated by the Nyquist criterion. This sampling must extend over electrically large acquisition apertures surrounding the imaged organ, resulting in a large number of measurement points. At the same time, clinical applications favor shorter times for examining a patient. If the data acquisition is to last a couple of minutes, the measurement time per spatial sample cannot exceed 0.5 s with 200 samples or more, which is usually the case in breast imaging. Such speed is not possible with mechanical scanning while ensuring good positioning accuracy and a complete stop during the RF measurement. This is why electronic scanning is a necessity, which requires the development of large, dense antenna arrays.

The array design is challenging as it must achieve inter-element spacing of about half wavelength at the center frequency of operation, which limits the element size and increases mutual coupling. Mutual coupling not only alters the input impedance of the individual elements but, in Rx arrays, it degrades the signal dynamic range [27]. Since the inter-element spacing often falls short of the desired spatial sampling density, electronic scanning may be supplemented with mechanical scanning [19], [21], [23], achieving finer spatial sampling within reasonable measurement time.

The challenge increases when measurements cover a wide frequency range. Many recent systems operate within the ultra-wideband (UWB) frequency spectrum (3.1 GHz to 10.6 GHz), achieving a balance between penetration depth and image resolution. Both frequency-sweep [23], [27], [28] and time-domain methods [29]-[31] are used in UWB breast-imaging systems, which employ various antenna types [32], [33]. Shielded or cavity-backed slot antennas are often preferred due to their wide bandwidth, compact size, and excellent front-to-back ratio, which make them well-suited for integration into diverse array configurations [27]-[29].

UWB imaging systems often operate with switched arrays, where some elements transmit while others receive, controlled by switching networks. The RF switching networks also face limitations when scaled to control large arrays. Managing hundreds of elements necessitates cascaded networks, which not only introduce loss but also face challenges in providing reliable RF interconnects to all antenna ports. To overcome these limitations on the Rx side, we recently proposed a novel architecture for an electronically switched microwave imager [34], where the multiplexing of hundreds of active antennas [27] is done at a single tone low intermediate frequency (IF) (e.g., 30 MHz). A single tone IF switched network has the advantages of low loss, excellent channel isolation, and easy impedance match. However, this Rx array must be complemented by a Tx array, which, too, is composed of hundreds of antennas. But these antennas are passive; thus, the Tx array requires RF feed networks, which must present good impedance match to the antenna elements in the UWB range, along with reliable high-quality RF interconnects. This is the focus of the work presented here.

We present a 16×16 Tx array of passive shielded slot antenna elements with 12 mm inter-element spacing in both lateral directions. The array is realized using multi-layer printed circuit board (PCB) technology. Its geometry matches that of the Rx array detailed in [27] as the two arrays work in tandem while placed on the two opposite sides of the compressed breast. The design of an efficient RF feed network for such a large, dense array becomes possible due to the following major development. The 256 densely packed array elements cannot be terminated with the common sub-miniature version A (SMA) surface-mount coaxial connectors, which are too large. The array can accommodate only subminiature push-on sub-micro (SMPS) coaxial connectors [27], but these are expensive and lack interconnect reliability, repeatability, and mechanical rigidity. Instead, we employ a recently developed impedance matching technique to achieve seamless RF transitions between high-pin-count, high-speed vertical connectors (HSVCs)—commonly used connectors in computing technology—and microwave circuits with grounded coplanar waveguide (GCPW) terminations operating in the low-GHz frequency range [34]. With proper impedance matching in the UWB frequency range, a handful of HSVCs can terminate 256 densely packed array elements on the Tx array panel, providing the means for large scale, high quality RF interconnects at a much lower cost than coaxial connectors. HSVCs also enable easy modular assembly by inserting the desired RF feed network PCBs into the HSVCs of the antenna panel. The proposed modular design, developed for the UWB frequency range, can be used with various large, printed antenna arrays and microwave circuits in both frequency-sweep and time-domain measurement setups.

Here, we propose and investigate two types of RF feed network PCBs: (i) for simultaneous excitation of all antenna elements (with power-splitting feed network) and (ii) for sequential excitation of individual elements. (with RF-switched feed network). Both are realized on PCB technology. The specific absorption rate (SAR) is investigated through simulations for the case of a compressed breast measurement, for which the Tx array is designed. The results establish the Tx power levels in both illumination scenarios, which ensure compliance with RF safety regulations. Furthermore, the near-field distributions within the tissue are analyzed and compared in various illumination scenarios.

The paper is organized as follows. Section 4.2 describes the design of the Tx antenna array and provides both simulation and measurement results. Section 4.3 focuses on the design, simulation, and testing of the switching feed network, which enables the excitation of individual array elements. Section 4.4 explores near field distributions, the SAR calculations, and the Tx power levels. Finally, Section 4.5 concludes with a summary of the key findings and future research directions.

4.2 Transmitting Antenna Array

4.2.1 Antenna Element Design and Array Configuration

Figure 4-1 illustrates the proposed 16×16 Tx array, comprising shielded slot antenna elements on a multi-layer PCB. It is designed to operate in direct contact with the breast tissue. To realize a reliable RF interconnect between the densely packed Tx array and the vertical RF feed network PCBs, board-to-board HSVCs [35] are integrated into the design. Note that the Tx array panel consists of 5 identical PCB tiles positioned side-by-side with the total number of elements being 18×20, of which only the internal 16×16 elements connect to the RF feed network PCBs. The remaining unconnected antenna elements are along the edges of the Tx array, which is important for uniform performance across the internal 16×16 antenna elements.

Each HSVC features 50 pins spaced 2 mm apart on either side, thus supporting up to 8 elements per side due to the 12 mm center-to-center element spacing. To simplify the design, only one side of the connectors is utilized, allowing

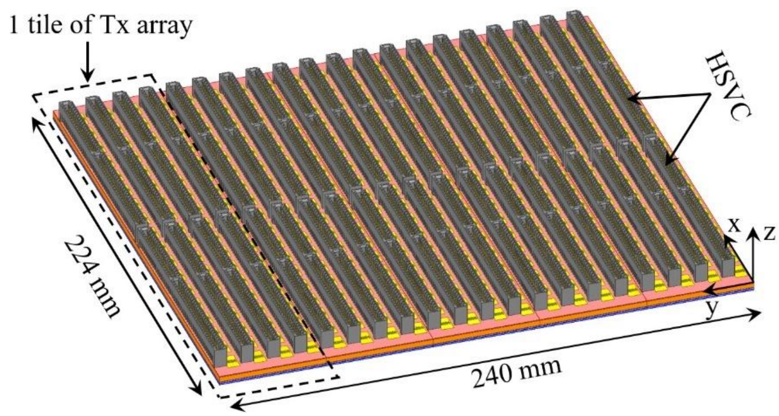

Figure 4-1: Isometric view of the CAD model of the 16×16 UWB Tx array integrated with HSVC. Dimensions in mm.

two edge- to-edge connectors to cover one row of 16 elements. A total of 32 HSVCs and 16 RF feed network PCBs (inserted in the connectors) are used to feed the 16×16 array. Note that all unused connector pins are grounded to avoid ground loops.

The stack-up of the proposed Tx array is shown in Figure 4-2, along with a color-coded table listing the thickness and dielectric properties of each layer. The structure consists of four metallization layers: the connector layer (metal layer 1), the shield layer (metal layer 2), the antenna feed layer (metal layer 3), and the slot layer (metal layer 4), which comes in contact with the breast tissue.

The Tx array design shares some features with the Rx array described in [27], including the inter-element spacing, the feeding forks in metal layer 3, and the slots in metal layer 4. However, it also incorporates substantial modifications in metal layers 1 and 2. These have been completely re-engineered because: (i) they do not contain the footprint of the LNA chips in the Rx array, and (ii) they accommodate the HSVC's footprint and the respective impedance-matched transmission lines and ground slots. An adjustment in the triple-wire vertical

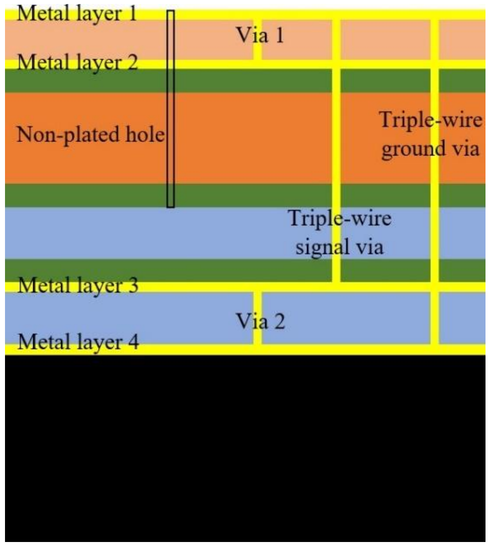

(a)

	Material	Thickness
	Copper	1 oz
	Rogers RO4350B (ε_r 3.5, tanδ 0.0037)	0.254 mm
	Copper	0.5 oz
	RO4460G2 (ε_r 6.15, tanδ 0.004)	0.1 mm
	FR4 (ε_r 4.34, tanδ 0.02)	2.364 mm
	RO4460G2 (ε_r 6.15, tanδ 0.004)	0.1 mm
	Rogers RO3010 (ε_r 10.2, tanδ 0.0022)	0.635 mm
	RO4460G2 (ε_r 6.15, tanδ 0.004)	0.073 mm
	Copper	0.5 oz
	Rogers RO3010 (ε_r 10.2, tanδ 0.0022)	0.635 mm
	Copper	1 oz
	Breast Tissue Phantom Carbon-rubber sheet (ε_r 9.6, tanδ 0.4)	66 mm

(b)

Figure 4-2: (a) A multi-layer PCB stack-up of the proposed Tx array. (b) Color-coded table listing the thickness and material properties of the stack-up.

transition from the antenna to metal layer 1 (where the HSVCs reside) has also been made. Figure 4-3 illustrate the geometry of an antenna element across the four metallic layers. Specifically, Figure 4-3a details the GCPW connecting the HSVC footprint to the antenna input terminals at the triple-wire vertical transition. This transition is a ground-signal-ground interconnect realized with three via-holes. The GCPW signal trace connects to the signal via-hole whereas the ground planes connect to the ground via-holes. The triple-wire transition carries the RF signal from the GCPW on metal layer 1 through an opening in the shield in metal layer 2 (see Figure 4-3b), and into the feeding fork in metal layer 3 (see Figure 4-3c). The shield layer (metal layer 2) ensures unidirectional radiation. Grounding vias (Via1 and Via2) are strategically placed throughout the stack-up to guarantee the grounding of the GCPWs on both the connector and fork layers. Additionally, non-plated holes in the multi-layer structure are used to secure the HSVCs onto the Tx array PCB. Since the antennas are now terminated with the HSVCs, their

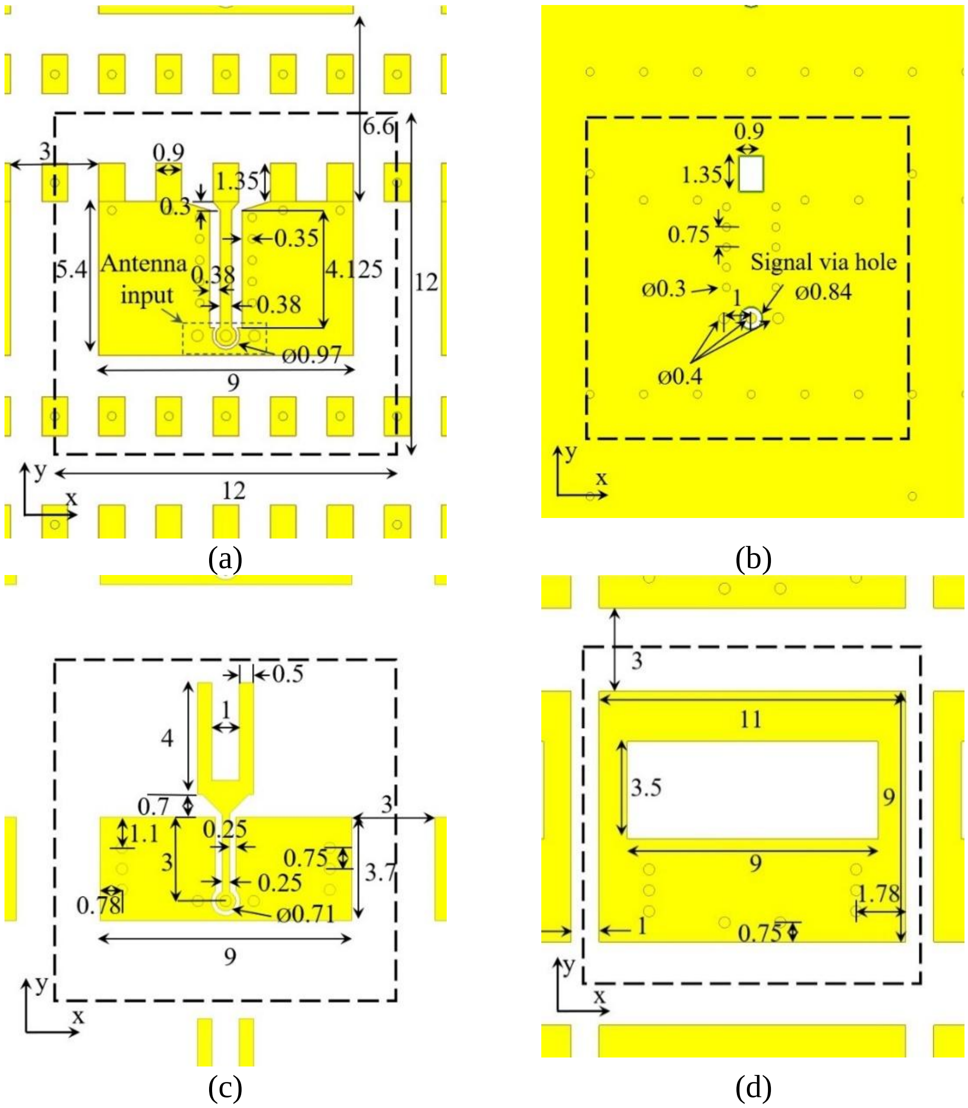

Figure 4-3: Layout and dimensions (in mm) of one element in: (a) connector layer (metal layer 1), (b) shield layer (metal layer 2), (c) feed layer (metal layer 3) and (d) slot layer (metal layer 4). The dash-line shows the area of 12×12 mm^2 occupied by each element.

performance in terms of impedance matching and mutual coupling must be evaluated at this new termination.

4.2.2 Feed-through Network Design

Testing the HSVC-terminated Tx array with a vector network analyzer (VNA) requires an impedance-matched transition from the HSVCs to coaxial connectors. To this end, we have designed feed-through vertical PCBs for insertion

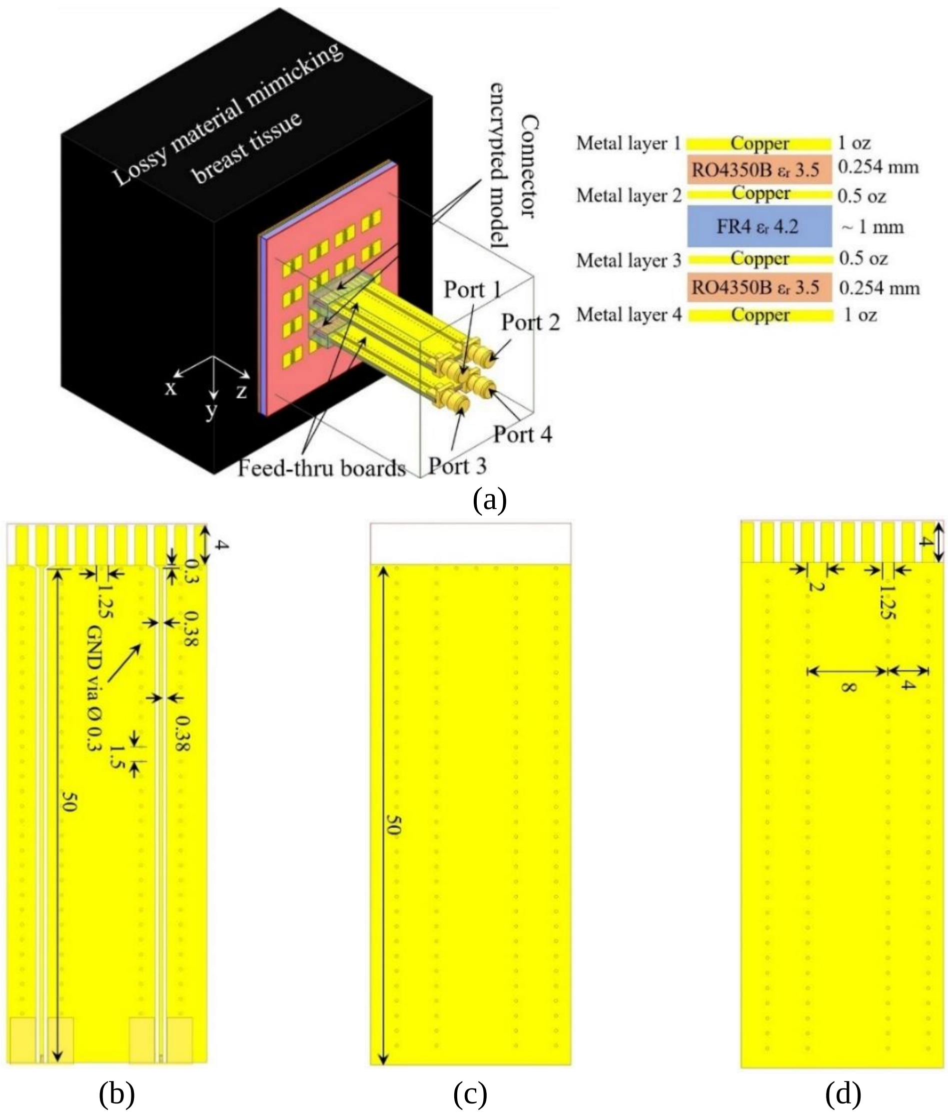

Figure 4-4: (a) Isometric view of the simulated 4×4 Tx array, illustrating the termination with HSVCs, the mated feed-through PCBs, and the corresponding port assignments. The feed-through PCB stack-up is also shown. The box surrounding the feed-through PCBs (in solid black line) and going through the antenna PCB all the way to the tissue medium is used to calculate the near-field directivity of an antenna element. (b) Layout and dimensions (in mm) of the GCPWs on the feed-through PCB. (c) The ground plane in metal layers 2 and 3. (d) The ground plane in metal layer 4.

into the HSVCs. They realize GCPW interconnects, spaced by 12 mm, between edge-mount SMA connectors and the HSVCs, as shown in Figure 4-4a. Figure 4-4a also provides the PCB stack-up. Note that the CAD model includes the encrypted

HSVC model (provided by the manufacturer) as well as the best possible comparison between simulated and measured results.

As previously shown [34], 50-Ω GCPW does not provide an optimal transition to/from the HSVC (originally designed for microstrip lines). GCPW interconnects with a signal trace width of 0.38 mm and a gap width of 0.38 mm are employed here on both the antenna side (metal layer 1, Figure 4-3a) and the feed-through PCBs; see Figure 4-4b. Moreover, the shield layer on the antenna PCB (see Figure 4-3b) must incorporate a rectangular slot beneath the HSVC's pin pad at the signal trace of the GCPW. Similarly, the ground plane of the feed-through PCBs, shown in Figure 4-4c, must be voided beneath the HSVC's pin pads in metal layers 2 and 3. The different width and gap of the GCPW (compared to that used in the Rx array in [27] where the antennas are terminated with SMPS coaxial connectors) necessitates modifications in the placement of the triple-wire vertical transition and its inter-wire spacing (Figure 4-3a) to achieve the best impedance match.

4.2.3 Tx Array Performance Evaluation

To validate the performance of the Tx antenna array terminated with the HSVCs, a 4-port simulation is conducted in HFSS [36], as shown in Figure 4-4a. Since the available HSVC encrypted model includes only 20 pins (10 pins per row), a 4×4 Tx antenna array is simulated. The four central elements are fed from two feed-through PCBs using wave-port excitation at the SMA connectors. The port assignment is shown in Figure 4-4a. The breast tissue is modelled as a 66-mm thick slab with relative permittivity. $\varepsilon_r \approx 9.6 - i3.8$ (averaged over the frequency band from 3 GHz to 8 GHz), mimicking the average permittivity of tissue in the BI-RADS breast-density category B [37]. The analysis provides the antennas'

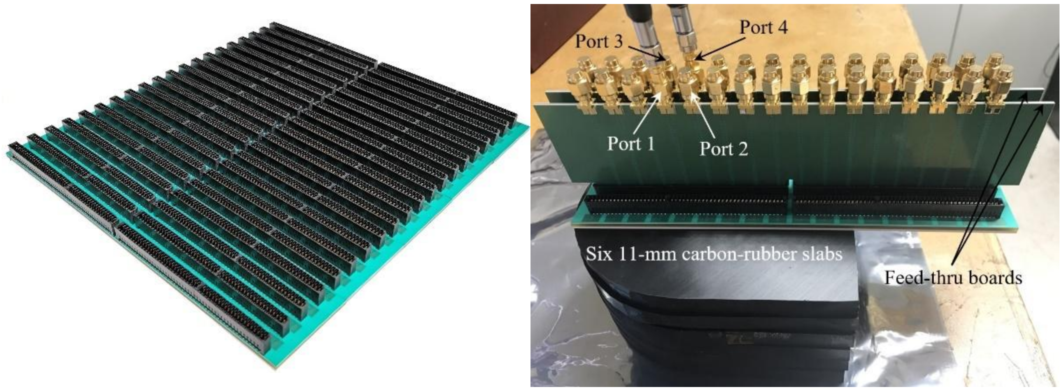

(a) (b)

Figure 4-5: (a) Isometric view of the 16×16 Tx array, constructed from 5 identical PCB tiles. (b) Measurement setup using one antenna tile positioned on top of six custom-made carbon rubber slabs, each 11 mm thick, mimicking breast tissue. Two feed-through PCBs are inserted into two rows of HSVCs feeding 32 elements.

coefficients as well as their mutual coupling, which are compared to the measurements with the fabricated prototype shown in Figure 4-5. Figure 4-5a shows a photo of the 16×16 Tx array panel, assembled from 5 identical PCB tiles, each containing 72 elements. We reiterate that the peripheral elements function as dummy elements. The fabricated feed-through vertical PCBs are shown in Figure 4-5b, where two of them are inserted in the HSVCs on one of the antenna tiles to feed two array rows (2×16 elements). The antenna tile is placed on top of a 66-mm thick stack of 11-mm thick custom-made carbon- rubber slabs with relative permittivity $\varepsilon_r \approx 9.6 - i3.8$, matching the breast tissue permittivity in the simulation. The port assignment in the measurement, shown in Figure 4-5b, matches that in the simulations (see Figure 4-4a). A two-port VNA [38] is used to measure the antenna reflection coefficients and their mutual coupling. All coaxial connectors not connected to the VNA during a measurement are terminated with 50-Ω loads.

The simulated and measured reflection coefficients are plotted in Figure 4-6a versus frequency, indicating a very good impedance match across the frequency range from 3 GHz to 8 GHz. While, on average, the simulations agree with the measurements, there are some significant differences, which we attribute to the fact that the simulation involves a small 4×4 Tx array along with a 20-pin HSCV, whereas the antenna tile in the measurement consists of 4×16 elements and a 50-pin HSVC. Note that the HFSS encrypted HSVC model is available only for the 20-pin version of the connector.

The simulated and measured mutual coupling coefficients are shown in Figure 4-6b. The agreement between simulations and measurements is, on average,

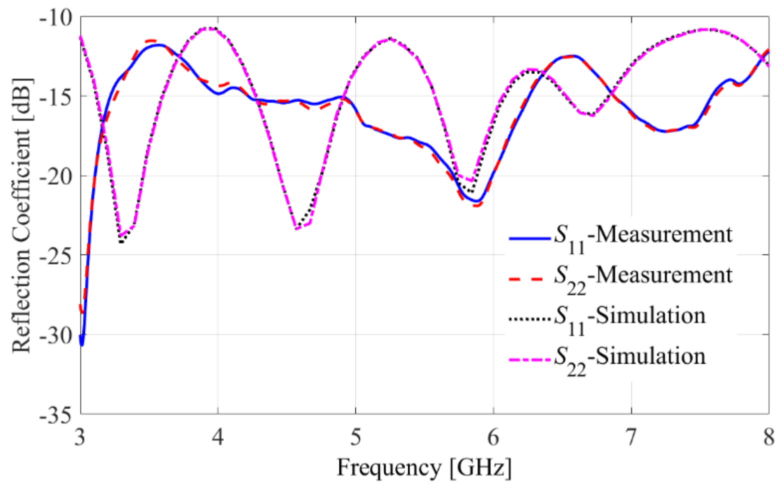

(a)

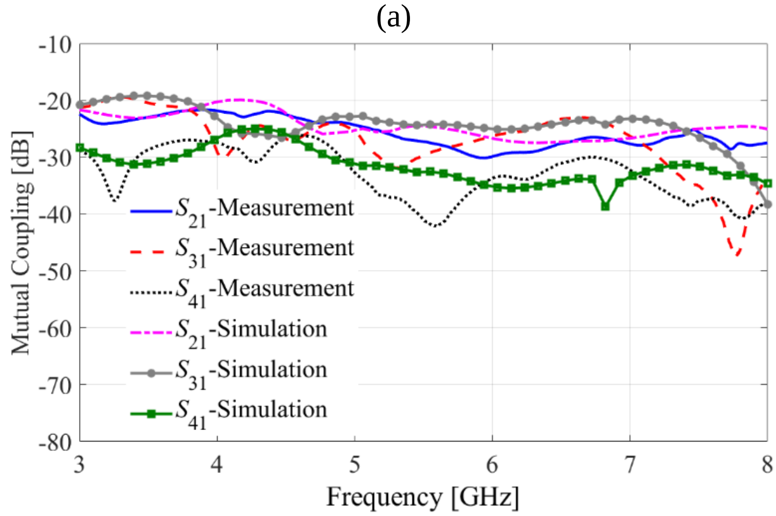

(b)

Figure 4-6: (a) Simulated and measured reflection coefficients. (b) Simulated and measured mutual coupling between the elements indicated in Figure 4-5b.

very good. Also, both sets of curves indicate that the mutual coupling between neighboring antenna elements is at or below −20 dB across the desired frequency range. As expected, the mutual coupling between diagonal elements (S_{41}) is the lowest (below −25 dB).

The near-field directivity and near-field radiation efficiency of an antenna element in the Tx array are evaluated through simulation. The near-field directivity is the ratio of the power coupled into the tissue $P_{\rm rad}^{\rm tsu}$ and the total radiated power in all directions $P_{\rm rad}$ [39]. The power calculations use a rectangular box of size 54 mm × 52 mm × 71 mm, which encloses all 16 antenna elements, as shown in Figure 4-4a. The front face of the box (used to compute $P_{\rm rad}^{\rm tsu}$) overlaps the slot layer at the tissue interface, whereas the back face is at the SMA connectors' edges. Input power of 1 W is injected through one of the SMA connectors. The power radiated through each face is calculated by surface integration of the real part of the normal component of the Poynting vector. The near-field directivity in percentage is plotted

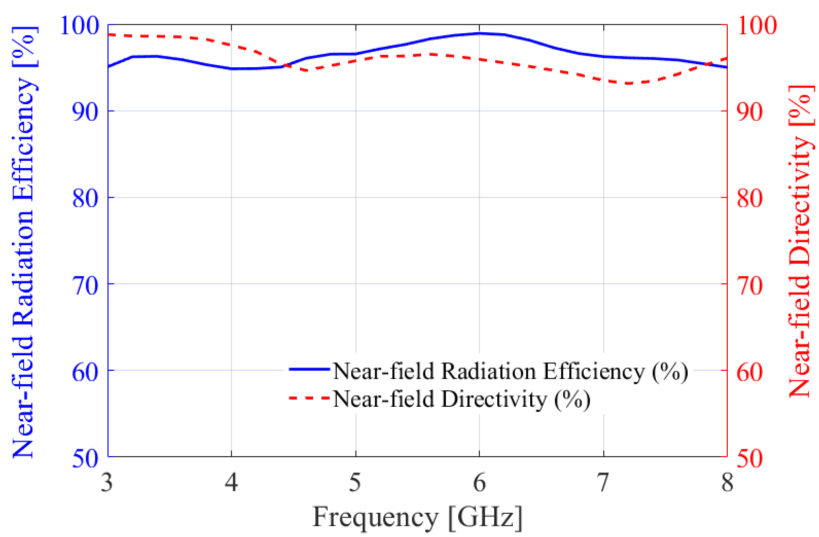

Figure 4-7: Simulated near-field directivity and near-field radiation efficiency of an antenna element in the proposed Tx array.

versus frequency in Figure 4-7. It demonstrates a mean value of 96% across the 3–8 GHz frequency range, confirming that most of the radiated power is directed toward the tissue.

The near-field radiation efficiency is the ratio of total radiated power P_{rad} and the power P_{in} fed to the antenna, i.e., $e_{\mathrm{rad}}^{\mathrm{tsu}} = P_{\mathrm{rad}} / P_{\mathrm{in}}$ [39]. Here, $P_{\mathrm{in}} = 1 - \left(1 - |S_{11}|^2\right) P_{\mathrm{inc}}$ where P_{inc} is the incident power at the antenna terminals and S_{11} is the antenna reflection coefficient. The antenna terminals are at the HSVC input, which requires de-embedding the power loss in the GCPW on the feed-through PCB. To account for this loss, the incident power is adjusted based on the GCPW loss, which is calculated using a transmission line tool for a length of d = 50 mm. For example, at 5.5 GHz, the GCPW introduces a power loss of 0.684 dB, resulting in incident power of $P_{\mathrm{inc}} \approx 0.85$ W. The near-field radiation efficiency, shown in Figure 4-7, is 96% on average across the 3–8 GHz frequency range.

4.3 RF-Switched Feed Network

4.3.1 PCB Design

The use of HSVCs on the Tx array enables a modular assembly, allowing for using various RF feed networks. To implement switched single-element excitation, a 1-to-16 RF-switched feed network is designed in ADS [40], so that one such PCB can control one row of the Tx array. The entire RF-switched feed network consists of 16 PCBs, each terminated with an edge-mount SMA connector, and fed by a 1-to-16 coaxial power divider. The RF-switched feed network PCB uses a four-stage cascaded network of single-pole-double-throw (SPDT) surface-mount switches (see Figure 4-8a). The first stage employs an absorptive switch

[41]. All subsequent stages employ reflective switches [42]. Figure 4-8a also shows the PCB stack-up, where the third and fourth metal layers contain the DC-power and switch-control traces, respectively. All RF interconnects employ identical 50-Ω GCPWs, except for the outputs leading to the HSVCs, where the GCPWs are the same as those in the feed-through PCB design (see Figure 4-4) to ensure the impedance match with the HSVCs. The cascaded design of the RF-switched

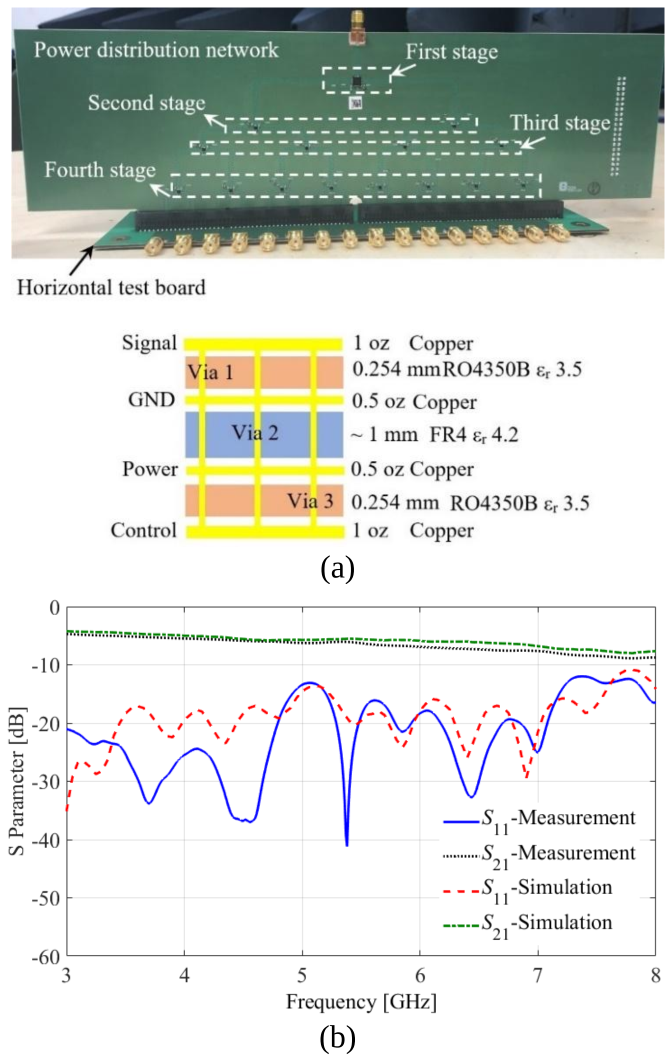

Figure 4-8: The fabricated RF-switched feed network on vertical PCB inserted into two HSVCs mounted on a horizontal test board. The PCB stack-up for the RF-switched feed network is also provided. (b) Simulated and measured *S*-parameters of the fabricated RF-switched feed network PCB when mounted on the horizontal test board. The input is at the SMA connector on the vertical board. The output is at one of the 16 ports on the horizontal board.

network ensures uniform excitation in both magnitude and phase across the array elements. Since this switching scheme excites one antenna at a time, only one RF-switched PCB is activated at a time. All "inactive" PCBs have their first-stage absorptive switch in the OFF state, thus cutting off the RF power to their respective rows of elements. The switches are controlled by a microcontroller board [43] interfaced with a laptop through a USB port. This interface also supplies the DC power to all RF switches and the microcontroller.

4.3.2 Performance Evaluation

A horizontal test board (see Figure 4-8a) is used to validate the performance of the RF-switched feed network PCB, when inserted in the HSVCs. It features 16 20-mm long GCPW interconnects, with the same stack-up and signal trace/gap widths as those of the feed-through network PCBs. The outputs of the horizontal test board are terminated with 16 edge-mount SMA connectors for measurements with the VNA.

The reflection coefficients at the RF-switched feed network input (S_{11}) and the transmission coefficient from this port to one of the 16 outputs of the horizontal test board (S_{21}) are measured while all remaining outputs are terminated with 50-Ω loads. Figure 4-8b presents both the measured and simulated results. In the simulations, the switches are modeled using the S3P files provided by the manufacturers. The measured reflection coefficient (S_{11}) remains below −10 dB across the frequency range and shows good agreement with simulation. The measured transmission coefficient (S_{21}) is also in acceptable agreement with the simulations, with a maximum insertion loss of about 9 dB.

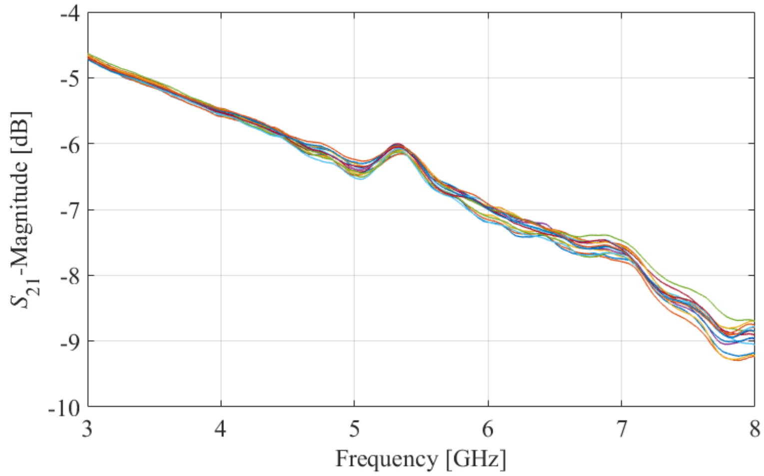

(a)

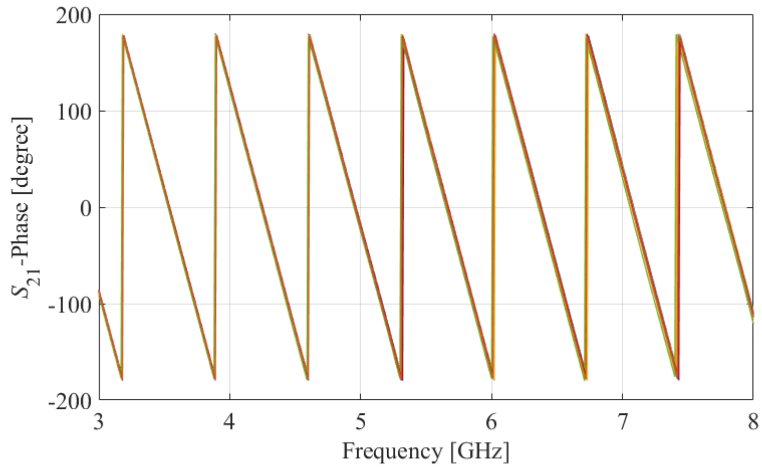

(b)

Figure 4-9: Measured transmission coefficient S_{21} from the input of the RF-switched feed network to the 16 outputs on the horizontal test board: (a) magnitude, (b) phase.

To confirm that the proposed RF-switched feed network has uniform performance across all 16 ports, the S_{21} magnitude and phase at each output are measured as the respective switch is activated. The results, presented in Figure 4-9a and Figure 4-9b, show consistent behavior across all outputs at lower frequencies. As the frequency increases, deviations (especially in the magnitude) become noticeable. The spread in the S_{21} magnitude values reaches about 0.5 dB at 8 GHz.

4.3.3 Tx Array Integration with the RF-switched Feed Network

Once the Tx array is integrated with the RF-switched feed network PCBs, its impedance match at the input of each PCB is again verified. Figure 4-10a shows a measurement setup, where an RF-switched feed network PCB is inserted inside the HSVCs of a Tx array tile to sequentially excite the 16 elements in the respective row of elements. As in a previous measurement, the tile is placed on six custom-made carbon rubber slabs, each 11 mm thick. This ensures the impedance match of the antennas. Port 1 of the VNA is connected to the input of the RF-switched feed network PCB where the reflection coefficient is measured.

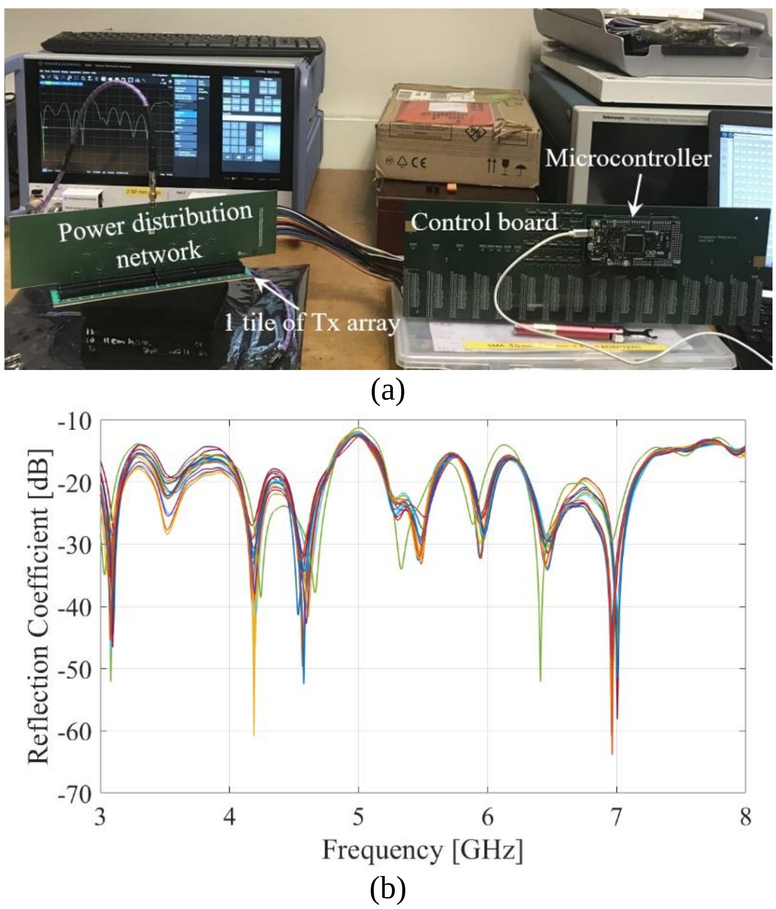

Figure 4-10: (a) Measurement setup for evaluating the reflection coefficient at the input of the RF-switched feed network PCB when inserted into the Tx array tile. The control board is also shown. (b) Measured reflection coefficients as each of the 16 antennas in the row is sequentially activated via RF switching network.

Figure 4-10b shows the results as the 16 antennas in the row are excited one at a time. It is observed that all measured reflection coefficients are below −10 dB. They are also consistent across all 16 antennas in the row.

4.4 Power Levels in Breast Tissue Imaging

4.4.1 Near-field Distribution

The near-zone electric field (*E*-field) distribution inside a homogeneous breast medium is analyzed through simulations at various frequencies from 3 GHz to 8 GHz and for varying depths. Here, the results are presented at the center frequency of 5.5 GHz for both single-element and simultaneous excitation scenarios. The breast medium is again represented as a lossy dielectric with relative permittivity $\varepsilon_r \approx 9.6 - i3.8$. The *E*-field distribution is assessed at depths of 1, 2.5, 5, and 10 mm. The results are shown in Figure 4-11and Figure 4-12 for single-element and simultaneous excitation, respectively. In both cases, each antenna element is excited with 1-W power.

For the single-element excitation, a 4×4 antenna array is analyzed with the *E*-field distribution obtained across the lateral area of the excited antenna element (12×12 mm²); see Figure 4-11. As expected, the pattern becomes smoother and broader with increasing depth. The *E*-field distributions for single-element excitation are generated using both HFSS and FEKO [44], showing a high degree of consistency. Only the FEKO results are shown here for brevity. Simulating the entire 16×16 Tx array is computationally very demanding, exceeding the available RAM and CPU resources. For this reason, an infinite array configuration with periodic boundary conditions is employed. The *E*-field distribution is calculated

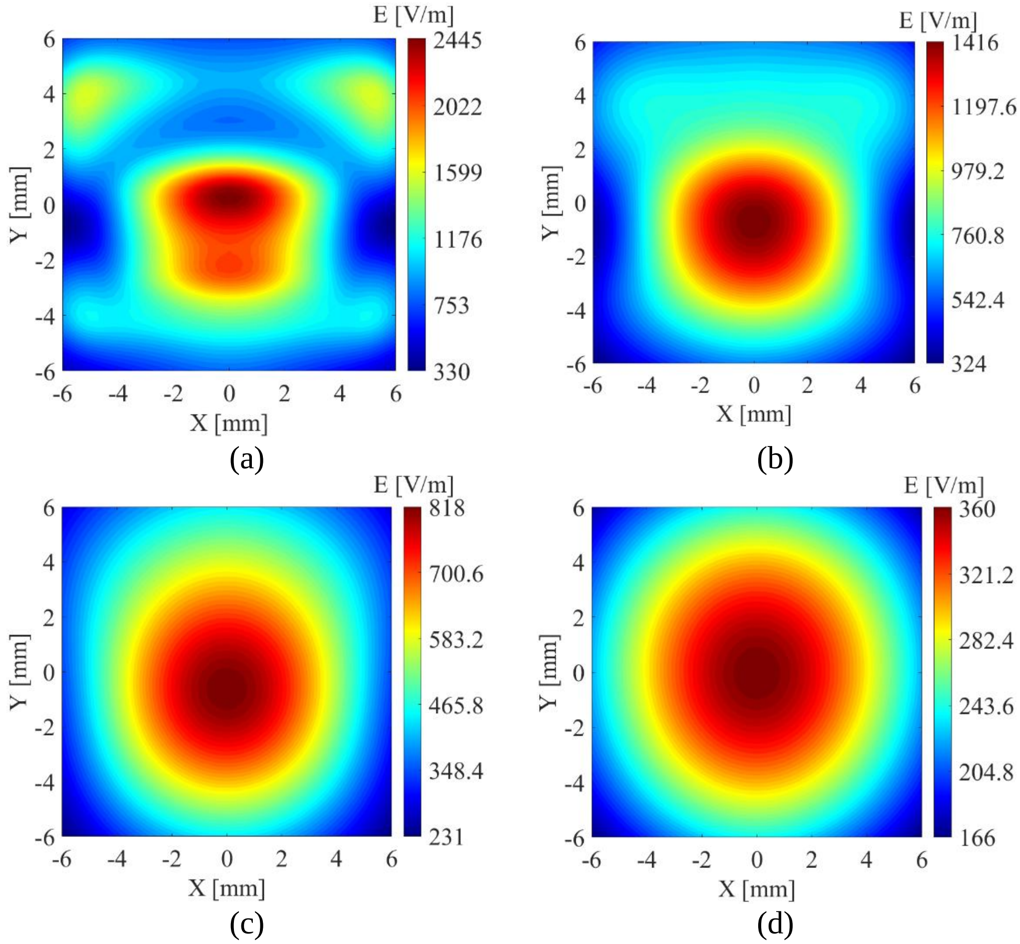

Figure 4-11: *E*-field distributions with single-element excitation at 5.5 GHz within the lateral area of one antenna element (12×12 mm^2) at various depths in the tissue: (a) 1 mm, (b) 2.5 mm, (c) 5 mm and (d) 10 mm.

over a 20×20 cm^2 plane encompassing all 16×16 antenna elements. Similarly to single-element excitation, the *E*-field distribution attains greater uniformity with increasing depth, i.e., the ratio of maximum-to-minimum field intensity decreases; see Figure 4-12.

This study provides important insight for the design of the imaging system. It is desirable to obtain a relatively uniform and symmetric illuminating field distribution within the lateral area of each antenna element (12×12 mm^2). From Figure 4-11 and Figure 4-12, it is apparent that a stand-off distance of about 10 mm between the antennas and the breast tissue would benefit such a distribution. At this

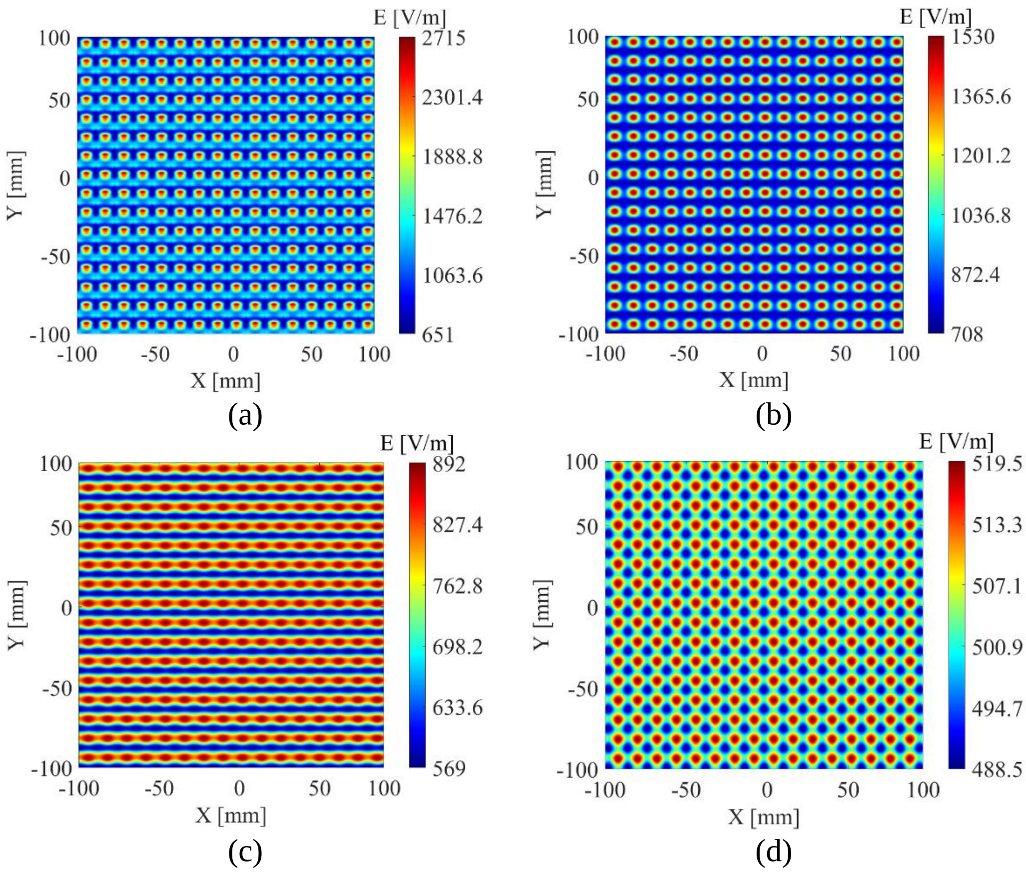

Figure 4-12: *E*-field distributions with simultaneous excitation at 5.5 GHz within the lateral scan area covered by the 16×16 Tx array (20 × 20 cm²) at various depths in the tissue: (a) 1 mm, (b) 2.5 mm, (c) 5 mm, and (d) 10 mm.

distance, the maximum-to-minimum field ratio for single-element excitation is 2.17, whereas for simultaneous excitation, it is 1.06. The stand-off can be realized by placing a 10-mm thick tissue-mimicking carbon-rubber slab (such as those shown in Figure 4-5) between the antennas and the breast tissue.

4.4.2 Specific Absorption Rate Calculation

The study presented here determines the maximum power that can be injected into the Tx array while complying with RF safety standards, e.g., Canada Safety Code 6 [45]. The regulations limit the amount of RF energy coupled into human tissues to prevent health risks associated with excessive heating. This analysis is carried out using simulations in FEKO, where the compressed breast is modeled as a multi-layer structure as shown in Figure 4-13. It consists of 2 mm-thick skin layers at the top and bottom, each with a mass density of 1109 kg/m³ [46]. In-between lies a 52 mm thick breast-tissue layer. It represents a homogenized mixture of fat and fibro-glandular (FG) tissues, which have mass densities of 911 kg/m³ and 1041 kg/m³, respectively [46]. We have investigated the field strength and the specific absorption rate (SAR) in all four categories of the BI-RADS breast-density classification [37]: A (almost entirely fatty, FG < 25%), B (scattered areas of FG density, 25% ≤ FG ≤ 50%), C (heterogeneously dense, 51% ≤ FG ≤ 75%), and D (extremely dense, FG > 75%). The frequency-dependent permittivity and conductivity of the skin, fat, and FG tissues are extracted from [47], [48]. Then, the dielectric properties of the breast-tissue layer are obtained as the volume-weighted average of the fatty and FG tissue properties according to their proportions in the breast-density category. For example, for category D breast tissue, we assume an FG-to-fat volume ratio of 9:1. The worst-case scenario with the highest SAR levels is the category D breast tissue, and only these results are presented below. The Tx array is placed on a 10 mm thick dielectric layer (buffer layer), which provides the

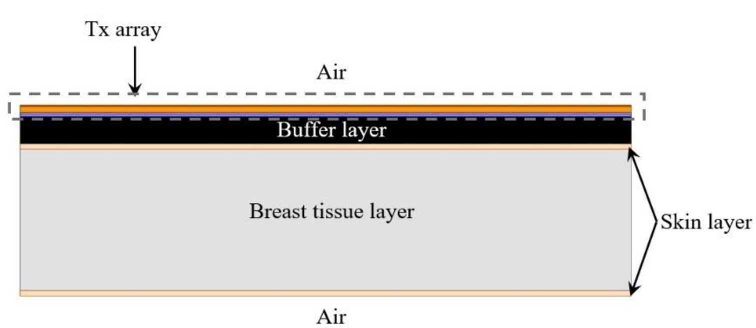

Figure 4-13: Multi-layer model for SAR and maximum *E*-field calculation. The skin layers are 2 mm thick. The compressed breast tissue is represented by a 52 mm thick layer whose permittivity values are extracted as weighted averages based on the tissue composition of the four BI-RADS breast-density classification. A 10 mm buffer layer separates the antennas from the skin.

stand-off between the antennas and the skin (see Figure 4-13). This layer assumes the use of our custom-made carbon-rubber slabs ($\varepsilon_r \approx 9.6 - i3.8$). Increasing its thickness further enhances the field uniformity and area coverage, but at the expense of higher input power.

The maximum *E*-field and SAR are evaluated at various depths within the skin and the breast-tissue layers. The SAR is expressed in terms of the *E*-field strength as $\mathrm{SAR} = \sigma E_{\mathrm{rms}}^2 / \rho$, where σ is conductivity (S/m), ρ is mass density (kg/m^3), and E_{rms} is the root-mean-square (RMS) *E*-field strength (V/m). To avoid field discontinuities, the SAR is computed 1 mm away from media interfaces. Specifically, the SAR in the top skin layer is calculated at 1 mm depth from the buffer–skin interface (11 mm from the antennas). This is where the highest field and SAR values occur due to the antenna proximity and the high skin conductivity. The SAR in the breast-tissue layer is evaluated 1 mm away from the skin–breast-tissue interface (13 mm away from the antennas).

The maximum *E*-field and SAR values are computed for both illumination scenarios—single-element excitation and simultaneous excitation. In both cases, each antenna element is excited with 1-W power at frequencies from 3 GHz to 8 GHz with 1-GHz interval. The 1-W power refers to the actual power delivered to each element after accounting for losses and mismatches introduced by the RF feed network and the HSVCs. The results for the maximum *E*-field and SAR values are summarized in Table 4-1 and Table 4-2 for single-element excitation and simultaneous excitation, respectively. In both cases, the maximum *E*-field and SAR values occur in the skin layer. However, the frequencies at which these maxima peak differ in the two scenarios: 6 GHz for the single-element excitation and 3 GHz for simultaneous excitation.

In regulations, the SAR limit of 1.6 W/kg is defined for the spatially averaged value over 1 g of tissue in a cubic shape and over a 6-minute reference period [45]. For a conservative estimate of the allowed excitation power, we aim to have the peak SAR value not exceeding 1.6 W/kg. Since averaging inherently reduces the SAR value from its peak, our recommended maximum safe power level, denoted as P_{max}, provides a margin of safety beyond what is strictly necessary. Since the tissue medium is linear and the excitation power at each antenna is 1 W in the simulations, P_{max} is calculated using simple power scaling, i.e., $P_{\text{max}} = \text{SAR}_{\text{L}} / \text{SAR}_{\text{max}}$, where SAR_{L} is the limit as per the regulations, and SAR_{max} is the computed peak SAR value among all frequencies in the given excitation scenario. The obtained maximum safe power levels are obtained as 17 mW (12.3 dBm) for single-element excitation and 7 mW (8.45 dBm) for simultaneous excitation.

Table 4-1: Maximum *E*-field and SAR values in the skin and the breast tissue (Category D) with single-element 1-W excitation.

Frequency (GHz)	Skin Layer		Breast-Tissue Layer (Category D)	
	Max E-field (V/m)	Max SAR (W/Kg)	Max E-field (V/m)	Max SAR (W/Kg)
3	188.33	30.46	153.61	19.26
4	210.22	49.81	168.28	31.88
5	221.74	72.24	169.67	41.49
6	227.06	94.54	171.00	51.57
7	184.62	77.32	132.56	37.29
8	160.02	67.89	109.68	29.57

Table 4-2: Maximum *E*-field and SAR values in the skin and the breast tissue (Category D) with simultaneous 1-W excitation of all array elements.

Frequency (GHz)	Skin Layer		Breast-Tissue Layer (Category D)	
	Max E-field (V/m)	Max SAR (W/Kg)	Max E-field (V/m)	Max SAR (W/Kg)
3	509.64	223.10	457.66	170.95
4	354.94	141.98	303.99	104.03
5	355.95	186.17	299.01	128.86
6	304.85	170.41	247.01	107.69
7	255.59	148.20	199.97	84.86
8	221.18	129.70	164.56	66.55

4.5 Conclusion

We have presented a 16×16 UWB Tx planar antenna array comprised of shielded slot-antenna elements operating across the 3-8 GHz frequency range. The array is designed to serve as an illuminating module in an electronically switched microwave imaging system performing measurements on the compressed breast. The array leverages a novel modular architecture, using HSVCs to provide seamless RF transitions between the antenna panel and any desired RF feed network realized on PCBs inserted in the HSVCs. A very good impedance match is demonstrated between the antenna elements and the HSVCs, along with antenna near-field directivity better than 94% across the frequency band, which confirms the ability to efficiently couple power into the tissue. The near-field radiation efficiency of an array element, with its HSVC interconnect included, is better than 90% across the frequency band, indicating low-loss interconnect performance.

Additionally, two RF feed network PCBs are designed, fabricated and demonstrated: one for simultaneous excitation of all elements (with power-splitting feed network) and another for sequential single-element excitation (with RF-switched feed network). In the latter configuration, the array can also serve as an RF-switched receiving array. Both networks show excellent impedance match to the HSVCs and uniform performance across all outputs. The proposed modular design, featuring robust board-to-board microwave signal transfer, is readily applicable to other UWB applications requiring high channel counts on densely packed antenna arrays or electronic components.

Detailed assessment of the array's near-field distribution is carried out, demonstrating smooth *E*-field distribution within the target tissue. It is shown that a stand-off distance of 10 mm or more between the slot elements and the breast tissue is beneficial in achieving uniform field intensity distribution. This stand-off is realized with a tissue-mimicking buffer layer, which ensures the impedance match of the antennas. The SAR of the Tx array is also analyzed through simulations of the compressed breast imaging scenarios, providing the appropriate power levels for the two excitation configurations, which ensure compliance with RF safety standards.

Future work will focus on the integration of the proposed Tx array with the IF-switched Rx array into a complete microwave electronic scanner for compressed-breast imaging. This will enable studies on the benefits of employing various illumination schemes in image reconstruction as well as on the limitations of the imaging modality stemming from the power limitations imposed by the RF safety regulations.

4.6 References

[1] Z. Xinyue, X. Yang, Y. Ding, Y. Wang, J. Zhou, and L. Zhang, "Contactless simultaneous breathing and heart rate detections in physical activity using IR-UWB radars," *Sensors,* vol. 21, no. 16, pp. 5503, Aug. 2021.

[2] C. H. Tseng, T. J. Tseng, and C. Z. Wu, "Cuffless blood pressure measurement using a microwave near-field self-injection-locked wrist pulse sensor," *IEEE Trans. Microw. Theory Techn*., vol. 68, no. 11 pp. 4865-4874, Aug. 2020.

[3] N. K., Nikolova. "Microwave imaging for breast cancer," *IEEE Microw. Mag.*, vol. 12, no. 7, pp.78-94, Dec. 2011.

[4] R. C. Conceição, J. J. Mohr, and M. O'Halloran, "An introduction to microwave imaging for breast cancer detection." *Springer*, 2016. Accessed: Sep. 5, 2024, [Online]. Available: https://link.springer.com/content/pdf/10.1007/978-3-319-278667.pdf

[5] A. Zamani, S. A. Rezaeieh, and A. M. Abbosh, "Lung cancer detection using frequency-domain microwave imaging," *Electron. Lett.*, vol. 51, no. 10, pp. 740-741, May 2015.

[6] M. N. Hamza, S. Koziel, and A. Pietrenko-Dabrowska, "Design and experimental validation of a metamaterial-based sensor for microwave imaging in breast, lung, and brain cancer detection," *Sci. Rep.*, vol. 14, no. 1, pp.16177, Jul. 2024.

[7] S. Bing, C. K. Chawang, and J. C. Chiao, "A tuned microwave resonant sensor for skin cancerous tumor diagnosis," *IEEE J. Electromagn. RF Microw. Med. Biol.*, vol. 7, no. 4, pp. 320-327, Jun. 2023.

[8] K. C. Santos, C. A. Fernandes, and J. R. Costa, "Feasibility of bone fracture detection using microwave imaging," *IEEE Open J. Antennas Propag.*, vol. 3, pp.836-847, Jul. 2022.

[9] D.O. Rodriguez-Duarte, J. A. Tobon Vasquez, R. Scapaticci, G. Turvani, M. Cavagnaro, M. R. Casu, L. Crocco, F. Vipiana, "Experimental validation of a microwave system for brain stroke 3-D imaging," *Diagnostics*, vol. 11, no. 7, pp. 1232, Jul. 2021.

[10] D.O. Rodriguez-Duarte, C. Origlia, J. A. Vasquez, R. Scapaticci, L. Crocco, F. Vipiana, "Experimental assessment of real-time brain stroke monitoring via a microwave imaging scanner," *IEEE Open J. Antennas Propag.*, vol. 3, pp. 824-835, Jul. 2022.

[11] D.O. Rodriguez-Duarte, J. A. T. Vasquez, R. Scapaticci, L. Crocco, and F. Vipiana, "Assessing a microwave imaging system for brain stroke monitoring via high fidelity numerical modelling," *IEEE J. Electromagn. RF Microw. Med. Biol.*, vol. 5, no. 3, pp. 238-245, Jan. 2021.

[12] T. Lauteslager, M. Tømmer, T. S. Lande, and T. G. Constandinou, "Dynamic microwave imaging of the cardiovascular system using ultra-wideband radar-on-chip devices," *IEEE Trans. Biomed. Eng.*, vol. 69, no. 9, pp. 2935-2946, Mar. 2022.

[13] *Breast Cancer*. American Cancer Society. Accessed: Sep. 5, 2024. [Online]. Available: https://www.cancer.org/cancer/types/breast-cancer.html

[14] *Dense Breasts: Answers to Commonly Asked Questions*. National Cancer Institute. Accessed: Sep. 5, 2024. [Online]. Available: https://www.cancer.gov/types/breast/breast-changes/dense-breasts#

[15] M. von Euler-Chelpin, M. Lillholm, I. Vejborg, M. Nielsen M, E. Lynge, "Sensitivity of screening mammography by density and texture: a cohort study from a population-based screening program in Denmark," *Breast Cancer Res.*, vol. 21, p. 111, Oct. 2019.

[16] N.R. Payne, S.E. Hickman, R. Black, A. N. Priest, S. Hudson, F. J. Gilbert, "Breast density effect on the sensitivity of digital screening mammography in a UK cohort," *Eur. Radiol.*, 2024. Accessed: Sep. 5, 2024. [Online]. Available: https://link.springer.com/article/10.1007/s00330-024-10951-w

[17] *Breast Cancer Screening*. American Cancer Society. Accessed: Sep. 10, 2024. [Online]. Available: https://www.cancer.org/cancer/types/breast-cancer/screening-tests-and-early-detection/american-cancer-society-recommendations-for-the-early-detection-of-breast-cancer.html

[18] *Breast Cancer Screening*. Ontario Breast Screening Program (OBSP). Accessed: Sep. 10, 2024. [Online]: Available: https://www.cancercareontario.ca/en/cancer-care-ontario/programs/screening-programs/ontario-breast-obsp

[19] M. Adachi, T. Nakagawa, T. Fujioka, M. Mori, K. Kubota, G. Oda and T. Kikkawa, "Feasibility of portable microwave imaging device for breast cancer detection," *Diagnostics*, vol. 12, no. 1, pp. 27, Dec. 2021.

[20] T. M. Grzegorczyk, P. M. Meaney, P. A. Kaufman, and K. D. Paulsen, "Fast 3-D tomographic microwave imaging for breast cancer detection," *IEEE Trans. Med. Imaging*, vol. 31, no. 8, pp. 1584-1592, May 2013.

[21] B. M. Moloney, P.F. McAnena, S.M. Abd Elwahab, A. Fasoula, L. Duchesne, J.D.G. Cano, C. Glynn, A. O'Connell, R. Ennis, A.J. Lowery, and

M.J. Kerin, “Microwave imaging in breast cancer–results from the first-in-human clinical investigation of the wavelia system,” *Acad. Radiol.*, vol. 29, pp. S211-S222, Jan. 2022.

[22] R. Sidebottom, D. Webb, B. Bishop, M. Kabir, S. Allen, “Results for the London investigation into dielectric scanning of lesions study of the MARIA M6 breast imaging system,” *Br. J. Radiol.*, vol. 97, pp. 549–552, Mar. 2024.

[23] D.A. Sánchez-Bayuela, N. Ghavami, C.R. Castellano, A. Bigotti, M. Badia, L. Papini, G. Raspa, G. Palomba, M. Ghavami, R. Loretoni, and M. Calabrese, “A multicentric, single-arm, prospective, stratified clinical investigation to evaluate MammoWave’s ability in breast lesions detection,” *PLoS One*, vol. 18, no. 7, pp. e0288312, Jul. 2023.

[24] A. Janjic, M. Cayoren, I. Akduman, T. Yilma, E. Onemli, O. Bugdayc, M.E. Aribal, “SAFE: A novel microwave imaging system design for breast cancer screening and early detection—Clinical evaluation,” *Diagnostics*, vol. 1, no. 3, pp. 533, Mar. 2021.

[25] E. C. Fear, J. Bourqui, C. Curtis, D. Mew, B. Docktor, C. Romano, “Microwave Breast Imaging with a Monostatic Radar-Based System: A Study of Application to Patients,” *IEEE Trans. Microw. Theory Tech.* 2013, vol. 61, pp. 2119–2128, Apr. 2013.

[26] S. Katrin, B. Jeremie, W. Zefang, B. Brendon, L.E.A. Mark, “Microwave imaging for monitoring breast cancer treatment: A pilot study,” *Med. Phys.* Vol. 50, pp. 7118–7129, Nov. 2023.

[27] N. V. Shahmirzadi, V. Tyagi, J. Nguyen, R. Kazemivala, N. K. Nikolova, and C.H. Chen, “Planar array of UWB active slot antennas for microwave

imaging of the breast," *IEEE Trans. Antennas Propag*., vol. 71, no. 4, pp. 2946-2957, Jan. 2023.

[28] A. W. Preece, I. Craddock, M. Shere, L. Jones, and H. L. Winton, "MARIA M4: clinical evaluation of a prototype ultrawideband radar scanner for breast cancer detection," *J. Med. Imaging*, vol. 3, no. 3, pp. 033502-033502, Jul. 2016.

[29] H. Song, S. Sasada, T. Kadoya, M. Okada, K. Arihiro, X. Xiao, and T. Kikkawa, "Detectability of breast tumor by a hand-held impulse-radar detector: performance evaluation and pilot clinical study," *Sci. Rep.*, vol. 7, p. 16353, Nov. 2017.

[30] E. Porter, H. Bahrami, A. Santorelli, B. Gosselin, L.A. Rusch, and M. Popović, "A wearable microwave antenna array for time-domain breast tumor screening," *IEEE Trans. Med. Imaging*, vol. 35, no. 6, pp. 1501-1509, Jan. 2016.

[31] M. Ghamati, M. Taherzadeh, F. Nabki, and M. Popović, "Integrated fast UWB time-domain microwave breast screening," *IEEE Trans. Instrum. Meas.*, vol. 72, pp. 1-12, Oct. 2023

[32] M. H. El Misilmani, T. Naous, S. K. Al Khatib, and K.Y. Kabalan, "A survey on antenna designs for breast cancer detection using microwave imaging," *IEEE Access*, vol. 8, pp. 102570-102594, June 2020.

[33] B. Borja, J. A. Tirado-Mendez, and H. Jardon-Aguilar, "An overview of UWB antennas for microwave imaging systems for cancer detection purposes," *Prog. Electromagn. Res. B*, vol. 80, pp. 173-198, May 2018.

[34] N. V. Shahmirzadi, N. K. Nikolova, and C. H. Chen, “Interconnect for dense electronically scanned antenna array using high-speed vertical connector,” *Sensors*, vol. 23, no. 20, article 8596, Oct. 2023.

[35] Samtec. *MEC2-50-01-L-DV*. Accessed: Sep. 20, 2024. [Online]. Available: https://www.samtec.com/products/mec2-50-01-l-dv.

[36] Ansys Corporation. *HFSS 2022 R1*. Accessed: Sep. 20, 2024. [Online]. Available: https://www.ansys.com/

[37] *ACR BI-RADS ATLAS-MAMMOGRAPHY*. Accessed: Sep. 20, 2024. [Online]. Available: https://www.acr.org/-/media/ACR/Files/RADS/BI-RADS/Mammography-Reporting.pdf

[38] R&S® *ZNA43 Vector Network Analyzer 2 Ports*. Accessed: Sep. 25, 2024. [Online]. Available: https://www.rohde-schwarz.com/ca/products/test-and-measurement/network-analyzers/rs-zna-vector-network-analyzers_63493-551810.html.

[39] R. K. Amineh, A. Trehan, and N. K. Nikolova, “TEM horn antenna for ultra-wide band microwave breast imaging,” *PIER B*, vol. 13, pp: 59-74, 2009.

[40] Keysight-Technologies. *Pathwave Advanced Design System (ADS)*. Accessed: Sep. 20, 2024. [Online]. Available: https://www.keysight.com/ca/en/products/software/pathwavedesignsoftware/pathwave-advanced-design-system.html

[41] Renesas, *F2923*. Accessed: Oct. 10, 2024. [Online]. Available: https://www.renesas.com/en/products/rf-products/rf-switches/f2923-constant-impedance-kz-sp2t-rf-switch.

[42] Psemi, *PE42424*. Accessed: Oct. 10, 2024. [Online]. Available: https://www.psemi.com/products/rf-switches/high-isolation-rf-switches/pe42424.

[43] *Arduino Due*. Arduino, Torino, Italy. Accessed: Oct. 10, 2024. [Online]. Available: https://www.arduino.cc/en/Guide/ArduinoDue.

[44] Altair Engineering. *FEKO: Electromagnetic Simulation Software 2022. 3*, Altair, Troy, MI, USA. Accessed: Oct. 17, 2024. [Online]. Available: https://www.altair.com/feko.

[45] *Limits of human exposure to radiofrequency electromagnetic fields in the frequency range from 3 kHz to 300 GHz, Safety Code 6*. Health Canada, Ottawa, ON, Canada, 2015. Accessed: Oct. 17, 2024. [Online]. Available: https://www.canada.ca/en/health canada/services/publications/health-risks-safety/limits-human-exposure-radiofrequency-electromagnetic-energy-range-3-300.html

[46] *Tissue properties database: Density*. IT'IS Foundation. Accessed: Oct. 17, 2024. [Online]. Available: https://itis.swiss/virtual-population/tissue-properties/database/density/

[47] T. Sugitani, S.I. Kubota, S.I. Kuroki, K. Sogo, K. Arihiro, M. Okada, T. Kadoya, M. Hide, M. Oda, and T. Kikkawa, "Complex permittivities of breast tumor tissues obtained from cancer surgeries," *Appl. Phys. Lett.*, vol.104, no. 25, Jun. 2014.

[48] X. Xiao, and T. Kikkawa, "Study on the breast cancer detection by UWB microwave imaging," *IEEE Int. Conf. Microwave and Millimeter Wave Technology*, vol. 4, pp. 1707-1710, Apr. 2008.

Chapter 5

5. Conclusions

5.1 Summary

In this work, significant advancements are made in the development of a novel electronically scanned compressed breast imager through: i) the design, fabrication and evaluation of a planar Rx array of shielded UWB slot antennas where each antenna element is integrated with its own RF front-end, ii) the development and evaluation of a robust RF interconnects for reliable board-to board transitions between the Rx array and its corresponding RF-front end circuitry using HSVCs, enhancing signal integrity and mechanical robustness, and iii) the design, fabrication and evaluation of a modular UWB Tx array, facilitating adaptable illumination configurations for breast microwave imaging. The subsequent discussion outlines the ongoing efforts toward realizing the first prototype of this electronically scanned system and identifies future directions for enhancing its performance and capabilities.

5.2 Ongoing Tasks

Here, ongoing design tasks are briefly described. These tasks aim at completing the Rx module of the breast microwave imager. As detailed in Chapter 3, two edge-to-edge HSVCs support two rows of 16 elements on the active Rx array

PCB, accommodating a total of 32 array elements. A total of 16 HSVCs are required to assemble the entire Rx array. These connectors establish the interface between the active Rx array PCB and eight identical double-sided vertical PCBs, each hosting 32 mixer chips, along with the LO power distribution network and the IF switching network. Thus, this vertical PCBs accommodate the majority of the RF front-end components for the Rx antenna array.

The design of the Rx front-end PCBs poses significant challenges, as it requires the integration of 32 identical RF front-end circuits on a double-sided PCB, 16 per side. The LO power distribution network employed on these vertical PCBs is based on an architecture similar to the RF-switched feed network developed for the Tx array (not shown here for brevity), ensuring near-uniform magnitude and phase across all mixers' LO inputs (see Figure 4-8). The block diagram of the designed IF switching network is depicted in Figure 5-1. Each vertical PCB multiplexes 32 IF signals, 16 channels per side. These 16 IF outputs of the respective mixers are routed to four SP4T IF switches. These switches have a typical insertion loss of 0.8 dB and provide an isolation of over 60 dB at the IF (30 MHz). The outputs of the SP4T switches are directed to a single SP4T switch, resulting in two outputs per double-sided mixer board. With eight vertical PCBs in total, this configuration generates 16 IF outputs, which are subsequently fed into an SP16T coaxial switch. This final stage provides a single IF output to the VNA.

While the design process has been successfully completed, the evaluation, fabrication, and integration of these vertical PCBs into the full compressed breast imager system are still in progress. This work will be published in an additional journal paper.

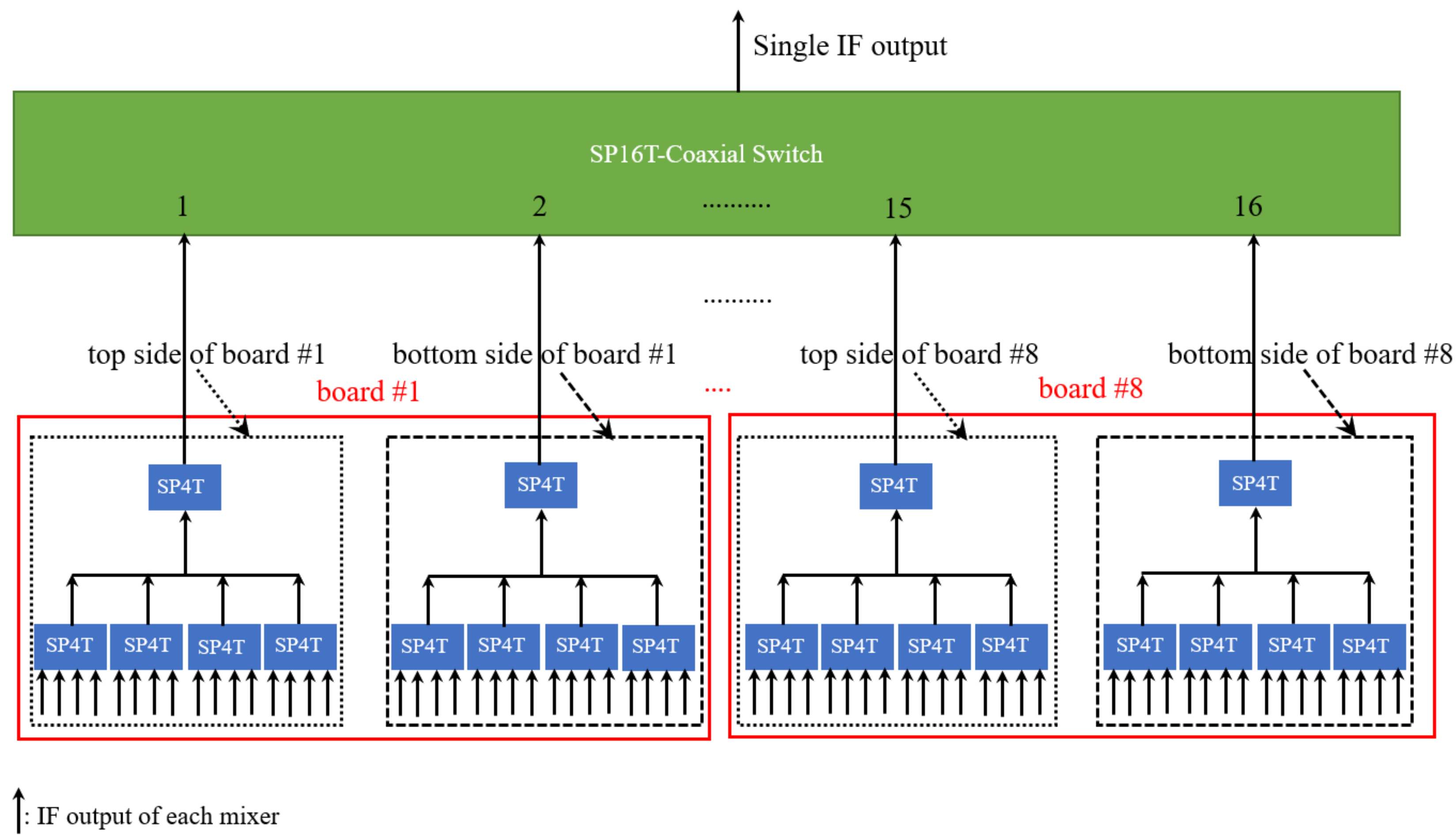

Figure 5-1: The block diagram of the IF switch network realized on the vertical PCBs.

5.3 Future Work

1. *Assembly and Evaluation of an Initial Imaging Prototypes for Phantom-based Measurements*

   This research should primarily focus on the hardware development and the performance evaluation of the individual modules of the electronically scanned compressed breast imager. The individual modules—the Tx and Rx arrays and their associated circuitry—must be integrated into an initial imaging prototype for phantom-based experimental validation (see Figure 5-2). With the active Rx array terminated with HSVCs, multiplexing can be performed either at the RF UWB band (3 GHz to 8 GHz) using a set of eight double-sided RF-switched feed network PCBs (same as those designed for the Tx array), or at the single-tone IF (30 MHz) using eight double-sided vertical PCBs housing the mixers, the LO power distribution network, and the IF-switched network. To perform multiplexing at IF (30 MHz) as shown in Figure 5-2, port 1 of the VNA is connected to the Tx array's RF-switched feed network via a 1-to-16 coaxial power divider, while its port 2 is connected to the IF output of the SP16T coaxial switch (see Figure 5-1). The VNA must be configured to operate in a frequency-conversion (also known as mixer) measurement mode [1]. VNAs operating in this mode are equipped with an auxiliary RF generator, which is synchronized with the main-port RF generator to provide precise user-defined (here 30 MHz) frequency offset. The synchronized LO output of the VNA (see output "LO" from the VNA in Figure 5-2a) is connected to another 1-to-16 coaxial power

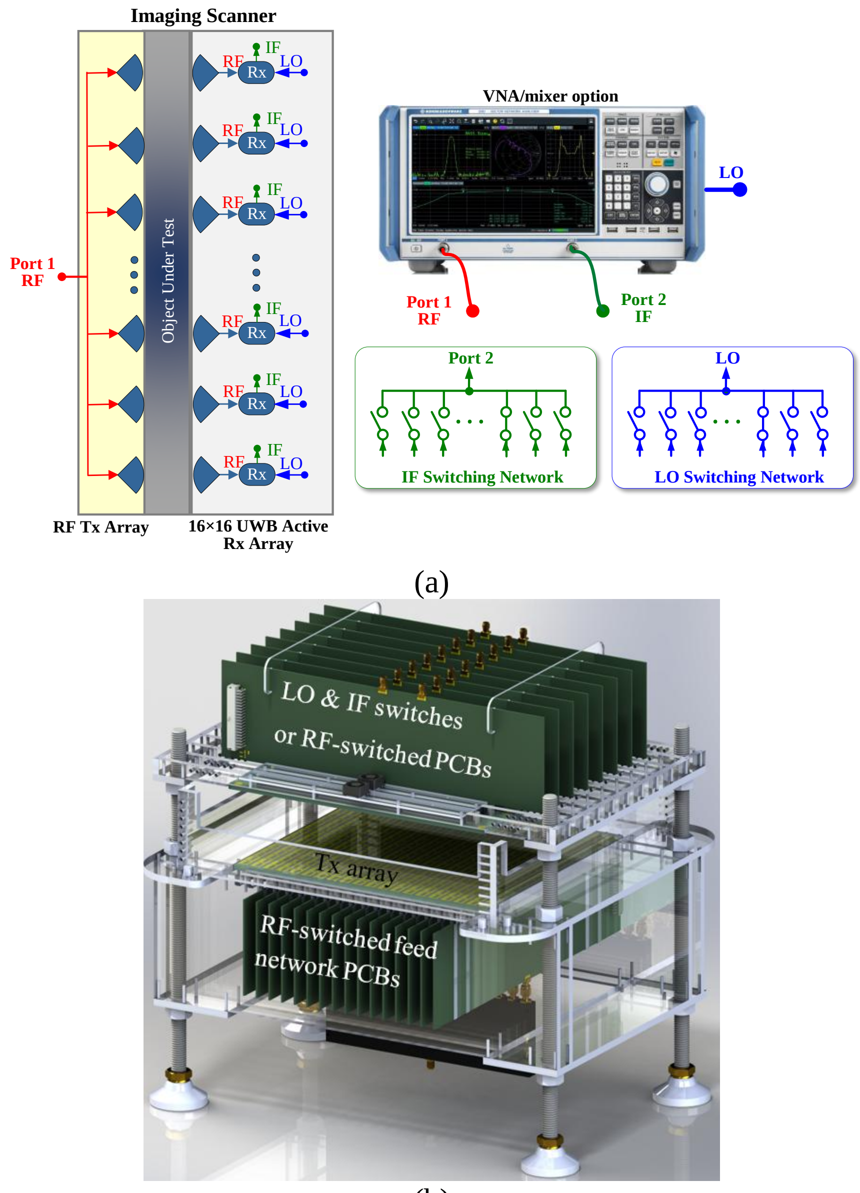

Figure 5-2: (a) System architecture of the electronically scanned compressed breast imager, and (b) CAD model of the initial module for an electronically scanned compressed breast imager (photo credit: Tyler Ackland).

divider followed by the complementary vertical PCBs of the Rx array. Experiments conducted with this initial prototype will not only validate the functionality of the proposed imaging system but will also provide a quantitative comparison of the imaging performance between the IF-switched and the RF-switched multiplexing schemes on the Rx side, establishing a foundation for further optimization and benchmarking.

2. *Evaluation of Different Illumination Scenarios in Imaging Experiments*

   The current Tx array supports two primary excitation schemes: single-element activation via an RF-switched feed network and simultaneous activation using a power-splitting feed network. The RF-switched feed network enables sequential activation of individual elements. Leveraging the modular design of the Tx array, enabled by the HSVCs, these RF-switched networks on the Tx side can be further reconfigured to implement various illumination scenarios (e.g. 5-element excitation or 9-element excitation). Evaluating these different excitation patterns in imaging experiments provides insights into their impact on the image quality, resolution, and artifact suppression, contributing to the optimization of the imaging performance.

3. *Unified Microcontroller System for Enhanced Control*

   Integrating the Rx and Tx array control systems into a unified microcontroller platform will further enhance the system design. This consolidation will ensure precise synchronization between the Tx array and Rx array operations, will minimize inter-board communication delays, and will reduce the overall system size.

4. *Biasing and Thermal Management of LNAs in the Rx Array*

   In the current design, the 16×16 active Rx array is realized by five identical tiles, each containing 4×18 elements. On each tile, 64 antenna elements are equipped with their own LNAs. Due to space constraints (12×12 mm^2 per element), the DC bias for the 32 elements on each tile is supplied by a DC trace network on the left side of the board, while the remaining 32 elements are powered by a DC trace network on the right side (see Figure 5-3). Therefore, all 32 elements are powered simultaneously, even though only one element's output is typically recorded by the VNA at any given time. This simultaneous powering results in substantial DC power consumption, leading to a temperature rise up to 68°C on the electronic layer (metal layer 1, as shown in Figure 2-1a) in the presence of heat sinks. The DC power consumption is typically 60 mA per LNA at a +5V DC supply, while the

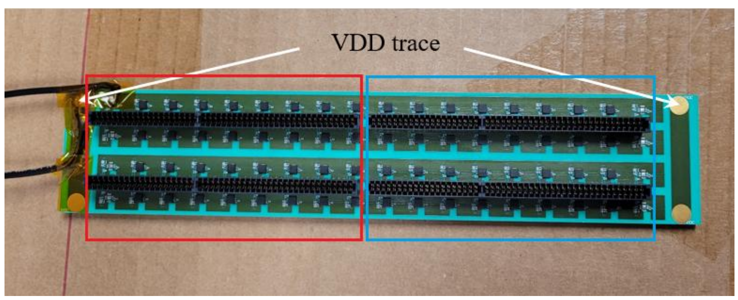

Figure 5-3: DC bias supply configuration for one tile of the Rx array. The red box indicates the 32 elements powered by the left VDD trace, while the blue box indicates the 32 elements powered by the right VDD trace.

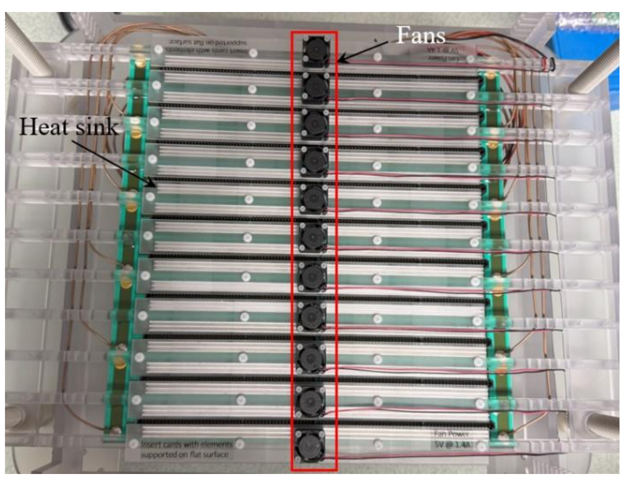

Figure 5-4: The16×16 Rx array realized by 5 identical tiles equipped with fans and heat sinks.

thermal resistance of the junction-to-ground lead is 47°C/W [1]. To further mitigate this temperature rise, fans have been also employed on the Rx array (see Figure 5-4), which are sufficient for phantom-based experiments. However, a temperature evaluation (thermal analysis) is essential at the slot layer (metal layer 4 in Figure 2-1a), where the Rx array will directly contact the breast tissue in clinical trials. These evaluations should be conducted with and without the tissue phantom, as the phantom provides different heat dissipation properties compared to air. If the temperature of the slot side of the Rx array panel exceeds 40°C, this will cause patient discomfort. If this problem occurs, the DC power supply network should be redesigned for better thermal management. Another solution is to move the LNAs from the Rx array PCB to the complementary vertical PCBs. As described in Chapter 3, these vertical boards are inserted in the HSVCs on the Rx array PCB. However, such relocation requires careful investigation, as the primary advantage of placing LNAs directly at the antenna terminals is to amplify the received signal before it encounters attenuation and distortion due to the interconnects. Relocating the LNAs would eliminate any heat concerns within the Rx array.

5. *Design of an RF-front End Chip*

As discussed earlier, the current IF-switched Rx array houses the mixers, the LO power distribution network, and the IF switch network on complementary vertical PCBs. The mixers on these boards are passive elements that only require sufficient LO power for down conversion. However, they introduce conversion loss. Active mixers mitigate the conversion loss (in fact, they provide conversion gain), but they would complicate the design, as they require bias tees and DC bias supply. Moreover, no commercially available active mixers can operate across the 3 GHz to 8 GHz frequency range. Therefor, a promising future direction is the development of a single integrated UWB chip that combines the LNA and mixer functionalities. This integration would significantly streamline the system, enhance signal integrity, reduce interconnect complexity, optimize space usage, and improve the compactness and performance of the Rx array.

6. *Optimization of Passive Antenna Elements for Improved Performance and Cost Efficiency*

   Current antenna elements in both the Rx and Tx arrays feature a complex stack-up structure, composed of multiple substrate laminates with blind vias. This design requires high-precision manufacturing technologies, which are not widely available among PCB manufacturers, and it contributes to high fabrication costs. A potential improvement would involve redesigning the antenna structure to achieve a more cost-effective solution (e.g. by eliminating all blind via-holes) without compromising performance. It is also beneficial to validate the performance of the antenna in the presence of a superstrate to avoid direct contact between the slot antennas and breast tissue in clinical applications. Using regular cleaning agents can damage the slot layer, affecting its performance over time. By employing a superstrate, the cleaning process becomes more efficient, as the superstrate can be cleaned independently without affecting the delicate antenna elements. Furthermore, the current antenna element size is 12×12 mm², which results in a spatial sampling step of 12 mm (without performing mechanical scanning). For optimal image reconstruction in breast microwave imaging, the spatial sampling step should be equal to or smaller than one-half of the wavelength at center frequency of operation in the breast tissue. Reducing the antenna element size to below 10 mm could enhance spatial sampling, providing more detailed imaging. However, this reduction could introduce challenges such as increased mutual coupling and degraded impedance match over the 3 GHz to 8 GHz frequency range, which would need to be carefully addressed in the design modifications.

7. *Clinical Deployment of the proposed electronically scanned compressed breast imager*

   The envisioned clinical deployment is shown in Figure 5-5. Except for the VNA, the electronics is to be mounted on a mechanical frame with a compression paddle for a compressed breast examination. The prototype also features a mechanism for rotating the plane of compression. The envisioned mechanical frame is analogous to those in X-ray mammography, providing planar images of the compressed breast in the transverse and sagittal planes, as well as angles in-between. The VNA, the host computer, and a display will be placed on a table nearby. Ports 1 and 2 of the VNA along with the synchronized LO generator are connected to the Tx and Rx arrays through RF cables. The VNA is connected to the computer through an Ethernet cable for data offload. 256 spatial samples in the lateral (compression) plane with 100 frequency points at each spatial sample can

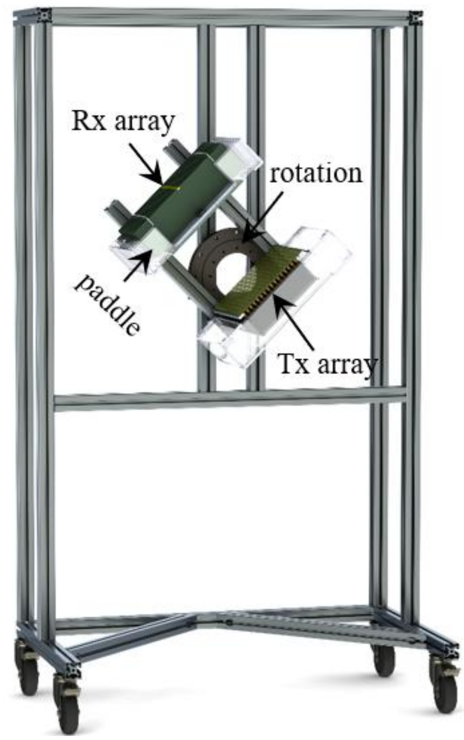

Figure 5-5: Mechanical frame featuring a compression paddle, rotation mechanism, and integrated Tx and Rx arrays for the clinical deployment of the electronically scanned compressed breast imager (photo credit: Tyler Ackland).

be provided, where the estimated time for a breast scan is less than 2 min. The resulting image will be displayed within 30 s of completing the measurement. This clinical deployment will establish a robust and standardized platform for quantitative benchmarking, enabling direct performance comparisons (scan time, dynamic range, sensitivity, etc.) with other imaging prototypes. It is expected that the proposed measurement system will not only provide superior speed compared to prototypes reported in the literature, but it will also feature superior dynamic range (> 120 dB) due to the novel IF-switching architecture. Importantly, this prototype will enable future trials with patients.

8. *Toward low-cost Breast Microwave Imager*

The current research prototype for breast microwave imaging relies on stepped-frequency continuous wave (SFCW) measurements using a VNA with frequency-conversion (mixer) measurement capability. While these VNAs are very accurate and easy to set up, their cost is high. However, the proposed system architecture can be achieved without the use of a VNA. Instead, two off-the-shelf synchronized RF generators (one for the Tx array and one for the LO power distribution network), capable of sweeping the frequency range from 3 GHz to 8 GHz with a 30 MHz frequency offset, can be utilized [3] as shown in Figure 5-6. On the receiver side, an off-the-shelf 30 MHz radio receiver—widely available and affordable—can be employed [4]. This would result in a cost-effective design, potentially making the breast microwave imager much more affordable for broader clinical and research applications.

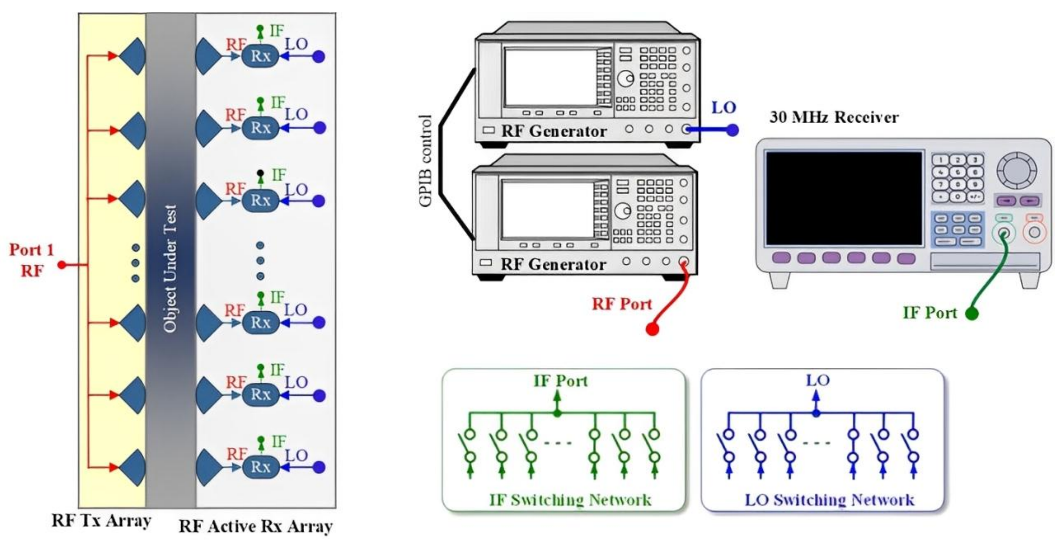

Figure 5-6: Microwave imaging system architecture where the VNA is replaced by alternative low-cost equipment.

5.4 References

[1] Mini-Circuits. *Low Noise Amplifier PMA3-83LN+*. Accessed: Dec. 16, 2024. [Online]. Available: https://www.minicircuits.com/WebStore/dashboard.html?model=PMA3-83LN%2B

[2] R&S® *ZNA43 Vector Network Analyzer 2 Ports*. Accessed: Sep. 25, 2024. [Online]. Available: https://www.rohde-schwarz.com/ca/products/test-and-measurement/network-analyzers/rs-zna-vector-network-analyzers_63493-551810.html

[3] Berkeley Nucleonics Corp, *Multi-Channel RF / Microwave Signal Generator-Model 855B*. Accessed: Dec. 16, 2024. [Online]. Available: https://www.berkeleynucleonics.com/multi-output-rf-microwave-signal-generator

[4] Acquitek, *Wideband HF receiver 30MHz-Model CA7801*. Accessed: Dec. 16, 2024. [Online]. Available: https://www.acquitek.com/product/ca7801-2/